# Current-induced torques in ferromagnets at room temperature

**Zhou Fang**

Department of Physics

University of Cambridge

This dissertation is submitted for the degree of

*Doctor of Philosophy*

Jesus College 2017

# Current-induced torques in ferromagnets at room temperature

**Zhou Fang**

## Abstract

This thesis uses ferromagnetic resonance to explore the current-induced torques (CITs) in two different systems, namely YIG/heavy metal bilayers and bulk NiMnSb, at room temperature. We apply a microwave current to the sample while sweeping the external magnetic field, and measure the longitudinal DC voltage. From a symmetry analysis of the ferromagnetic resonance lineshape, the amplitudes and directions of the CITs parameterised by an effective magnetic field are accurately estimated.

In Chapter 4, YIG samples of different thickness, capped by either Pt or Ta, are studied. The resonance is driven by both spin-transfer torque and Oersted field, and the DC voltage is attributed to both spin rectification and spin pumping. The CITs can be well analysed from the lineshape of the voltage and its dependence on YIG thickness, from which we deduce that the Oersted field dominates over the spin-transfer torque in driving magnetization dynamics.

In Chapter 5, we characterise the CITs in bulk NiMnSb induced by the relativistic spin-orbit coupling effect. Both field-like and antidamping-like spin-orbit torques are observed and analysed in detail. At the end of this chapter, we study the spin-wave resonance driven by the CITs, from which the exchange stiffness of NiMnSb is determined.

In Chapter 6, we extrapolate a new form of magnetoresistance in NiMnSb: unidirectional spin-orbit magnetoresistance (USOMR). USOMR scales linearly with the current and has opposite sign when the magnetization is reversed. Similar to the giant magnetoresistance in magnetic multilayers, USOMR can be used to distinguish between two opposite magnetization directions directly in the bulk of the ferromagnet.

# Declaration

I hereby declare that unless specified otherwise, the contents of this dissertation are original and have not been submitted in whole or in part for consideration for any other degree or qualification in this, or any other University. This dissertation is the result of my own work and includes nothing which is the outcome of work done in collaboration, except where specifically indicated in the text. This dissertation contains less than 60,000 words, including abstract, tables, footnotes and appendices.

Zhou Fang

2017

I would like to dedicate this thesis to my loving parents and wife…

# Acknowledgements

I would first like to offer my sincerest gratitude to my previous supervisor Dr. Andrew Ferguson for his kind guidance and tremendous supports on my PhD program. The transition from a master in Engineering to a PhD student in Physics was really challenging for me at the beginning, while he always treated me with huge patience and encouragement. In three-year time working with him, I gained much knowledge in physics inside and outside the textbook, and developed myself as an independent researcher. I do learn a lot about problem solving skills from him and gradually understand the importance of "creativity" in experimental physics, which was a word he wrote down to me in our first meeting.

I want to express my special appreciation to my recent supervisor Dr. Chiara Ciccarelli, who was also my advisor in the first three years, for her countless supports in my PhD life. She answered me academic questions, gave me advises on sample fabrications and measurements, trained me to use the wire bonding and argon ion miller, did proof reading on my paper and thesis, encouraged me when I felt disappointed, and so on. This thesis would not have been possible without her guidance and persistent help.

I hope to truly thank Prof. Henning Sirringhaus for his supervision. After Andrew left the group at the end of my third year, Henning became my supervisor for six months during Chiara's maternity period. He gave me crucial advises on my project and thesis writing, and patiently helped me solve many problems I faced in my final year. Additional appreciation is given to his work in running the microelectronics research centre, where I do enjoy the stimulating and positive working atmosphere in my four-year study.

My sincere thanks also goes to my previous group mate Dr. Vahe Tshitoyan for his assistance in using the electromagnet, device designing, sample fabrication, Matlab coding and so on. He also frequently discussed some challenging questions about Spintronics with me, from which I do gain a deeper understanding on my work.

I would like to expend my appreciation to Amy Westerman, Dr. Oscar Cespedes and Prof. Bryan Hickey from University of Leeds for providing me the YIG samples; Dr. Felicitas Gerhard, Dr. Charles Gould, and Prof. Laurens Molenkamp from Universität Würzburg for growing the NiMnSb samples for me; Dr. Leonid Abdurakhimov and Dr. Ron Mansell for their helps in ion milling; Dr. Radoslav Chakalov for the clean room training; Dr. Jakub Zelezny and Prof. Tomas Jungwirth from Institute of Physics, Academy of Sciences of the Czech Republic for building the theoretical background of the spin-orbit torque in NiMnSb and discussing the corresponding questions.

I do enjoy the life in microelectronics research centre. I appreciate my group mates Adam, Chiara, Fernando, Imtiaz, Nick, James, Riccardo, Stefan, Tim, Tomas and Vahe for their warm helps in and outside the academics, and the funny life outside the lab with them. I also want to thank the group administrators Emily, Emma, Julia and Vivian for their help for some group/department issues and Alex for his IT support.

# Contents

# List of Figures

# List of Tables

# List of Abbreviations

| | |
|---|---|
| AFM | Atomic force microscope |
| AMR | Anisotropic magnetoresistance |
| ANE | Anomalous Nernst effect |
| BIA | Bulk inversion asymmetry |
| CI-FMR | Current-induced ferromagnetic resonance |
| DRAM | Dynamic random-access memory |
| FMR | Ferromagnetic resonance |
| GMR | Giant magnetoresistance |
| HM | Heavy metal |
| IPA | Isopropyl alcohol |
| ISHE | Inversed spin Hall effect |
| LLG | Landau-Lifshitz-Gilbert |
| LMBE | Laser molecular beam epitaxy |
| MPE | Magnetic proximity effect |
| MRAM | Magnetic random-access memory |
| MRFS | Magnetron radio-frequency sputtering |
| MSBVW | Magnetostatic backward volume waves |
| MSFVW | Magnetostatic forward volume waves |
| MSSW | Magnetostatic surface spin wave |
| MSW | Magnetostatic spin waves |
| MTJ | Magnetic tunnel junctions |
| PCB | Printed circuit board |
| PLD | Pulse laser deposition |
| PSSW | Perpendicular standing spin wave |

| | |
|---|---|
| SEM | Scanning electron microscope |
| SHE | Spin Hall effect |
| SIA | Structure inversion asymmetry |
| SMR | Spin Hall magnetoresistance |
| SOC | Spin-orbit coupling |
| SOF | Spin-orbit field |
| SOT | Spin-orbit torque |
| SP | Spin pumping |
| SQUID | Superconducting quantum interference device |
| SR | Spin rectification |
| SSE | Spin Seebeck effect |
| ST-FMR | Spin-torque ferromagnetic resonance |
| STT | Spin-transfer torque |
| USMR | Unidirectional spin Hall magnetoresistance |
| USOMR | Unidirectional spin-orbit magnetoresistance |
| VSM | Vibrating sample magnetometer |

# Chapter 1 Introduction

Moore's law, which predicts that the number of transistors per unit area on an integrated circuit doubles every two years, has set the pace for the development of microelectronics for the past five decades. In 2014, Intel has developed the 14-nm technology by employing tri-gate transistors, and they are expected to continue reducing the node size to 10 nm in 2017. Further development, however, is serious challenging because of the problems from several aspects, such as power consumption, fabrication technology, device reliability and so on. Spintronics aims to address these challenges and bring up new solutions. Unlike conventional microelectronics where data transfer and processing are based on electron charges, spintronics exploits the electron spins as an additional degree of freedom to improve the efficiency of data storage and processing. Combining the advantages of integrated data processing, low power consumption and non-volatile storage capabilities, spintronics has been considered as one attractive route to redefine the conventional computation schemes.

In 1988, the discovery of giant magnetoresistance (GMR) by the groups led by Fert [1] and Grünberg [2] turned spintronics into a popular subfield of physics. For this reason, they were awarded the Nobel Prize in Physics in 2007. GMR was observed in multilayers consisting of alternating ferromagnetic and non-magnetic layers. The resistance of multilayers depends on the magnetizations of two adjacent ferromagnetic layers (in parallel or anti-parallel configurations). The use of GMR to build the read head of hard disks has led to a revolution in data storage technology over the last two decades. In the aspect of data writing, however, the magnetization switching still relies on an external magnetic field, which limits both the density of data storage and the device reliability.

The discovery of spin-transfer phenomenon has provided a promising way for data writing in spin valves. Spin-transfer torque (STT) was first studied theoretically by

Slonczewski [3] and Berger [4] in 1996. The magnetization of one ferromagnetic layer in spin valves is fixed (usually via exchange bias effect) while the other one's is free to be reoriented. Data is written by passing a DC current through the fixed layer, where the current becomes spin polarized and then transfers angular momentum to the free layer to switch its magnetization to either parallel or antiparallel with respect to the fixed layer's. Since the device is in spin-valve structure, the data can be easily read via the GMR, making STT a promising technique for magnetic random-access memory (MRAM). STT-MRAM was first reported in lab by Tsoi et al. in 1998 [5], and recently it has been commercialized by Hynix Inc. since 2008. As the data in STT-MRAM is written by charge current rather than the magnetic field, it has the potential to allow higher storage density and reliability than conventional MRAM. Together with non-volatility, low power consumption and compatibility with CMOS techniques, STT-MRAM has many potential applications in computers, radio frequency identification, mobile devices and so on. The disadvantages of STT-MRAM, however, include its requirement of current densities that are still too high for commercial standards, and the higher production cost compared to classical dynamic random-access memories (DRAM). New solutions need to be explored before STT-MRAM can be widely used or even replace the DRAM.

A recently explored possibility is to use spin-orbit torque (SOT) to switch the magnetization. SOT is a relativistic effect based on the spin-orbit coupling, which polarizes the electrons flowing in the materials. The polarization is independent on the direction of magnetization, and the flowing electrons can thus exchange angular momentum with the magnetization, and switch it to a specific direction. Unlike STTs which require an external fixed ferromagnetic layer to polarize the current, SOTs can take place not only in multilayer structures (Rashba effect) [6–9] but also in the bulk of materials with a zinc-blende crystalline structure (Dresselhaus effect) [10], making it more flexible for industrial applications. SOT has been well studied in the diluted magnetic semiconductor (Ga,Mn)As [11,12], and it has been proven to be an effective way to reversibly switch its magnetization [13,14]. Although the fabrication of (Ga,Mn)As is highly compatible with CMOS technology, the application is limited by its ferromagnetic critical temperature of

~170 K. It was not until 2016 that SOT was first observed in bulk NiMnSb at room temperature [15]. The research on this topic, however, is still at the early stage, and further work is required to understand the SOT in NiMnSb.

In this thesis, we report a series of current-induced ferromagnetic resonance (CI-FMR) studies for two types of devices, namely, YIG/heavy metal bilayers and NiMnSb thin films. The main purpose is to probe the magnetic properties of these materials and to measure the amplitude and the symmetry of the current-induced torques. All of the measurements in this thesis are carried out at room temperature.

After introducing the theoretical background in Chapter 2 and the experimental methods in Chapter 3, in Chapter 4 we discuss the CI-FMR measurement on a series of YIG samples of different thickness capped with either Pt or Ta. Unlike magnetic tunnel junctions where the spin angular momentum is carried by flowing electrons, in these bilayer structures, the angular momentum is carried by a pure spin current generated in the heavy metals via the spin Hall effect. In this way it can flow into the ferromagnetic insulator and exert a STT. The FMR in YIG can be electrically driven by either STT or Oersted field from the current flowing in the heavy metals, and their contributions are well` identified by a symmetry analysis of the FMR lineshape and its dependence on YIG thickness.

In Chapter 5, we study the current-induced SOT in NiMnSb thin films using the CI-FMR method. Similar to (Ga,Mn)As at low temperature [11,12], both field-like and antidamping-like SOTs were clearly observed in NiMnSb, but at room temperature. By comparing with the previous work in [15], we also found that not only the SOT but also the anisotropic magnetoresistance and magnetic anisotropy highly depend on the stoichiometry of NiMnSb. The spin wave resonance driven by SOT in NiMnSb was also investigated.

In Chapter 6, we report our discovery of the unidirectional spin-orbit magnetoresistance in bulk NiMnSb from CI-FMR measurement. We find that the sample resistance depends on the relative orientation between the magnetization and the non-equilibrium spin component of the carriers induced by spin-orbit coupling. This provides a method to detect magnetization switchings in bulk materials using a two-terminal geometry. Combined with the current-

induced SOT studied in Chapter 5, this result paves the way to build a SO-MRAM using bulk magnetic materials.

# Chapter 2 Theoretical background

This chapter presents the background theory and mathematics used in this thesis. We first discuss different magnetic energy terms in magnetic materials in order to understand the behaviour of the magnetization. Section 2.2 focuses on how the direction of the magnetization affects the transport properties and hence the resistivity of ferromagnetic materials (FM). Before discussing the reciprocal process on how charge transport through the FM can be used to manipulate its magnetic state, we give a brief introduction on magnetization dynamics and ferromagnetic resonance (FMR) in section 2.3, which can provide an effective tool to probe not only the magnetic properties but also the current-induced torques (CITs) in FMs. Finally, in section 2.4, we discuss two common CITs, namely spin-transfer torque (STT) and spin-orbit torque (SOT), together with a short literature review on probing CITs using FMR.

## 2.1 Magnetic energy and ordering

The magnetic moments in magnetic materials do not always align with the external magnetic field. Instead, there are several factors that affect the magnetic energy of the material, and the magnetic moments point to the direction where the total energy reaches a minimum. There are five contributions we usually consider when calculating the total energy of magnets at magnetostatic condition:

$$E_{total} = E_{Zeeman} + E_{ex} + E_{demag} + E_{mca} + E_{s} \tag{2.1}$$

where the five terms on the right-hand side refer to the Zeeman energy and the energy from the exchange interaction, shape anisotropy, magnetocrystalline anisotropy and surface anisotropy respectively.

### 2.1.1 Zeeman energy

The Zeeman energy is the potential energy held by a magnetic material when an external magnetic field $\mathbf{H}_{ext}$ is applied. Its mathematical expression is given by:

$$E_{Zeeman} = -\mu_0 \int_V \mathbf{M} \cdot \mathbf{H}_{ext} \mathrm{d}V \tag{2.2}$$

where $\mu_0 = 4\pi \times 10^{-7}$ H/m is the vacuum permeability; $\mathbf{M}$ is the vector of the local magnetization and $V$ is the sample volume. Clearly, the Zeeman energy is at its minimum when $\mathbf{M}$ aligns with $\mathbf{H}_{ext}$.

### 2.1.2 Exchange interaction

The exchange interaction is an electrostatic interaction in quantum mechanism which lies at the heart of the magnetic ordering. Since electrons are Fermions, the joint wave function of two electrons should be antisymmetric so that the Pauli exclusive principle is satisfied [16]. Therefore, both spatial and spin wave functions of a two-electron system can be either symmetric or antisymmetric, but always with opposite symmetry to each other, which results in a singlet state with total spin $S = 0$ and a triplet state with $S = 1$. By defining the energy of the two states as $E_S$ and $E_T$ respectively, we can model the exchange interaction between two electrons with spin $\mathbf{S}_1$ and $\mathbf{S}_2$ by a spin-Hamiltonian operator as:

$$\hat{\mathcal{H}}_{ex} = -\left(E_S - E_T\right)\mathbf{S}_1 \cdot \mathbf{S}_2 = -2J_{ex}\mathbf{S}_1 \cdot \mathbf{S}_2 \tag{2.3}$$

where $J_{ex} = (E_S - E_T)/2$ is the exchange constant. We can further apply this model to a many-body system by assuming that the exchange interaction is only effective between neighbouring atoms. This results in the Hamiltonian of the Heisenberg model [17]:

$$\hat{\mathcal{H}}_{ex} = -2\sum_{i>j}^{n} J_{ij}\mathbf{S}_i \cdot \mathbf{S}_j \tag{2.4}$$

where the coefficient $J_{ij}$ is the exchange constant between the $i^{th}$ and $j^{th}$ spins. Usually, it is valid to assume that $J_{ij}$ equals to a constant $J$ for neighbouring spins and equals to 0 otherwise [17]. Depending on the relative magnitude of $E_S$ and $E_T$, $J$ can be either positive or negative, resulting in ferromagnetic and antiferromagnetic ordering respectively. To determine the exchange energy in a ferromagnetic material, we need to replace the spins in Eq. (2.2) with a continuous unit magnetization $\mathbf{m} = \mathbf{M}/M_s$, where $M_s$ is the saturation magnetization, and integrate over the whole volume of the sample as:

$$E_{ex} = \frac{2JS^2 z}{a}\int_V (\nabla \mathbf{m})^2 \mathrm{d}V \tag{2.5}$$

where $a$ is the nearest neighbouring distance and $z$ is the number of sites in the unit cell.

### 2.1.3 Shape anisotropy

The shape anisotropy arises from the demagnetizing field inside the magnetic material and is due to the long-range magnetic interaction of the surface dipoles. The magnetic flux density can be determined by $\mathbf{B} = \mu_0(\mathbf{H} + \mathbf{M})$ inside the magnet. To satisfy the Maxwell equation ($\nabla \cdot \mathbf{B} = 0$) without any external magnetic field, there must be a demagnetization field inside the magnet such that:

$$\nabla \cdot \mathbf{H}_{demag} = -\nabla \cdot \mathbf{M} \tag{2.6}$$

The distribution of the demagnetization field is a complex function of the geometrical shape, but for an ellipsoidal shape, the demagnetizing field can be calculated and simplified to:

$$\mathbf{H}_{demag} = -\mathbf{N}\mathbf{M} \tag{2.7}$$

where $\mathbf{N}$ is the demagnetizing tensor, usually represented by a 3×3 matrix. When $\mathbf{M}$ is along one of the principal axes of the ellipse, the tensor can be expressed as:

$$\mathbf{N} = \begin{pmatrix} N_x & 0 & 0 \\ 0 & N_y & 0 \\ 0 & 0 & N_z \end{pmatrix} \tag{2.8}$$

where $N_x$, $N_y$ and $N_z$ are called the demagnetizing factors and satisfy $N_x + N_y + N_z = 1$. Similar to the Zeeman energy introduced in 2.1.1, we can also calculate the demagnetization energy by integrating the product of $\mathbf{H}_{demag}$ and $\mathbf{M}$ over the whole volume as:

$$E_{demag} = -\frac{\mu_0}{2}\int_V \mathbf{H}_{demag} \cdot \mathbf{M} dV \tag{2.9}$$

Therefore, there are preferred directions of $\mathbf{M}$ depending on the demagnetizing factors in order to minimize the value of $E_{demag}$.

### 2.1.4 Magnetocrystalline anisotropy

The magnetocrystalline anisotropy, in contrast to the shape anisotropy, originates from the spin-orbit coupling (SOC). Since the electron orbits in the lattice depend on the crystallographic structure of the material, there will be some well-defined crystallographic axes along which the electrons' spins prefer to align due to the SOC. Two common magnetocrystalline anisotropies considered in this thesis are the uniaxial and cubic anisotropy.

For the materials with a uniaxial anisotropy, the magnetization prefers to align in a single axis (called easy axis) in order to minimize the energy $E_{mca}$. In some hexagonal crystals like Co, the uniaxial anisotropy energy can be written as [18]:

$$\frac{E_{mca}}{V} = K_{u1}\sin^2\theta_u + K_{u2}\sin^4\theta_u + K_{u3}\sin^6\theta_u + \cdots \tag{2.10}$$

where $K_{ui}$ are the uniaxial anisotropy constants and $\theta_u$ is the angle between $\mathbf{M}$ and the stacking direction of the hexagonal crystal. When $K_{ui} > 0$, the angle $\theta_u$ needs to be zero to minimise the value of $E_{mca}$, indicating that the hexagonal axis is the easy axis; When $K_{ui} < 0$, $E_{mca}$ is minimal when $\theta_u = 90°$, and $\mathbf{M}$ is free to rotate in the hexagonal plane.

Cubic anisotropy usually appears in materials with cubic crystal structures, such as Fe and Ni, and the cubit anisotropy energy is given by:

$$\frac{E_{mca}}{V} = K_{c1}\left(\alpha_x^2\alpha_y^2 + \alpha_y^2\alpha_z^2 + \alpha_x^2\alpha_z^2\right) + K_{c2}\alpha_x^2\alpha_y^2\alpha_z^2 \tag{2.11}$$

where $K_{ci}$ are the cubic anisotropy constants and $\alpha_{x,y,z}$ are the direction cosines of **M** with respect to the three principal axes. The sixth order term $K_{c2}$ is negligible in most cases. Therefore, in some materials with $K_{c1} > 0$ (e.g. Fe), the easy axis is along the (100) crystalline direction or equivalent, while in other materials with $K_{c1} < 0$ (e.g. Ni), the easy axis is along the (111) direction.

### 2.1.5 Surface anisotropy

Surface anisotropy, also called interface out-of-plane anisotropy, is usually present in thin magnetic films, where the orbital motion of electrons is disturbed by the symmetry breaking at the interface. In some ultrathin films of a few nanometres thick, this term can even dominate the anisotropy of the samples. Phenomenologically, the surface anisotropy energy $E_s$ can be written as [19]:

$$\frac{E_s}{V} = \frac{K_s}{t_{film}}\sin^2\theta_s \tag{2.12}$$

where $K_s$ is the surface anisotropy constant depending on the interface roughness, while $t_{film}$ and $\theta_s$ are the film thickness and the angle between **M** and the surface normal respectively.

Finally, it is valuable to mention that, in order to compare the effects of the anisotropies introduced above with that of the external magnetic field or coercivity, we can define the anisotropy fields as [18]:

$$H_{ani} = \frac{2K_a}{\mu_0 M_s} \tag{2.13}$$

where $K_a$ is the corresponding anisotropy constant for different anisotropies.

## 2.2 Spin-dependent transport

Research on spin-dependent transport focuses on how the magnetic field or the magnetic properties of the system affects the scattering of carriers. The former case leads to the well-known Hall effect [20], while the latter case is diverse and constitutes one of the major area of study in spintronics. The scattering of carriers depends on the directions of the magnetization in FMs, which affects the resistance via a variety of different magnetoresistance. The SOC is also at the origin of the spin-dependent scattering of carriers in non-magnetic heavy metals, leading to the generation of spin currents via the spin Hall effect (SHE) [21]. Both topics will be discussed in this section.

### 2.2.1 Anisotropic magnetoresistance

The resistance of ferromagnetic metals depends on the orientation of the magnetization **M** with respect to that of charge current **I**. This phenomenon is called anisotropic magnetoresistance (AMR). In *3d* transition metals, where the *3d* band is not fully filled, AMR can be explained by a combination of *s-d* scattering and SOC. In these metals, the *sp* electrons are mainly responsible for the electron conduction (Mott's model) [22]. When a magnetic field is applied, some of the *sp* electrons are scattered to the *d* sub-bands, increasing the resistivity. The scattering cross-section depends on the orientation of the electrons' orbits. In one picture, due to the SOC, the electrons' orbits are either in the plane of the current when **I** $\perp$ **M** or perpendicular to the current when **I** // **M**, resulting in a small and a large scattering cross-section respectively, corresponding to a small and a large resistive state [23]. In the present of AMR, the resistance of the ferromagnetic metals and the AMR ratio can be respectively written as:

$$R = R_{\perp} + \left(R_{\parallel} - R_{\perp}\right)\cos^2\theta \tag{2.14}$$

$$\frac{\Delta R}{R_{av}} = \frac{R_{\parallel} - R_{\perp}}{\frac{1}{3}R_{\parallel} + \frac{2}{3}R_{\perp}} \tag{2.15}$$

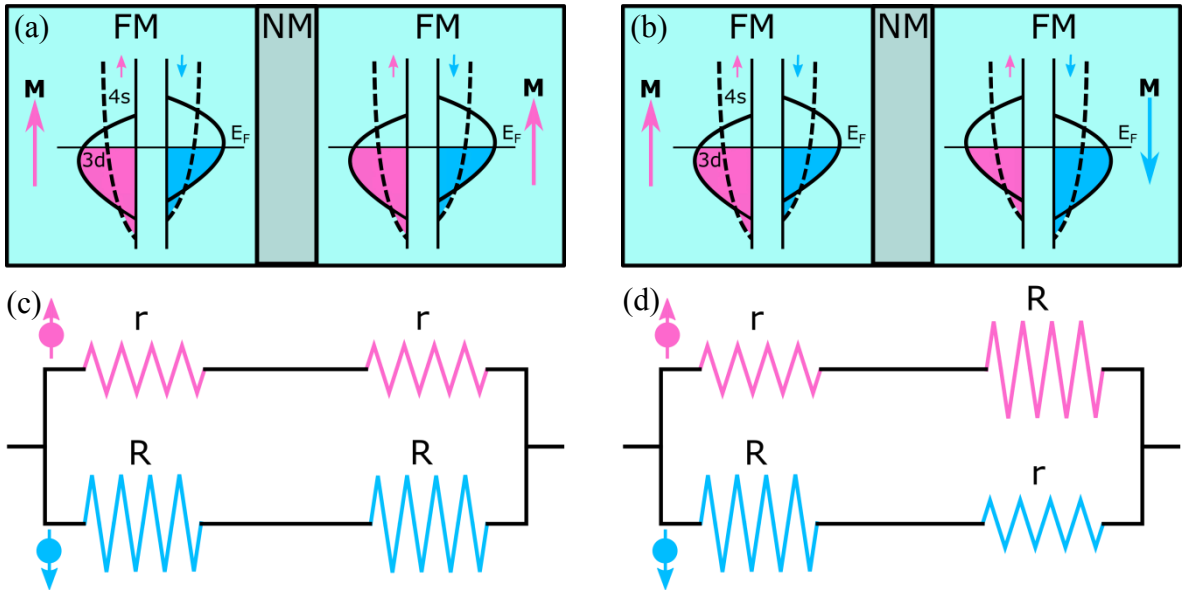


**Figure 2.1** Ferromagnetic/non-magnetic/ferromagnetic junctions with magnetizations in (a) parallel and (b) antiparallel configurations. The insets represent the density of states for the *3d* and *4s* sub-band for majority spin-up (pink) and minority spin-down (blue) electrons in the corresponding ferromagnetic layer. The corresponding "two-current model" circuit is shown in (c) and (d) for the parallel and antiparallel cases, where the electrons experiences a low resistive channel (labelled as "r") when the electron spins are parallel with **M**, and a high resistive channel (labelled as "R") when the spins and **M** are antiparallel.

where $\theta$ is the angle between **I** and **M**; $R_{//}$ and $R_{\perp}$ are the resistance when **I** // **M** and **I** $\perp$ **M** respectively. As explained above, most transition metals have a positive AMR ratio (i.e. $R_{//} > R_{\perp}$), while in some other materials such as (Ga,Mn)As, the AMR ratio can be negative (i.e. $R_{//} < R_{\perp}$) [15,24–26].

### 2.2.2 Giant magnetoresistance

Giant magnetoresistance (GMR) was first observed in a Fe/Cr/Fe junction [2] or $(Fe/Cr)_n$ multilayer structure [1], where the junction resistance was found to strongly depend on the relative magnetization directions (i.e. in parallel or antiparallel alignment) of adjacent Fe layers. Also, the behaviour of GMR can be explained by using Mott's model introduced in

the previous section [22], together with the "two-current model" [27] where the currents of majority spin-up electrons (with spins parallel to the magnetization **M**) and minority spin-down electrons (with spins antiparallel to **M**) are considered separately, and the spin-flip scattering is negligible. In *3d* transition metals, *4s* electrons are mainly responsible for the conduction, and the resistance is affected by the scattering between *4s* and *3d* energy bands. As shown in Figure 2.1 (a), if the magnetization of the metal is pointing "up", the *3d* density of state at the Fermi level is larger for the spin-down sub-band compared with the spin-up sub-band, resulting in a higher scattering rate, and hence a higher resistivity, for the spin-down electrons. Therefore, we can draw the "two-current model" circuits for the junctions with magnetizations in parallel and antiparallel configurations as shown Figure 2.1 (c) and (d) respectively. In the parallel case, the current with spin-up (spin-down) electrons experiences two low (high) resistive channel when flowing through the junction, which results in a lower overall resistivity compared with the antiparallel case, where the current for both spin-up and spin-down will flow through a high and low resistive channels.

### 2.2.3 Spin Hall effect and spin Hall magnetoresistance

The spin Hall effect is a transport phenomenon by which a charge current flowing through a material can generate a pure spin current in the transverse direction [21]. This phenomenon is usually observed in heavy metals [28–30] or semiconductors [31–33] and has been widely used for spin current generation [21,34,35]. The reciprocal process is called the inverse spin Hall effect (ISHE), where a pure spin current can be converted into a transverse charge current [36–38]. The origin of the SHE (and ISHE) is generally attributed to the SOC, while we can further identify three possible mechanisms: intrinsic [39,40], skew-scattering [41], and side-jump [42]. In the intrinsic SHE, we first assume that the sample film is grown in the x-y plane and an electric field is applied along the x-axis. Then, the electrons with momentums in the ±y-axis will experience an effective torque which can tilt their spins in opposite directions along the z-axis due to the Rashba SOC. In this way, a pure spin current is generated along the y-axis [40]. In contrast, both skew-scattering and side-jump mechanisms rely on the asymmetric scattering of impurities for different spins in the present

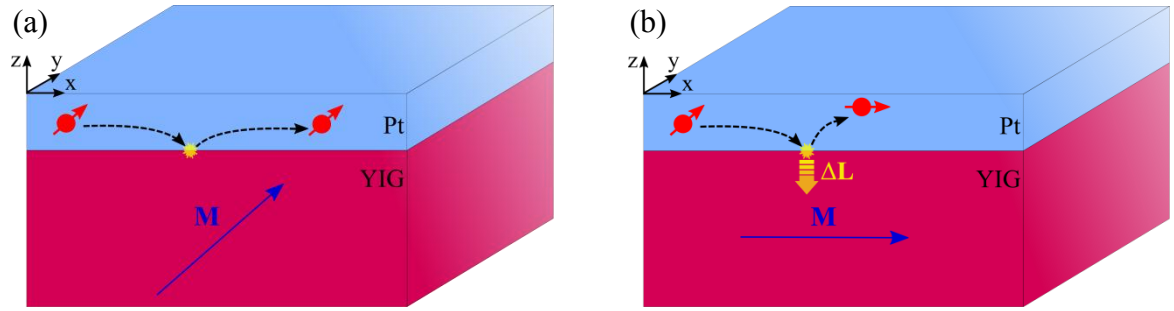


**Figure 2.2** Schematic illustration of the mechanism behind spin Hall magnetoresistance: (a) when **M** // y-axis, the spin polarization of the electrons at the interface is parallel to **M**, so that electrons are scattered back without angular momentum exchange with YIG; (b) when **M** // x-axis, the transverse component of the spin angular momentum $\Delta\mathbf{L}$ is absorbed by YIG, and electrons after the scattering are deflected away from the reflection path due to the ISHE. This effectively reduces the overall charge current, resulting in a larger resistivity compared to (a).

of SOC. For this reason, they are classified as the extrinsic mechanisms. The efficiency of the conversion between charge and spin currents is usually evaluated using a coefficient called spin Hall angle, which is defined as:

$$\vartheta_{SH} = \frac{J_s}{J_c} \tag{2.16}$$

where $J_c$ and $(\hbar/2e)J_s$ are the charge and spin current densities respectively. The value of $\vartheta_{SH}$ has been probed using different methods [43–50] and it can be either positive (i.e. Pt, Au and Ag) or negative (i.e. Ta, W and Mo) for different materials. However, experiments performed by different groups are still in disagreement by more than a factor of 20 as for its value [51].

The simultaneous action of the SHE and the ISHE in FM/heavy metal (HM) bilayer structures can result in a new magnetoresistance called the spin Hall magnetoresistance (SMR). It was first observed in YIG/Pt bilayers [30,49,50,52–54] and has now been reported in other bilayer systems [55–61]. As shown in Figure 2.2, the charge current in Pt along the x-axis generates a pure spin current via the SHE, which flows in the z-axis with spin

polarization parallel to the y-axis, resulting in a spin accumulation at the interface. At the interface, electrons will exchange angular moment with the YIG film via the STT, and will be scattered back into Pt with a spin orientation that depends on the relative direction of the magnetization in YIG and the electron spins before the scattering. Finally, the electrons being reflected at the interface will experience a deflection due to the ISHE, producing an additional current which can either enhance or reduce the original charge current and hence change the overall longitudinal resistivity.

Unlike AMR, where the magnetoresistance depends on the angle between the charge current (density) **J** and the magnetization **M**, SMR depends on the angle between the spin polarization at the interface $\boldsymbol{\sigma}$ ($\propto \mathbf{J} \times \mathbf{z}$) and **M**. Therefore, these two magnetoresistances are expected to have a different angle dependence when rotating the magnetization of the ferromagnet in the three principle planes in spatial coordinates. The AMR can be expressed as $\rho = \rho_x - (\rho_{yz} - \rho_x)(\mathbf{M} \cdot \mathbf{J})^2$, where $\rho_i$ represents the resistivity when **M** is saturated along the i-axis (or in the yz-plane for $\rho_{yz}$). We would expect that $\rho_y \approx \rho_z \neq \rho_x$ in AMR, and the resistance is a constant when **M** is in the y-z plane. In contrast, the SMR is characterised by $\rho_y < \rho_z \approx \rho_x$, and the resistance stays unchanged when **M** is rotated in the x-z plane where $\boldsymbol{\sigma}$ (along y-axis) is always perpendicular to **M**. From some recent theory on SMR [62], the maximum change in resistivity due to SMR can be calculated as:

$$\frac{\Delta\rho}{\rho} = \vartheta_{SH}^2 \frac{\lambda_{HM}}{t_{HM}} \mathrm{Re}\left[ \frac{2\lambda_{HM} G_{\uparrow\downarrow} \tanh^2\left(\frac{t_{HM}}{2\lambda_{HM}}\right)}{\frac{1}{\rho} + 2\lambda_{HM} G_{\uparrow\downarrow} \coth\left(\frac{t_{HM}}{\lambda_{HM}}\right)} \right] \tag{2.17}$$

where $\rho$ is the intrinsic electric resistivity; $G_{\uparrow\downarrow}$ is the interface spin mixing conductance; $t_{HM}$ and $\lambda_{HM}$ are the thickness and the spin diffusion lengths of the heavy metal respectively. Therefore, the value of $\vartheta_{SH}$ can be determined via a SMR measurement if $\lambda_{HM}$ and $G_{\uparrow\downarrow}$ are known. Finally, it is worth mentioning that since the SMR ratio is proportional to $\vartheta_{SH}^2$, the behaviour of SMR is independent on the sign of the spin Hall angle [30].

## 2.3 Magnetization dynamics

### 2.3.1 Ferromagnetic resonance

Ferromagnetic resonance is a spectroscopic technique that is widely used to probe the magnetic properties of ferromagnetic materials. To carry out a FMR experiment, we input microwave power to the ferromagnet mounted in a uniform magnetic field, and measure the corresponding response, i.e. power absorption, the rectified voltage along the sample bar and so on, near the resonance condition.

To explain the physics of FMR, we first introduce the model developed by Landau and Lifshitz in 1935, which describes the precessional motion of the magnetization when a (effective) magnetic field $\mathbf{H}_{\text{eff}}$ is applied [63]:

$$\frac{\mathrm{d}\mathbf{M}}{\mathrm{d}t} = -\mu_0\gamma_L \mathbf{M}\times\mathbf{H}_{eff} + \frac{\lambda}{M_s}\mathbf{M}\times\left(\mathbf{H}_{eff}\times\mathbf{M}\right) \tag{2.18}$$

$\gamma_L$ and $\lambda$ are the gyromagnetic ratio (for the Landau-Lifshitz equation) and the phenomenological damping parameter respectively. Later in 1955, Gilbert optimized equation (2.18) by introducing a different form of the damping term and got the well-known Landau-Lifshitz-Gilbert (LLG) equation [64]:

$$\frac{\mathrm{d}\mathbf{M}}{\mathrm{d}t} = -\mu_0\gamma \mathbf{M}\times\mathbf{H}_{eff} + \frac{\alpha}{M_s}\mathbf{M}\times\frac{\mathrm{d}\mathbf{M}}{\mathrm{d}t} \tag{2.19}$$

where $\alpha$ is the Gilbert damping coefficient. The first term in equation (2.19) is a torque which makes **M** rotate in an elliptical orbit around $\mathbf{H}_{\text{eff}}$. The second term (Gilbert damping term) represents a torque that tilts M towards $\mathbf{H}_{\text{eff}}$. These two equations are mathematically equivalent with $\gamma_L = \gamma/(1+\alpha^2)$ and $\lambda = \gamma\alpha/(1+\alpha^2)$ [65]. However, the Gilbert damping term is physically more meaningful, since it results in the convergence of the motion of magnetization (i.e. $\mathrm{d}\mathbf{M}/\mathrm{d}t \to 0$) in the limit of infinite damping ($\alpha \to \infty$).

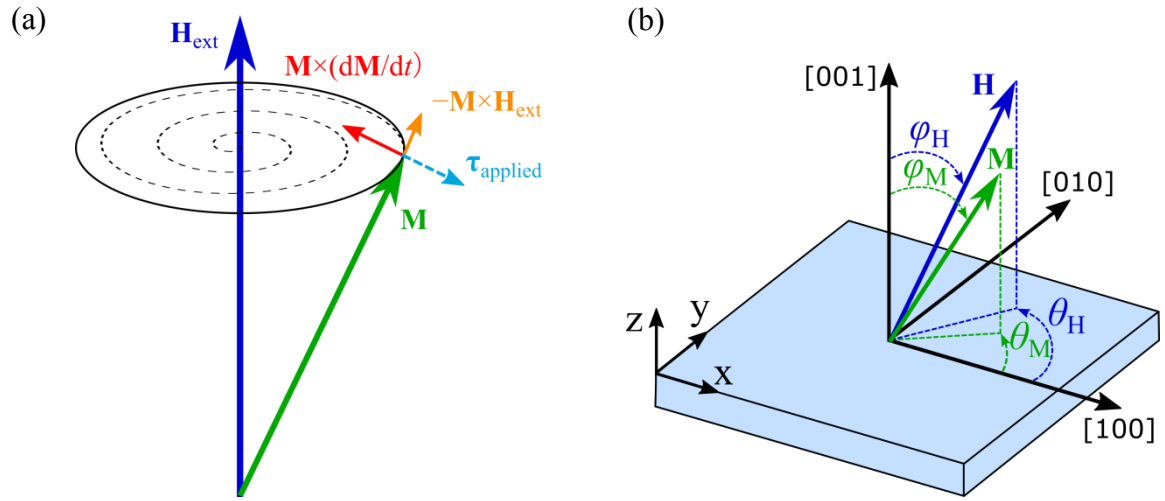


**Figure 2.3** (a) Schematic diagram of ferromagnetic resonance. (b) The coordinate system used for the deduction of Kittel's formula, where $\theta_H$ and $\theta_M$ are the angles between the [100] crystalline direction and the projection of **H** and **M** respectively in the x-y plane; $\varphi_H$ and $\varphi_M$ are the angles travelling from the [001] direction to **H** and **M** respectively

The mechanism of FMR can be understood from the LLG equation (2.19). The external magnetic field $\mathbf{H}_{ext}$ enters the first term of Eq. (2.19) which drives **M** to precess around $\mathbf{H}_{ext}$ in a circular path (solid circle in Figure 2.3(a)). The second term represents a damping torque. It turns the precessional path into a spiral shape (dashed line) and makes **M** align with $\mathbf{H}_{ext}$ in the end. FMR can be realized by compensating the damping with an additional torque (light blue arrow) so that the magnetization can keep precessing around $\mathbf{H}_{ext}$. In a conventional FMR experiment, this torque can be induced by applying a magnetic field at microwave frequency to the sample via either a coplanar waveguide or a microwave cavity [66–68]. More recently, researchers also input microwave charge current into the ferromagnetic materials and drive the FMR via the current-induced torques [11,47,69], which allows probing the ferromagnetic materials at nanoscales. From the magnetization dynamics, we are able to deduce magnitude and directions of the torque that has excited these dynamics.

In order to drive FMR, the frequency of the oscillating magnetic field is required to match that of the precessional motion of the magnetization. This provides a convenient link

between the magnetic properties we want to study and the microwave parameters we apply. The term $\mathbf{H}_{\text{eff}}$ in Eq. (2.18) represents the total effective magnetic field including the applied external field, the demagnetization field, and the crystalline anisotropic field, and it can be derived from the total magnetic energy $E$ of the sample by

$$\mathbf{H}_{eff} = \frac{\partial E}{V \partial \mathbf{M}} \tag{2.20}$$

where $V$ is the sample volume. Following the method in [70,71], the resonance frequency for any given field orientation (defined in Figure 2.3(b)) can be obtained by solving the equation:

$$\left(\frac{2\pi f}{\mu_0 \gamma}\right)^2 = \frac{1}{V^4 M_s^2 \sin^2 \psi_M}\left[\frac{\partial^2 E}{\partial \psi_M^2}\frac{\partial^2 E}{\partial \theta_M^2} - \left(\frac{\partial^2 E}{\partial \psi_M \partial \theta_M}\right)^2\right] \tag{2.21}$$

In this thesis, three energy terms are considered: the Zeeman term $E_{\text{Zeeman}}$, the demagnetization term $E_{\text{demag}}$ and the magnetic crystalline anisotropy term $E_{\text{mac}}$. Assuming that the bar is patterned along the [100] direction[1], these three terms can be written as:

$$\frac{E_{zeeman}}{V} = -M_s \cdot H_{ext}\left[\cos\psi_M \cos\psi_H + \sin\psi_M \sin\psi_H \cos(\theta_M - \theta_H)\right] \tag{2.22}$$

$$\frac{E_{demag}}{V} = \frac{1}{2} M_s^2 \left(N_x \sin^2\psi_M \cos^2\theta_M + N_y \sin^2\psi_M \sin^2\theta_M + N_z \cos^2\psi_M\right) \tag{2.23}$$

$$\frac{E_{mac}}{V} = -\frac{1}{2} M_s \left[H_{2\perp} \cos^2\psi_M + H_{2//} \sin^2\psi_M \sin^2\left(\theta_M - \frac{\pi}{4}\right) + \frac{1}{2} H_{4//} \frac{1}{4}\left(3 + \cos 4\theta_M\right)\sin^4\psi_M\right] \tag{2.24}$$

where $N_{x,y,z}$ are the demagnetization factors along the three principal axes; $H_{2\perp}$, $H_{2//}$, $H_{4//}$ are the out-of-plane anisotropy field, in-plane uniaxial and cubic anisotropy field respectively, which are related to the anisotropy energy by $H_i = 2K_i/M_s$. Since most of the measurements in this thesis limit $\mathbf{H}_{\text{ext}}$ to the film plane with the amplitude much larger than the anisotropy

[1] Otherwise, an offset in angle should be added when calculating the demagnetization energy, and the offset is determined by the pattering of the bar.

field, we can simplify our formulas by assuming $\psi_H = \psi_M = 90^o$ and $\theta_H = \theta_M = \theta$. Inputting Eq. (2.22)-(2.24) into (2.21), we obtain[2]:

$$f = \frac{\mu_0 \gamma}{2\pi} \sqrt{\left(H_{res} + H_1\right)\left(H_{res} + H_2\right)} \tag{2.25}$$

where

$$\begin{aligned} H_1 = M_s \left[ -N_x \cos^2\left(\theta + \phi\right) - N_y \sin^2\left(\theta + \phi\right) + N_z \right] - H_{2\perp} \\ + H_{2//} \sin^2\left(\theta - \frac{\pi}{4}\right) + \frac{1}{4} H_{4//} \left(3 + \cos 4\theta\right) \end{aligned} \tag{2.26}$$

$$H_2 = M_s \left(N_y - N_x\right) \cos 2\left(\theta + \phi\right) - H_{2//} \sin 2\theta + H_{4//} \cos 4\theta \tag{2.27}$$

We added a phase shift $\phi$ to the demagnetization term to extend our equation to bars patterned in any crystalline directions, since the demagnetization term is crystalline independent. Specifically, for an infinitely large thin film with negligible crystalline anisotropy[3], Eq. (2.25)-(2.27) reduce to the well-known Kittel's formula for the in-plane case [72]:

$$f = \frac{\mu_0 \gamma}{2\pi} \sqrt{H_{res}\left(H_{res} + M_{eff}\right)} \tag{2.28}$$

where $M_{eff} = M_s - H_{2\perp}$ is defined as the effective magnetization.

In addition to the dispersion relation, from which we can evaluate the gyromagnetic ratio and the magnetic anisotropy of the materials, we can use FMR to estimate the Gilbert damping coefficient $\alpha$ in the LLG equation by measuring the linewidth of the resonance $\Delta H$ as a function of the frequency:

[2] We call this equation as the modified Kittel's formula in this thesis.
[3] That is, $N_x = N_y = 0$ and $N_z = 1$; $\phi = 0$; $H_{2\perp} = H_{2//} = H_{4//} = 0$.

$$\Delta H = \Delta H_0 + \frac{2\pi f \alpha}{\mu_0 \gamma} \tag{2.29}$$

$\Delta H_0$ is the inhomogeneous linewidth caused by disorder. From Eq. (2.29), the value of $\Delta H_0$ and $\alpha$ can be determined by linearly fitting the dependence of the linewidth on resonance frequency and finding the values of the intercept and the slope respectively.

### 2.3.2 Spin wave resonance

In the last section, we explained FMR based on the solution of the LLG equation, which describes the magnetization dynamics for a homogeneously magnetized sample. In reality, there also exist higher-order resonance modes because of the generation of spin waves (i.e. spin wave resonance), where the precessional phase of magnetic moments varies periodically from point to point [73–75]. Spin wave resonances can be excited not only by an inhomogeneous RF field, but also even by a uniform RF field due to the lower symmetry of spins at the surface compared with the ones in the interior [73,75]. The wavevector of the spin wave is closely related to the amount of phase shift between neighbouring magnetic moments during precession, which is in turn determined by the mutual interaction between them. Depending on the type of interactions, namely dipole-dipole or exchange interaction, the spin waves are classified into magnetostatic spin waves (MSWs) with long wavelength ($k = 2\pi/\lambda < 10^6$ m$^{-1}$) and exchange spin waves with short wavelength respectively [76].

**Magnetostatic spin waves**

The MSWs were first observed in a non-uniformly excited YIG sphere by White and Solt in 1956 [74], and explained theoretically by Walker in 1958 [77]. In 1962, Damon and Eshbach theoretically analysed the MSWs in a ferromagnetic slab [78], and predicted three types of MSWs, depending on the direction of magnetization and the wavevectors.

- Magnetostatic surface spin wave (MSSW): MSSW modes (also called Damon-Eshbach mode) are observed when the magnetization is in the sample plane and perpendicular to

the wavevector. Limiting our discussion to thin films with negligible in-plane anisotropy, their dispersion relation is given by [79,80]:

$$\left(\frac{2\pi f}{\mu_0\gamma}\right)^2 = H_{res}\left(H_{res}+M_{eff}\right)+\frac{M_{eff}^2}{4}\left(1-e^{-2kt_{film}}\right) \tag{2.30}$$

where $t_{\mathrm{film}}$ is the film thickness. From Eq. (2.30), we know that the MSSWs are the forward wave (with group and phase velocity in the same direction) with their amplitude decaying exponentially from the film surface [81,82].

- Magnetostatic backward volume waves (MSBVW): MSBVW modes are observed when the magnetization in-plane and parallel to the wavevector. Unlike the MSSW modes, the MSBVWs are distributed almost uniformly throughout the sample volume. The dispersion relation can be approximately described as [81]:

$$\left(\frac{2\pi f}{\mu_0\gamma}\right)^2 = H_{res}\left[H_{res}+M_{eff}\left(\frac{1-e^{-kt_{film}}}{kt_{film}}\right)\right] \tag{2.31}$$

  Differently from the MSSW modes, MSBVWs have a negative group velocity with respect to the phase one.

- Magnetostatic forward volume waves (MSFVW): MSFVW modes are observed when the magnetization points out of the film plane while the wavevector stays in plane. Similar to the MSBVWs, MSFVMs are also uniform throughout the sample volume, but with positive group velocity. Its dispersion relation can be approximately expressed as [81]:

$$\left(\frac{2\pi f}{\mu_0\gamma}\right)^2 = H_{res}\left[H_{res}+M_{eff}\left(1-\frac{1-e^{-kt_{film}}}{kt_{film}}\right)\right] \tag{2.32}$$

**Perpendicular standing spin waves**

In thin ferromagnetic films with thickness in the range of nanometres, there also exist spin waves with wavevectors perpendicular to the film plane. Unlike the MSWs where the

wavevector stays inside the film plane and the wavelength can be chosen continuously, the perpendicular spin wave is confined by boundary conditions between the two surfaces. This implies that only standing spin waves with specific wavelengths are allowed to be excited. In this case, the spin wave has a very short wavelength, and the exchange interaction becomes dominant. Assuming that the spins are unpinned at the surface and the magnetization is in the film plane, one can give the dispersion relation of perpendicular standing spin waves (PSSW) as [80,83]:

$$\left(\frac{2\pi f}{\mu_0\gamma}\right)^2 = \left[H_{res} + \left(\frac{2A}{\mu_0 M_s}\right)k_{PSSW}\right]\left[H_{res} + M_{eff} + \left(\frac{2A}{\mu_0 M_s}\right)k_{PSSW}\right] \tag{2.33}$$

where $A$ is the exchange stiffness constant and $k_{\mathrm{PSSW}} = n\pi/t_{\mathrm{film}}$ is the wavevector of the $n$th-order PSSWs.

Finally, it is important to notice that for a given resonance field $H_{\mathrm{res}}$, both MSSW (Eq. (2.30)) and PSSW (Eq. (2.33)) modes require a microwave field with higher frequency with respect to the uniform FMR mode (Eq. (2.28)). In contrast, the resonance frequency required to excite MSBVW (Eq. (2.31)) modes is lower than the uniform mode[4]. The dispersion relations of all three modes converge to the Kittel's formula (Eq. (2.28)) for $k \to 0$, as expected.

## 2.4 Current-induced torques in ferromagnets

Opposite to the magnetoresistance, the charge current can also induce the motion of the magnetization by generating a torque. Recently, considerable progress has been made in the area of current-induced magnetization manipulation in the context of domain wall motion [7,84,85], magnetization switching [6,8,9,48,86–90], magnetic damping [91,92] and

[4] Since the magnetic field is applied in the film plane for all of the FMR experiment in this thesis, the MSFVW modes cannot be excited and are therefore not involved in this comparison.

FMR [11,47,93]. In this section, we will describe both STT, together with its Onsager's-reciprocity related effect (spin pumping), and SOT.

### 2.4.1 Spin-transfer torque and spin pumping

Spin-transfer torque was predicted theoretically by Slonczewski [3] and Berger [4] in 1996, and was first observed in devices with a spin-valve structure [5]. A spin-valve (Figure 2.4) consists of a fixed layer (F1) and a free layer (F2) of ferromagnetic materials, separated by a thin non-magnetic spacer. The current first flows though F1 where the magnetization is fixed, and electrons become polarized along $\mathbf{M}_{F1}$. After passing the non-magnetic spacer where spin-flip scattering is negligible, the electrons entering F2 are polarized again in the direction of $\mathbf{M}_{F2}$ [94]. In this process, angular momentum is exchanged between the electrons' spins and $\mathbf{M}_{F2}$, resulting in a torque that tilts $\mathbf{M}_{F2}$ towards $\mathbf{M}_{F1}$.

The STT contribution can be modelled by introducing two additional terms to the LLG equation (2.19) as [95–98]:

$$\frac{\mathrm{d}\mathbf{M}}{\mathrm{d}t} = -\mu_0\gamma\mathbf{M}\times\mathbf{H}_{eff} + \frac{\alpha}{M_s}\mathbf{M}\times\frac{\mathrm{d}\mathbf{M}}{\mathrm{d}t} + \frac{\hbar\gamma J_c P g_r^{\uparrow\downarrow}}{2eM_s t_{FM}}\mathbf{M}\times(\boldsymbol{\sigma}\times\mathbf{M}) - \frac{\hbar\gamma J_c P g_i^{\uparrow\downarrow}}{2eM_s t_{FM}}\mathbf{M}\times\boldsymbol{\sigma} \qquad (2.34)$$

where $g_{r(i)}^{\uparrow\downarrow}$ is the real (imaginary) part of the interface spin mixing conductance; $e$, $P$ and $t_{FM}$ are the elementary charge, the spin polarization factor and the thickness of the free ferromagnetic layer respectively; $\boldsymbol{\sigma}$ is the unit vector of the spin polarization. The third term is the Slonczewski's antidamping-like term [99], representing a torque which is always parallel or antiparallel to the damping torque depending of the spin polarization[5]. Therefore, the STT can either enhance or compensate the magnetic damping in magnetization dynamics, and the latter case provides us with a method for building spin auto-oscillators [91,100,101]. The fourth term is called the field-like term because the STT component in this format will

[5] This can be understood to compare the Slonczewski's term with the second (damping) term in Eq. (2.18), where they have the same format if $\boldsymbol{\sigma}$ // $\mathbf{H}_{eff}$.

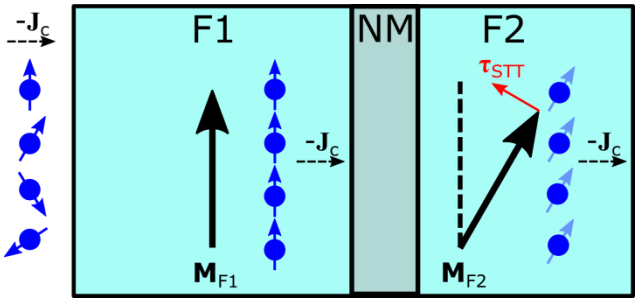


**Figure 2.4** Spin-transfer torque in a spin valve. When the electrons (in blue) flow through the fixed ferromagnetic layer F1, they are polarized along the magnetization of F1 ($\mathbf{M}_{F1}$). After passing the non-magnetic spacer, the electrons exchange angular momentum with the d-electrons in F2, exerting a torque (red arrow) on $\mathbf{M}_{F2}$.

behaves as an additional magnetic field along $\boldsymbol{\sigma}$. In most cases, the antidamping-like term dominates over the field-like term in FM/HM bilayers where $g_r^{\uparrow\downarrow} >> g_i^{\uparrow\downarrow}$ is satisfied [102,103].

**Spin pumping**

As introduced above, the spin current can drive the motion of the magnetization in FMs via STT. From Onsager's reciprocity relations, there exists a reciprocal process called spin pumping, where the magnetization precession in FMs leads to the emission of a pure spin current [98]. The theory of spin pumping was first developed Tserkovnyak et al. [104], where the pumped spin current is expressed as:

$$\frac{e}{\hbar}\mathbf{I}_s = g_r^{\uparrow\downarrow}\mathbf{M}\times\frac{\mathrm{d}\mathbf{M}}{\mathrm{d}t} + g_i^{\uparrow\downarrow}\frac{\mathrm{d}\mathbf{M}}{\mathrm{d}t} \tag{2.35}$$

The first term in Eq. (2.35) has the same format of the Gilbert damping term in the LLG equation (2.19), which implies that the spin pumping can cause an enhancement in the Gilbert damping by:

$$\alpha_{eff}\left(t_{FM}\right) = \alpha_0 + \alpha_{SP} = \alpha_0 + \frac{\gamma\hbar}{4\pi M_s t_{FM}} g_{reff}^{\uparrow\downarrow} \tag{2.36}$$

where $\alpha_0$ is the intrinsic damping factor, and $g_{\text{reff}}^{\uparrow\downarrow}$ is the effective real part of the spin mixing conductance taking the interface backflow of the spins into account [104,105]. This concept has been investigated both theoretically and experimentally [44,104,106–112]. The second term represents the reciprocal term of the field-like torque which effectively changes the value of the gyromagnetic ratio [98,104]. Since both γ and $\alpha$ can be easily extracted from the FMR measurement (details in section 2.3.1), spin pumping has been widely used not only for the generation of the pure spin current, but also as an effective way to probe the FM/HM interface properties [113].

**Literature review on spin-torque driven ferromagnetic resonance**

Before moving to the next section, we briefly review the previous work in probing STT based on FMR. One pioneer work was done by Tulapurkar et al. in 2005 who conducted a spin-torque ferromagnetic resonance (ST-FMR) experiment in a magnetic tunnel junction (MTJ) [69]. As shown in Figure 2.5 (a), the microwave current flowing through the pinned layer (CoFeB/Ru/CoFe trilayer at the bottom) becomes polarized and exerts a STT to the free layer on top, driving its magnetization into precession. At resonance, the junction resistance oscillates at the same frequency as the microwave current due to tunnel magnetoresistance, resulting in a rectified DC voltage across the MTJ. The lineshape of the DC resonance voltage (Figure 2.5 (b)) consists of a symmetric and an antisymmetric Lorentzian functions, where the antidamping-like and the field-like components of the STT can be extracted [69]. This device is also named spin-torque diode, as it transforms a microwave current into a DC voltage at resonance. A series of ST-FMR experiments in MTJs have then been reported with different device structures focusing on either understanding STT quantitatively for MRAM applications [114,115] or optimizing the devices for better performance [116–121]. Similar experiments were also extended to metallic spin valves [122–125]. The sensitivity of the spin-torque diode, defined as the detected DC rectified voltage over the input microwave power, can be enhanced by applying a DC voltage in parallel with the microwave to the sample [115,118,123]. In this way, the sensitivity has been improved to 75,400 mV/mW at room temperature after optimizing the MTJ structure [119], compared with the initial work of 1.4 mV/mW [69]. Furthermore, by controlling the perpendicular magnetic anisotropy of the

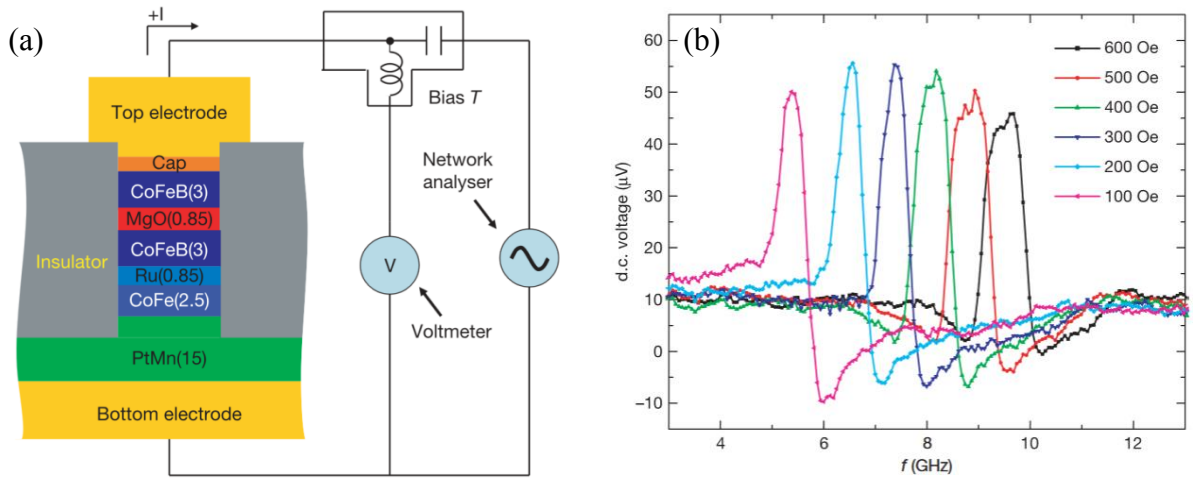


**Figure 2.5** (a) Setup of ST-FMR experiment and cross-sectional view of the MTJ. (b) The DC resonance voltage as a function of frequency at different external magnetic field. Figures are adapted from [69].

layers, the MTJ designed in [119] can operate without an external magnetic field, which largely reduces the size and the cost of the device. Although the rectified voltage in most ST-FMR is detected by a lock-in amplifier based on amplitude modulation, Gonçalves et al. have demonstrated that magnetic-field modulation can also be applied to measure ST-FMR in MTJs with a high degree of sensitivity, since it suppresses large non-magnetic background voltage [126]. This method is very effective in detecting weak rectified signals in ST-FMR experiment especially when a DC bias current is applied, since the rectified signal in this case will be hidden by the huge background generated by bolometric effects.

In addition to MTJs, ST-FMR can also be applied to bilayer structures consisting of a ferromagnetic thin film and a capping layer made by a heavy metal with strong SOC, like Pt, Ta or W. This technique was first developed by Liu et al. in a Py/Pt bilayer in 2011 [47]. In Figure 2.6 (a), the charge current in Pt along the x-axis generates a pure spin current flowing along the z-axis via the SHE, which exerts a STT to the magnetization **M** of Py and drives the precession. The current in Pt also generates an Oersted field (noted as $H_{rf}$ in figure) which also exerts an oscillating torque to the magnetization. Since the torques from STT and Oersted field are perpendicular to each other, they can be calculated separately by carrying a

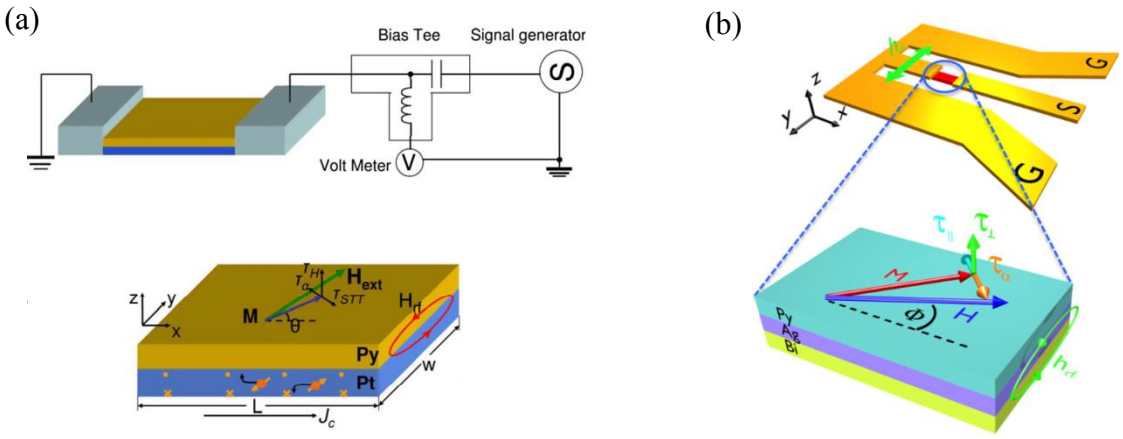


**Figure 2.6** (a) ST-FMR experimental setup (top) and structure of the Py/Pt bilayer (bottom). The magnetization of the Py is driven by the spin transfer torque $\tau_{STT}$, the torque $\tau_H$ induced by the Oersted field $H_{rf}$ and damping torque $\tau_\alpha$. (b) Experimental setup (top) and sample structure of Py/Ag/Bi trilayer (bottom). The Rashba effect at the Ag/Bi interface generates a spin current which exerts an in-plane STT on the Py, together with an out-of-plane torque generated by the Oersted field. Figure (a) and (b) are adapted from [47] and [127] respectively.

lineshape analysis of the resonance, where STT and Oersted field contribute to a symmetric ($V_{sym}$) and antisymmetric ($V_{asy}$) Lorentzian respectively. Moreover, because the torques which are exerted by the STT and the Oersted field are linear in the spin current and the charge current respectively, the spin Hall angle of Pt can be calculated to be 5.6% from the ratio between $V_{sym}$ and $V_{asy}$. Soon later, they also reported the giant spin Hall angle of 15% and 30% in β-Ta [48] and β-W [128] respectively using the same method. One advantage of this method is that the result is self-calibrated, as it is not necessary to know the current density in Pt [51]. Since then, a series of ST-FMR experiments have been done to either measure the spin Hal angle of heavy metals [129–131], analyse the current-induced torques [132–135] or probe the anisotropy of ferromagnets at nano-scales [59,136]. Recently, the ST-FMR method has been extended to topological-insulator/ferromagnet bilayers, demonstrating that the SHE in $Bi_2Se_3$ can efficiently manipulate the ferromagnet via STT [137,138]. In addition to the SHE, Jungfleisch et al. [127] reported that the spin current can be generated via the spin-orbit

interaction (Rashba effect) at the interface between Ag and Bi, which exerts a STT and drives the FMR in a Py/Ag/Bi trilayer device (Figure 2.6 (b)). Skinner et al. also reported a FMR measurement based on Rashba effect in the Co/Pt bilayers [93,139]. However, differently from the one in [127], the spin polarization from Rashba effect is generated directly at the interface of Co/Pt, so it drives the magnetization dynamics via the s-d scattering in the Py rather than a "transfer" process of the angular momentum from the adjacent Pt layer.

Similar to the case of MTJs, a DC bias current can be applied in parallel with the microwave to control the damping of the FM as shown in Figure 2.7 (a) [47,92,133,140,141]. Measuring the changes in damping as a function of DC bias current (Figure 2.7 (b)) provides an alternative way to estimate the spin Hall angle [47]. More importantly, we can estimate the threshold DC current required to fully compensate the damping, which paves the way in building spin auto-oscillators in FM/HM bilayer systems [91,101,142–145].

Since charge current in HM can generate pure spin current via SHE, it is possible to extend the ST-FMR method to ferromagnetic insulator.[6] Differently from the bilayers with ferromagnetic metals, the signal detection in YIG/Pt is based on the microwave current rectification by the SMR instead of the AMR [146]. In addition, as SMR is usually more than ten times smaller than AMR, the rectified voltage is relatively weak and the spin pumping voltage is no longer negligible when analysing the results. Recently, several groups have studied ST-FMR in YIG/Pt both theoretically [147–149] and experimentally [146,150,151]. Using the theoretical model built by Chiba [148], Schreier did the first experiment of in-plane CI-FMR in YIG/Pt and identified the current-induced torque from the symmetry and the lineshape of the resonance [146]. Sklenar then repeated the experiment but with the external magnetic field out of the film plane [150]. Very recently, Jungfleisch imaged the current-driven magnetization precession in YIG/Pt at resonance condition with Brillouin light scattering spectroscopy and argued that uniform precession is no longer applicable at high microwave power [151]. Despite these, the behaviour of CI-FMR in YIG/HM should strongly

[6] Part of this paragraph is published on: Z. Fang et al., *Appl. Phys. Lett.* **110**, 092403 (2017).

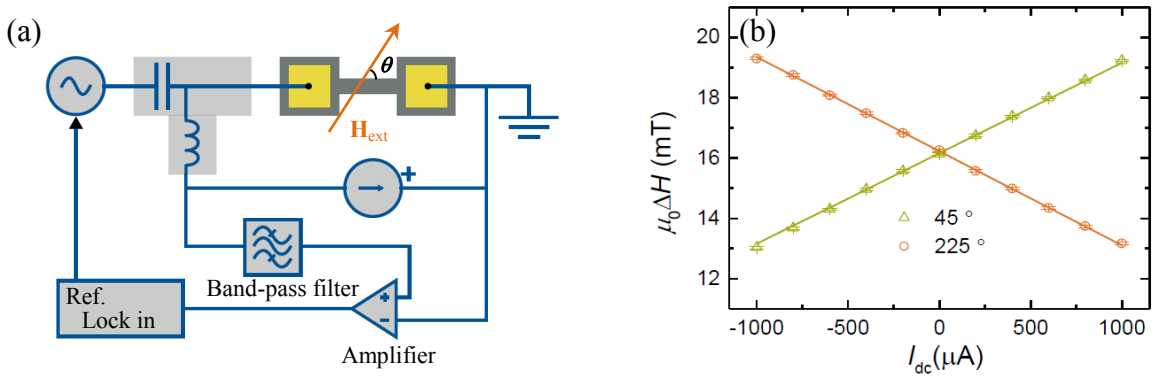


**Figure 2.7** (a) ST-FMR experimental setup with DC bias current. (b) Resonance linewidth as a function of DC bias current at $\theta$ = 45° and 225°. Both show a linear behaviour with opposite gradient. Figures are adapted from [141].

depend on the thickness of the films [147], while there is a lack of detailed study on this topic. This study is one of the results of this thesis described in Chapter 4.

### 2.4.2 Spin-orbit torque

Spin-orbit coupling is a relativistic effect by which the spin of an electron is coupled to its motion. As explained before, it is at the origin of several important spintronic phenomena, like AMR, SHE, SMR, anomalous Hall effect, magnetic anisotropy and so on. Furthermore, in ferromagnetic materials lacking of symmetry at interface (i.e. Pt/Co/$AlO_x$ [6,90]) or in crystalline structure (i.e. (Ga,Mn)As [11,14]), charge current leads to a spin accumulation because of the SOC, which can induce a torque to the local magnetization via the s-d scattering if the spins and the magnetization are not aligned [152,153]. This torque is named spin-orbit torque. Distinct from STT, which is based on the angular momentum "transfer" between the fixed and the free layer, SOT is a relativistic phenomenon, and the torque is induced uniformly inside the spin-orbit coupled ferromagnet without the need of an external polarizer [24].

We start by explaining the mechanism of SOC. Consider a hydrogen atom where the electron orbits the nucleus at a velocity **v**. According to special relativity, we can look at this

system from the rest frame of the electron with the nucleus orbiting the electron at the same velocity. Since the nucleus carries positive charge, the orbiting of the nucleus constitutes a circular current, which generates a magnetic field **B** on the electron. From a Lorentz transformation between electric and magnetic fields, the field **B** can be written as [17]:

$$\mathbf{B} = -\frac{\mathbf{v}\times\mathbf{E}}{c^2} \tag{2.37}$$

where $c$ is the speed of light and **E** is the electric field at the electron generated by the nucleus:

$$\mathbf{E} = -\frac{\mathbf{r}}{r}\frac{\mathrm{d}V(r)}{\mathrm{d}r} \tag{2.38}$$

$V(r)$ is the potential energy; **r** and r are the position vector of the electron and its magnitude. This effective magnetic field interacts with the electron magnetic moment **m** and contributes with an additional term to the electron's Hamiltonian as:

$$\hat{\mathcal{H}}_{SO} = -\frac{1}{2}\mathbf{m}\times\mathbf{B} = \frac{e}{2m_e^2c^2r}\frac{\mathrm{d}V(r)}{\mathrm{d}r}\mathbf{S}\cdot\mathbf{L} \tag{2.39}$$

$m_e$ is the electron's rest mass; **S** and **L** are the spin and orbital angular momentum with $\mathbf{S} = m_e\mathbf{m}/e$ and $\mathbf{L} = m_e\mathbf{r}\times\mathbf{v}$; the factor ½ in Eq. (2.39) is the Thomas factor for the relativistic correction. This equation is only applicable for one-atom system. For an electron in a lattice, the SOC term is usually written as:

$$\hat{\mathcal{H}}_{SO} = \frac{e\hbar}{4m_e^2c^2}\left[\nabla V(\mathbf{r})\times\mathbf{p}\right]\cdot\boldsymbol{\sigma} \tag{2.40}$$

where **p** is the momentum operator and $\boldsymbol{\sigma} = 2\mathbf{S}/\hbar$ is the Pauli spin operator.

The spin-splitting in materials via SOC only occurs when the inversion symmetry is broken in the system. This is because the Hamiltonian in Eq. (2.40) preserves the time-

reversal symmetry, which means that for the electrons with spin up ↑ (or down ↓) and wavevector **k**, the energy eigenvalue must satisfy [154]:

$$E_{\uparrow(\downarrow)}(\mathbf{k}) = E_{\downarrow(\uparrow)}(-\mathbf{k}) \tag{2.41}$$

This is called the Kramers degeneracy. If the system is inversion asymmetric, we have:

$$E_{\uparrow(\downarrow)}(\mathbf{k}) \neq E_{\uparrow(\downarrow)}(-\mathbf{k}) \tag{2.42}$$

By comparing (2.42) with (2.41), we obtain:

$$E_{\uparrow(\downarrow)}(\mathbf{k}) \neq E_{\downarrow(\uparrow)}(\mathbf{k}) \tag{2.43}$$

This means that the spin degeneracy is lifted.

There are generally two ways in which the inversion symmetry can be broken, namely by structure inversion asymmetry (SIA) and bulk inversion asymmetry (BIA). SIA was proposed by Rashba in 1960 [155], where the inversion symmetry is broken in heterostructures along the growth direction [156]. The Hamiltonian for the SOC in materials with SIA along the z-axis can be written as [157,158]:

$$\hat{\mathcal{H}}_R = \frac{\alpha_R}{\hbar}(\mathbf{z}\times\mathbf{k})\cdot\boldsymbol{\sigma} \tag{2.44}$$

where $\alpha_R$ is called the Rashba coefficient. In deformed crystals, however, SOC Hamiltonian is modified by the uniform strain [159], where the strain can be represented by the Cauchy strain tensor **ε**:

$$\varepsilon_{ij} = \frac{1}{2}\left(\frac{\partial u_i}{\partial r_j} + \frac{\partial u_j}{\partial r_i}\right) \tag{2.45}$$

The $\mathbf{r} = (r_x, r_y, r_z)$ is the atom's equilibrium position in crystals and $\mathbf{u}(\mathbf{r})$ is the displacement vector, with the parameters $i, j$ = x, y or z. For the Rashba term, the off-diagonal strain elements (called the shear strain) enter the Hamiltonian as [160]:

$$\hat{\mathcal{H}}_R = \frac{\alpha_R}{\hbar}\left[\left(\varepsilon_{zx}k_z - \varepsilon_{xy}k_y\right)\sigma_x + \left(\varepsilon_{xy}k_x - \varepsilon_{yz}k_z\right)\sigma_y + \left(\varepsilon_{yz}k_y - \varepsilon_{zx}k_x\right)\sigma_z\right] \tag{2.46}$$

In contrast, BIA proposed by Dresselhaus in 1955 [161] usually appears in crystals with a zinc-blende structure, which lacks a centre of inversion. In this case, the symmetry is broken directly by the bulk unit cell without the need of adjacent layers. Without strain, the Hamiltonian for the Dresselhaus-type SOC has a cubic form:

$$\hat{\mathcal{H}}_{D3} = \frac{\gamma}{\hbar}\left[k_x\left(k_y^2 - k_z^2\right)\sigma_x + k_y\left(k_z^2 - k_x^2\right)\sigma_y + k_z\left(k_x^2 - k_y^2\right)\sigma_z\right] \tag{2.47}$$

Once strain is applied, the on-diagonal strain elements (called the tetragonal strain) enter the equation. The Hamiltonian in Eq. (2.47) reduces to a linear form [162]:

$$\hat{\mathcal{H}}_{D1} = \frac{\beta_D}{\hbar}\left[\left(\varepsilon_{yy} - \varepsilon_{zz}\right)k_x\sigma_x + \left(\varepsilon_{zz} - \varepsilon_{xx}\right)k_y\sigma_y + \left(\varepsilon_{xx} - \varepsilon_{yy}\right)k_z\sigma_z\right] \tag{2.48}$$

In analogy to the Zeeman coupling, we can rewrite the Hamiltonian of the SOC as:

$$\hat{\mathcal{H}}_{SO} = \frac{\hbar}{2}\mathbf{\Omega}(\mathbf{k})\cdot\boldsymbol{\sigma} \tag{2.49}$$

where $\mathbf{\Omega}(\mathbf{k})$ the precession vector. Therefore, the effect from the SOC on the electron spins can be treated as an effective magnetic field in parallel with $\mathbf{\Omega}(\mathbf{k})$. Specifically, in some magnetic materials with zinc-blende crystalline structure, i.e. (Ga,Mn)As, the strain can introduce an addition term, which is known as $C_4$ martix element, into the Hamiltonian, and the expression becomes [11,163]:

$$\hat{\mathcal{H}}_{C4}(\varepsilon) = C_4\sum_i J_i k_i\left(\varepsilon_{i+1i+1} - \varepsilon_{i+2i+2}\right) + C_4\sum_i\left(J_i k_{i+1} - J_{i+1}k_i\right)\varepsilon_{ii+1} \tag{2.50}$$

Here, **J** is the hole total angular momentum operator for (Ga,Mn)As and $C_4$ is a constant. The first term in (2.50) represents a Dresselhuas-type spin-orbit field (SOF) resulting from a lattice mismatch (between (Ga,Mn)As and substrate) growth strain, i.e. $\varepsilon_{xx} = \varepsilon_{yy} \neq \varepsilon_{zz}$. The second term yields the Rashba-type SOF, and its origin can be modelled as a shear strain as

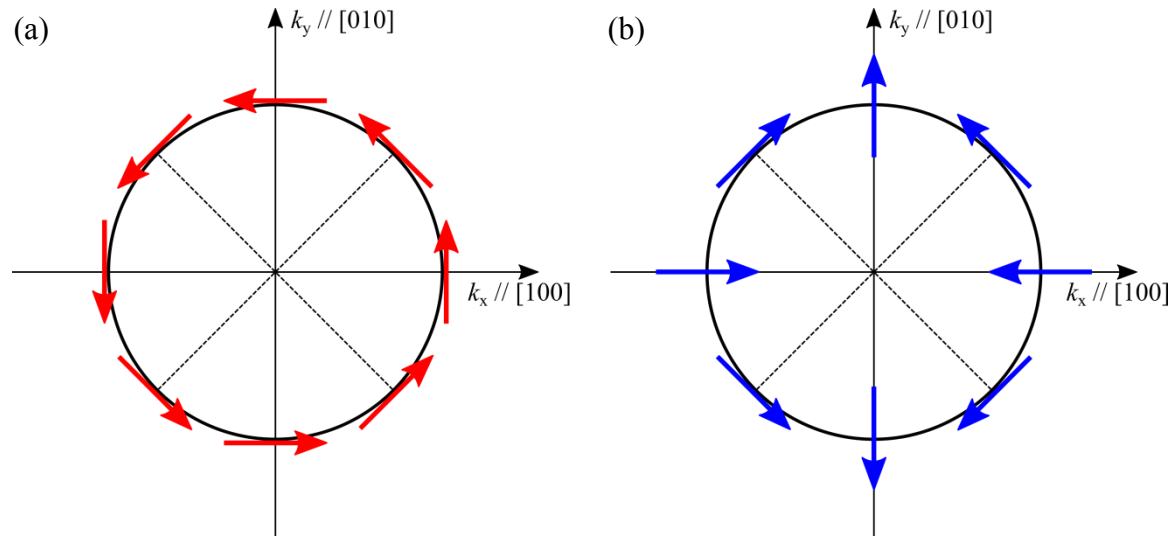


**Figure 2.8** Polar plot of the (a) Rashba and (b) Dresselhaus spin-orbit field in **k**-space.

$\varepsilon_{xy} = \varepsilon_{yx} \neq 0$, though this strain does not physically exist here [11]. We can plot the symmetry of the effective field from the Rashba and Dresselhaus SOC as shown in Figure 2.8. It can be seen that the Dresselhaus field strongly depends on the directions of the charge current with respect to the crystalline directions, while this is not true for the Rashba field which is always perpendicular to the current flowing in the x-y plane. In our thesis, we focuses on NiMnSb, whose crystalline structure falls in the same symmetry group as (Ga,Mn)As, so we can write the same Hamiltonian[7] dependent on the strain tensor **ε**.

Because of the SOF, when a charge current is flowing in an inversion-asymmetric material, a non-equilibrium spin polarization is induced in the direction of the SOF. This is called the inversed spin-galvanic effect [164,165]. When this effect is present in ferromagnetic materials, the induced spin polarization interacts with the magnetization and induces torques on it, which take the name of SOT [11,14,93,166].

[7] We need to replace the hole total angular momentum operator with that of the electron.

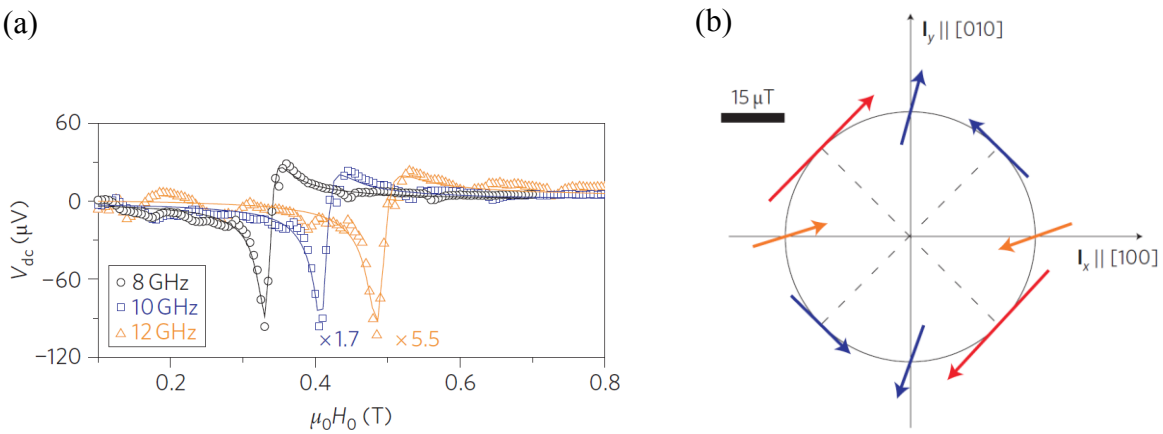


**Figure 2.9** (a) DC resonance voltage as a function of external field at different frequencies, measured in (Ga,Mn)As using SO-FMR. (b) Polar plot of the spin-orbit effective field in (Ga,Mn)As along different crystalline directions, normalized to a current density of $10^9$ A/m$^2$. Figures are adapted from [11].

**Literature review on spin-orbit driven ferromagnetic resonance**

We end up this section by reviewing the progress in probing SOT using FMR method. In 2011, Fang et al. first developed the spin-orbit driven FMR (SO-FMR) in bulk diluted magnetic semiconductor (Ga,Mn)As and (Ga,Mn)(As,P) with inversion asymmetry at low temperature of 6 K [11]. The experimental setup of SO-FMR is the same as the one in Figure 2.7 (a). Resonance signal generated by spin rectification can be observed for a wide range of frequencies (Figure 2.9 (a)), and the detected voltage consists of a symmetric ($V_{sym}$) and an antisymmetric Lorentzian lineshape ($V_{asy}$). Similar to the case in ST-FMR, these two components are determined by the antidamping-like and field-like torques respectively. The field-like SOTs observed in (Ga,Mn)As consists of both Rashba and Dresselhaus symmetries (Figure 2.9 (b)), and their amplitude can be estimated separately by measuring the angle dependence of $V_{asy}$ in the bars along different crystalline directions. However, the physical origin of $V_{sym}$ was not well understood at that time. Since there is no angular-momentum transfer between the materials and the outside, SO-FMR allows us to precisely probe the magnetic properties of the samples in the bulk structure.

Later, Kurebayashi et al. applied the same method to probe the SOTs in (Ga,Mn)As, from which they explained $V_{sym}$ as the result of a current-induced antidamping-like SOT originating from the Berry curvature [12]. During the acceleration of carriers between the scattering events, the effective SOF $\mathbf{h}_{SO}$ acquires a time-dependent component since $\mathbf{h}_{SO} \propto \mathbf{k}$. This leads to a small tilt of the spins from equilibrium, resulting in an out-of-plane component which induces an antidamping-like torque on the magnetization [12,167,168]. This antidamping-like torque can be comparable in amplitude with the field-like torque, and therefore should also be considered when probing the SOT in ferromagnetic materials [12].

Recently, Ciccarelli et al. has extended this method to the half-Heusler alloy NiMnSb, and this is the first time that the SOT is detected in bulk materials at room temperature [15]. However, more work is required in order to understand the SOTs in NiMnSb, and this is one of the objectives in this thesis as described in Chapter 5.

# Chapter 3 Devices and experimental setup

This chapter presents the experimental techniques employed in this thesis. It starts by describing the fabrication of $Y_3Fe_5O_{12}$/heavy metal (YIG/HM) and NiMnSb samples, followed by the patterning and post-processing. The experimental methods that involve the use of an electromagnet system will be introduced at the end of the chapter.

## 3.1 Sample film growing

### 3.1.1 Preparation of YIG/heavy metal bilayers

The YIG/HM samples used in this thesis were prepared by A. Westerman from the University of Leeds. A range of YIG films with a thickness of 8.2~80 nm were grown using RF sputtering on substrates of (111) gadolinium gallium garnet and at a pressure of 2.4 mTorr. Since the sputtered YIG was nonmagnetic at this stage, the films were annealed *ex situ* at 850˚C for 2 hours. An overlayer of 4.2 ± 0.1 nm Pt (or 5.0 ± 0.1 nm Ta) was then deposited via DC magnetron sputtering. Both YIG and Pt (or Ta) thicknesses were measured by x-ray reflectivity.

### 3.1.2 Preparation of NiMnSb samples

The NiMnSb samples were prepared by F. Gerhard from the Universität Würzburg. A 200 ± 5-nm thick (In,Ga)As film was first grown on Fe:InP insulating substrates as a buffer layer using molecular beam epitaxy. A layer of 34 ± 1-nm thick NiMnSb was then grown without breaking the vacuum and capped by a 5-nm layer of MgO to avoid oxidation. The lattices of (In,Ga)As and NiMnSb are well matched and the small mismatch (~0.6%) between

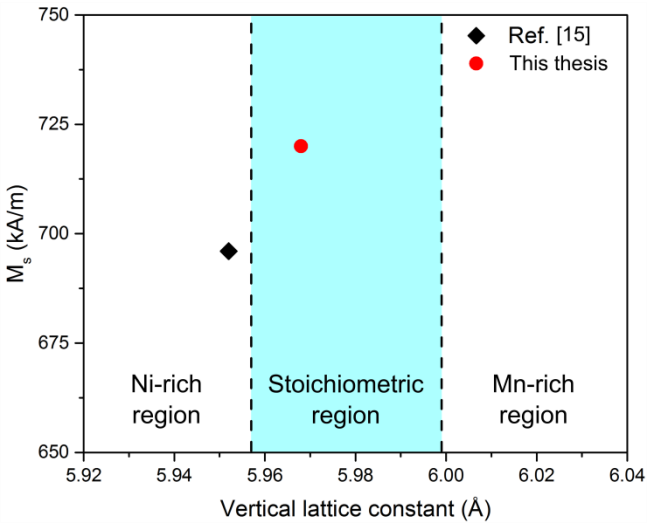


**Figure 3.1** Saturation magnetization of the sample in this thesis and the one in [15] as a function of Mn concentrations gauged by the vertical lattice constant. The light blue region is where the NiMnSb is expected to be stoichiometric.

the NiMnSb and the InP generates a compressive strain to both (In,Ga)As and NiMnSb layers [169,170]. It has been confirmed that this strain relaxes little for NiMnSb films that are thinner than 40 nm [170]. The saturation magnetization $M_s$ was measured to be ~716 kA/m using superconducting quantum interference device (SQUID).[8]

According to [171], the vertical lattice constant of $Ni_{1-x}Mn_{1+x}Sb$ increases linearly with its Mn composition (i.e. the value of $x$). Therefore, we can estimate the sample stoichiometry by probing the vertical lattice constant of NiMnSb via high resolution X-ray diffraction. As shown in Figure 3.1, the vertical lattice constant of the NiMnSb sample in this thesis was measured to be 5.968 Å, which is within the on-stoichiometric range (5.957 ~ 5.999 Å), while the lower and higher regions corresponding to Ni-rich and Mn-rich samples [172]. In contrast, the vertical lattice constant of NiMnSb in [15] is 5.951 Å (and $M_s$ ~ 695 kA/m), which corresponds to an off-stoichiometric Ni-rich sample.

[8] The SQUID and X-ray diffraction was done by F. Gerhard from the Universität Würzburg.

## 3.2 Sample patterning

### 3.2.1 Patterning YIG/heavy metal bilayers

**Photolithography** — A micrograph of a 5×50 $\mu m^2$ bar with gold pads on a YIG(62)/Pt(4.2) sample is shown in Figure 3.2 (a). Photolithography and ion milling were first used to pattern the YIG/HM samples into 5×50 $\mu m^2$ bars. The sample surface was first cleaned with acetone and then isopropyl alcohol (IPA) in an ultrasonic bath, both for one minute. After drying the surface with the nitrogen spray gun, the samples were spin-coated with Microposit S1813 at 5000 rpm for 1 minute and baked in an oven at 85°C for 30 minutes. The samples were then exposed to ultraviolet light via a self-designed photomask for 12 seconds. Finally, the samples were developed in Microposit MF319 for 35 seconds and rinsed in de-ionized water for 1 minute.

**Ion milling** — With the developed photoresist on top, the YIG/HM samples were patterned into bar structures by argon ion milling[9]. The samples were put into a chamber filled with argon gas. The argon gas was first ionized by the accelerated electrons emitted by a hot filament at the top of the chamber. The argon ions were then accelerated under an electrical potential of 1000 V and bombard the sample surface, etching the area that was not protected by resist[10]. The beam current was kept at 22 mA for the whole milling process. Finally, the samples were left in acetone for 7 hours to remove the resist. The overall ion milling rate was estimated to be 8~9 nm/s and milling for 10 minutes was enough to remove the YIG/HM bilayers and penetrate into the GGG layer for all samples. This was confirmed by measurement with the atomic force microscope (AFM), where a 10-minute milling on sample YIG(62)/Pt(4.2) approximately resulted in a 90-nm step between the milled and un-milled areas (Figure 3.2 (b)).

[9] Ion milling for the YIG/HM samples was carried out with the help of C. Ciccarelli and L. Abdurakhimov.

[10] The ion milling machine used for YIG/HM patterning suffered from some technical hitches. Higher beam voltage and current were required to achieve acceptable milling rate.

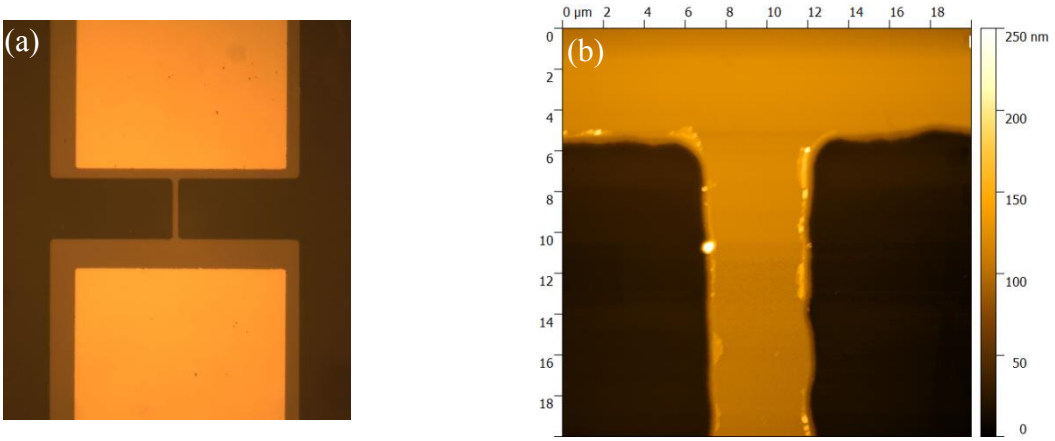


**Figure 3.2** (a) Optical micrograph of a 5×50 $\mu m^2$ bar on patterned YIG(62)/Pt(4.2). The light yellow regions are gold pads. (b) The zoom-in AFM image of the same bar.

**Contact pad evaporation** — Since the HM layer is very thin, it is necessary to grow additional contact pads to allow wire bonding. The photolithography step introduced above was applied to define the contact pad regions. After being developed, the samples were loaded into the chamber of a thermal evaporator. The chamber was then evacuated to a low pressure of 1~3 × $10^{-7}$ mbar. A 5-nm Cr buffer layer was first evaporated at a rate of 1 Å/s in order to improve the adhesion, followed by the evaporation of 50-nm thick Au layer at a rate of 2.5 Å/s. Finally, the samples were immersed in acetone for at least 7 hours for lift-off, followed by an ultrasonic bath of 3 seconds to remove any residual photoresist.

### 3.2.2 Patterning NiMnSb samples

**E-beam lithography** — The dimension of the bars patterned on the NiMnSb film is close to the resolution limit of the photolithography available in our clean room (3 ~ 4.4 µm). For this reason, in order to get more precise structures and better edge quality, electron-beam lithography was applied to pattern the NiMnSb samples. The samples were first cleaned by

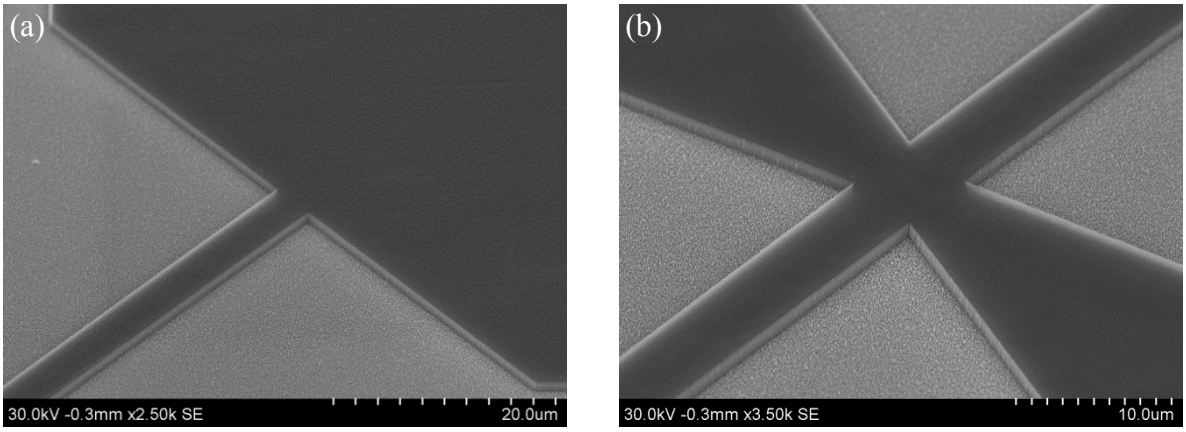


**Figure 3.3** SEM images of (a) a 4×40 μm$^2$ bar (the area near the pad) and (b) a 5×250 μm$^2$ cross-bar (the central region) with a tilting angle of 40 degree.

immersing them in acetone and IPA. Ultrasonic bath should be avoided since the InP substrate is mechanically fragile, while $O_2$ plasma process was also omitted to avoid oxidizing the NiMnSb film. In order to mill beyond the 200-nm (In,Ga)As seed layer, the samples had to be milled deeper than 240 nm. In order to better protect the sample surface, a negative resist Microresist Ma-N 2410 rather than PMMA was used. A layer of Ma-N 2410 was spun on NiMnSb at 7500 rpm for 1 minute. Then the samples were baked on a hot plate at 90 °C for 2 minutes. E-beam lithography is carried out at an exposure dose of 120 μC/cm$^2$. This step is ended up with developing the samples in Micrsoresist Ma-D 525 for 150 seconds, rinsing in DI water for 5 minutes and drying with $N_2$.[11]

**Ion milling** — Argon ion milling was used to pattern NiMnSb into bar and cross-bar shapes. The argon ions were accelerated at 300 V while the beam voltage and current were kept at 600 V and 28 mA respectively.[12] To avoid over-heating of the sample surface, the milling was carried out by alternating milling time of 20 seconds to cooling time of 20 seconds. The InP:S/(In,Ga)As/NiMnSb sample was milled for 10 minutes in total, resulting in a depth of ~1 μm, as measured by the scanning electron microscope (SEM). The process

[11] The spinning of the resist, the e-beam lithography and the developing were done by T. Mitchell in the Semiconductor Physics research group.

[12] Ion milling for NiMnSb samples was carried out by R. Mansell in Thin Film Magnetism research group using a different argon ion miller from the one used for YIG/HM samples.

ended up with immersing the sample in acetone for at least 7 hours for to remove the residual Ma-N resist. Figure 3.3 shows the SEM images of a 4×40 $\mu m^2$ bar (the area near the pad) and a 5×250 $\mu m^2$ cross-bar (the central region), showing good patterning quality. The Cr/Au contact pads were not grown on the NiMnSb samples, as direct bonding was possible in this case.

## 3.3 Experimental setup

### 3.3.1 Electromagnet and sample mounting

The experiments described in this thesis were carried out using a GMW5403 electromagnet with Helmholtz configuration (Figure 3.4 (a)). The gap between the two poles is adjustable from 30 mm to 60 mm, with a pole face area of 11.3 $cm^2$. Up to 40-ampere DC current can be applied to the Helmholtz coil, and about 1 T magnetic field can be generated for maximum. The magnetic field between two poles can be treated as nearly uniform. A calibration between the applied current and the generated magnetic field has been carried out previously, yielding an overall error of 2.6% in the calculation of magnetic field [173]. Finally, two twisted wires in green and yellow colour can be optionally used for 4-four-port probing. The measurement of YIG/HM bilayers and NiMnSb samples shared the same setup as introduced below.

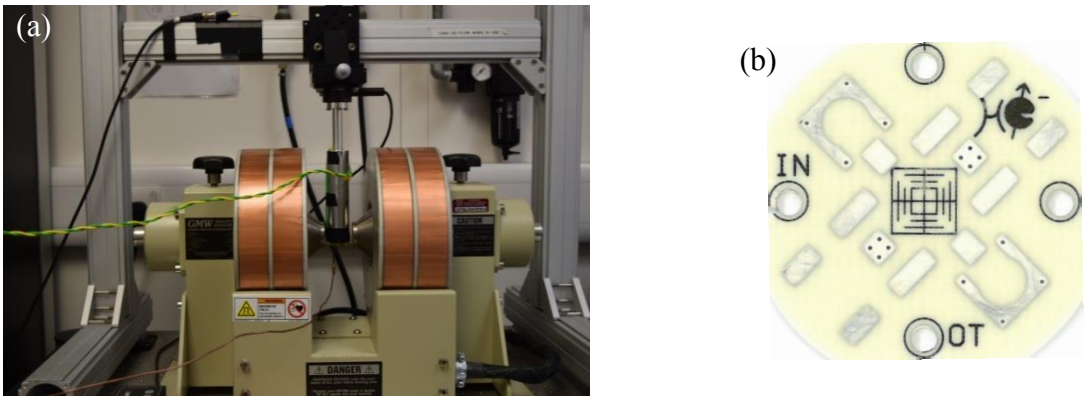


**Figure 3.4** (a) The electromagnet setup and (b) the layout of the PCB.

Samples were first glued onto a self-designed printed circuit board (PCB) shown in Figure 3.4 (b) using CMR-Direct GE Vanish. The patterned bar on the sample was then connected to the microstrip waveguide on the PCB via wedge bonding using 35-μm aluminium wire, and was terminated at a SMP connector. The PCB was then mounted onto an aluminium sample holder rod that fitted between the poles of the electromagnet. The sample holder was fixed to a frame with two translation stages and a rotation stage, allowing horizontal, vertical and 360° rotational adjustments. We were able to perform both in-plane and out-of-plane rotation in magnetic field by choosing different sample holders. The sample holder was connected to the external instruments both via a semi-rigid RF coaxial cable and DC lines.

### 3.3.2 Electrical detection of current-induced ferromagnetic resonance

Unlike the conventional FMR driven by the external microwave magnetic field generated by a waveguide or in a cavity, magnetization dynamics in CI-FMR is driven by an "effective magnetic field" generated when a microwave charge current is passed in the sample bars. The nature of this "effective magnetic field" can be different depending on the material of the bars and the device layout, and this has been discussed in greater details in section 2.4. In general, CI-FMR provides an effective method to both characterise ferromagnetic samples at the nanometre-scale and quantify the current-induced torques [11].

One common method to detect CI-FMR is to measure a longitudinal DC voltage near the resonance condition. Figure 3.5 shows the schematic diagram of the setup. An external magnetic field is applied to the sample bar via the electromagnet to align the magnetization. An Anritsu MG3694C signal generator is used to supply the microwave current to the sample. The use of an Anritsu K250 bias tee allows us to measure the DC voltage along the bar simultaneously. The microwave current is pulse-modulated to allow the lock-in detection to improve the signal-to-noise ratio. The modulated DC voltage along the bar is detected by a Stanford SR830 lock-in amplifier through a Stanford SR560 pre-amplifier.

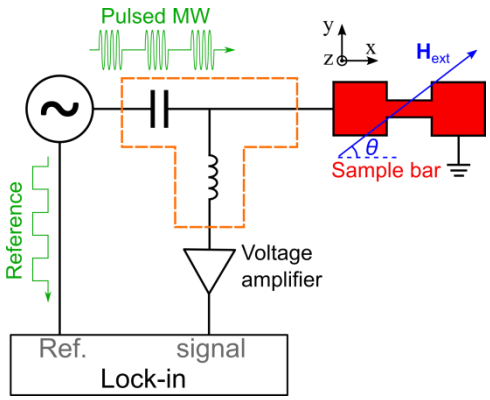


**Figure 3.5** Schematic diagram for CI-FMR measurement. The circuit inside the dashed-line frame in orange is the bias-T.

**Spin rectification** — One mechanism behind the generation of the longitudinal DC voltage at resonance is spin rectification, which exploits the anisotropic magnetoresistance (AMR) or spin Hall magnetoresistance (SMR) effect in the magnetic samples. Assume that the driving microwave current is $I_{MW} = I_0\cos(\omega t)$. From Ohm's law, the voltage along the bar is:

$$V(t) = I_0 \cos(\omega t) R(t) \tag{3.1}$$

At resonance, the oscillating magnetization leads to a time-dependent AMR or SMR at the same frequency:

$$R(t) = R_{\parallel} + \Delta R \cos^2\left[\theta + \theta_c \cos(\omega t)\right] \tag{3.2}$$

where $\theta_c$ is the precession cone angle. Under the small-angle approximation ($\theta_c << 1$), we can expand Eq. (3.2) using Taylor's series to the first order in $\theta_c$ and substitute it into Eq. (3.1):

$$V(t) \approx I_0 \cos(\omega t)\left[R_{\parallel} + \Delta R \cos^2\theta - \Delta R \theta_c \sin(2\theta)\cos(\omega t)\right] \tag{3.3}$$

By using the relation $\cos^2(\omega t) = ½[1+\cos(2\omega t)]$, we can see that $V(t)$ contains a time-independent term:

$$V_{SR} = -\frac{1}{2} I_0 \Delta R \theta_c \sin(2\theta) \tag{3.4}$$

which is what we measure. By measuring the angle dependence of the DC rectified signal at resonance, we can determine the precession cone angle, from which the current-induced effective field $\mathbf{h}_{\text{eff}} = (h_x, h_y, h_z)e^{j\omega t}$ that is responsible for driving this precession can be calculated. By solving the LLG equation (see Appendix A), we find that the rectified voltage near resonance consists of two Lorentzian components of symmetric ($V_{\text{sym-SR}}$) and antisymmetric lineshapes ($V_{\text{asy-SR}}$) [11,12]:

$$V_{SR} = V_{sym-SR} \frac{\Delta H^2}{(H_{ext} - H_{res})^2 + \Delta H^2} + V_{asy-SR} \frac{(H_{ext} - H_{res})\Delta H}{(H_{ext} - H_{res})^2 + \Delta H^2} \tag{3.5}$$

where

$$V_{sym-SR} = \frac{I_0 \Delta R}{2} \frac{\omega}{\mu_0 \gamma \Delta H (2H_{res} + H_1 + H_2)} h_z \sin 2\theta = \frac{I_0 \Delta R}{2} A_{sym} h_z \sin 2\theta \tag{3.6}$$

$$V_{asy-SR} = \frac{I_0 \Delta R}{2} \frac{(H_{res} + H_1)}{\Delta H (2H_{res} + H_1 + H_2)} (-h_x \sin\theta + h_y \cos\theta) \sin 2\theta = \frac{I_0 \Delta R}{2} A_{asy} (-h_x \sin\theta + h_y \cos\theta) \tag{3.7}$$

The terms $H_1$ and $H_2$ are coefficients that include the magnetic anisotropy of the sample and their complete expression is given in Appendix A. Both $H_1$ and $H_2$ are a function of the angle between the magnetization and the [100] crystalline orientation. Therefore, once knowing the AMR coefficient and the magnetic anisotropy, we can determine each component of $\mathbf{h}_{\text{eff}}$ by decomposing the resonance lineshape into $V_{\text{sym-SR}}$ and $V_{\text{asy-SR}}$, and measuring their dependence on the angle $\theta$.

It should be noted that the expression for $V_{\text{SR}}$ is directly deduced from the LLG equation for a generic driving field $\mathbf{h}_{\text{eff}}$ and does not depend on the nature of this field. Therefore, the equations above are applicable to both NiMnSb and the YIG/HM samples.

**Spin pumping** — For completeness, we should mention here that in the YIG/HM bilayer samples, there could be another contribution to the DC longitudinal voltage at resonance, spin

pumping [174,175]. The spin pumping signal should have a purely symmetric Lorentzian lineshape, since it is independent on the phase between the charge current and the magnetization precession. According to [106], the DC voltage generated via this mechanism is given by

$$V_{sym\text{-}SP} = R_0 w_{HM} \frac{2e}{\hbar} \vartheta_{SH} \lambda_{HM} \eta \tanh\left(\frac{t_{HM}}{2\lambda_{HM}}\right) j_s^0 \sin\theta \tag{3.8}$$

Here, $w_{HM}$, $t_{HM}$, $\vartheta_{SH}$ and $\lambda_{HM}$ are the width, thickness, spin Hall angle and spin diffusion length of the HM respectively; $e$ is the elementary charge and $\hbar$ is the reduced Planck constant; $\eta$ is a correction factor for the ellipticity of the magnetization precession. The spin-current density $j_s^0$ at the interface is given by [36]:

$$j_s^0 = \frac{\hbar g_{eff}^{\uparrow\downarrow} \gamma_{eff}^2 \left(\mu_0 h_{eff}\right)^2 \left[\mu_0 M_{eff}\gamma_{eff} + \sqrt{\left(\mu_0 M_{eff}\gamma_{eff}\right)^2 + 16\left(\pi f\right)^2}\right]}{8\pi\alpha_{eff}^2 \left[\left(\mu_0 M_{eff}\gamma_{eff}\right)^2 + 16\left(\pi f\right)^2\right]} \tag{3.9}$$

where $g_{eff}^{\uparrow\downarrow}$, $h_{eff}$, $\gamma_{eff}$ and $M_{eff}$ are the effective values of spin mixing conductance, current-induced field, gyromagnetic ratio and magnetization respectively. This spin-pumping induced symmetric signal $V_{sym\text{-}SP}$ must be considered in conjunction with $V_{sym\text{-}SR}$ induced by rectification in the YIG/HM samples, complicating the analysis. In Chapter 4, we will show how these two terms can be separated by performing a thickness dependent study.

### 3.3.3 Damping control via direct current bias

In the case of STT or SOT, the out-of-plane component of the current-induced effective field can have a format of $\mathbf{h}_{eff} \propto \mathbf{M} \times \boldsymbol{\sigma}$, where $\boldsymbol{\sigma}$ is unit vector of the spin polarization, which is associated to an anti-damping torque. In section 5.2.2, we use an alternative method to measure this term, which consists in measuring the changes in Gilbert damping factor induced when a DC electric current is passed in the bars in conjunction with the microwave one [47,92]. The Gilbert damping factor is extracted from the frequency dependence of the linewidth.

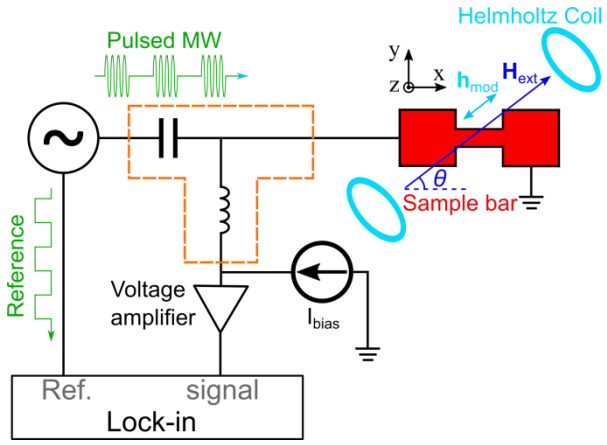


**Figure 3.6** Schematic diagram for damping-controlled CI-FMR measurement.

The circuit diagram for this measurement is shown in Figure 3.6. Compared with the standard CI-FMR measurement setup (Figure 3.5), an additional K2400 source meter is introduced as a DC current source. CI-FMR measurement is then carried out under different DC bias currents and the linewidth of the FMR signal by applying the bias current is determined by fitting the lineshape of the DC resonance voltage.

The CI-FMR detection method is subject to the bolometric effect [176,177]. Since the microwave current is modulated at lock-in frequency, the sample resistance is expected to oscillate by a certain amount (noted as $\Delta R_{MW}$) at the same frequency due to Joule heating. A DC bias current $I_{bias}$ can then introduce an oscillating voltage proportional to $I_{bias}\Delta R_{MW}$ along the sample bar, which appears as an additional background voltage in our lock-in detected signal. This background could be orders of magnitude larger than our resonance signal, decreasing the sensitivity of the measurement

In order to minimize the bolometric effect, field modulation rather than current modulation technique is employed. A couple of Helmholtz coils are introduced between the magnetic poles of the electromagnet to provide a small oscillating magnetic field along the original external field. A sinusoidal voltage $V_{mod}\sin(\omega t)$ at the lock-in frequency is applied to

the coils using a function generator, and the magnitude of the generated field is measured to be (110 ± 5) × $V_{mod}\sin(\omega t)$ in μT using a Gauss meter, where $V_{mod}$ is in the unit of Volt.

Under magnetic-field modulation, the DC voltage along the bar becomes [126]:

$$V_{SR-fm} = h_{mod}\frac{dV_{SR}}{dH_{ext}} \tag{3.10}$$

where $h_{mod}$ is the peak value of the sinusoidal modulation field, and $V_{SR}$ is the spin rectified voltage defined in Eq. (3.5). Substituting Eq. (3.5) into (3.10), we can get the expression of $V_{SR\text{-}fm}$ as:

$$V_{SR-fm} = \frac{h_{mod}}{\Delta H}\left\{2V_{sym-SR}S(H)A(H) + V_{asy-SR}\left[A^2(H) - S^2(H)\right]\right\} \tag{3.11}$$

where $V_{sym\text{-}SR}$ and $V_{asy\text{-}SR}$ are defined in Eq. (3.6) and (3.7) respectively, and

$$S(H) = \frac{\Delta H^2}{(H_{ext} - H_{res})^2 + \Delta H^2} \tag{3.12}$$

$$A(H) = \frac{(H_{ext} - H_{res})\Delta H}{(H_{ext} - H_{res})^2 + \Delta H^2} \tag{3.13}$$

Therefore, when field modulation is applied, the resonance signal has a more complicated lineshape than in the case of current modulation. Despite this, we can still get the resonance linewidth by fitting the lineshape with the above equations. This allows us to estimate the effective field component that give rise to the torque [47].

### 3.3.4 Microwave current calibration

The resistance of our sample is ~100 Ω for the 4×40 μm$^2$ NiMnSb bars and ~850 Ω (~7000 Ω) for the 5×50 μm$^2$ YIG/Pt (YIG/Ta) bars, which makes a high impedance mismatch arise with the rest of the 50 Ω microwave circuits. In order to measure exactly the current density that flows in our bars, we carry a calibration procedure based on the temperature

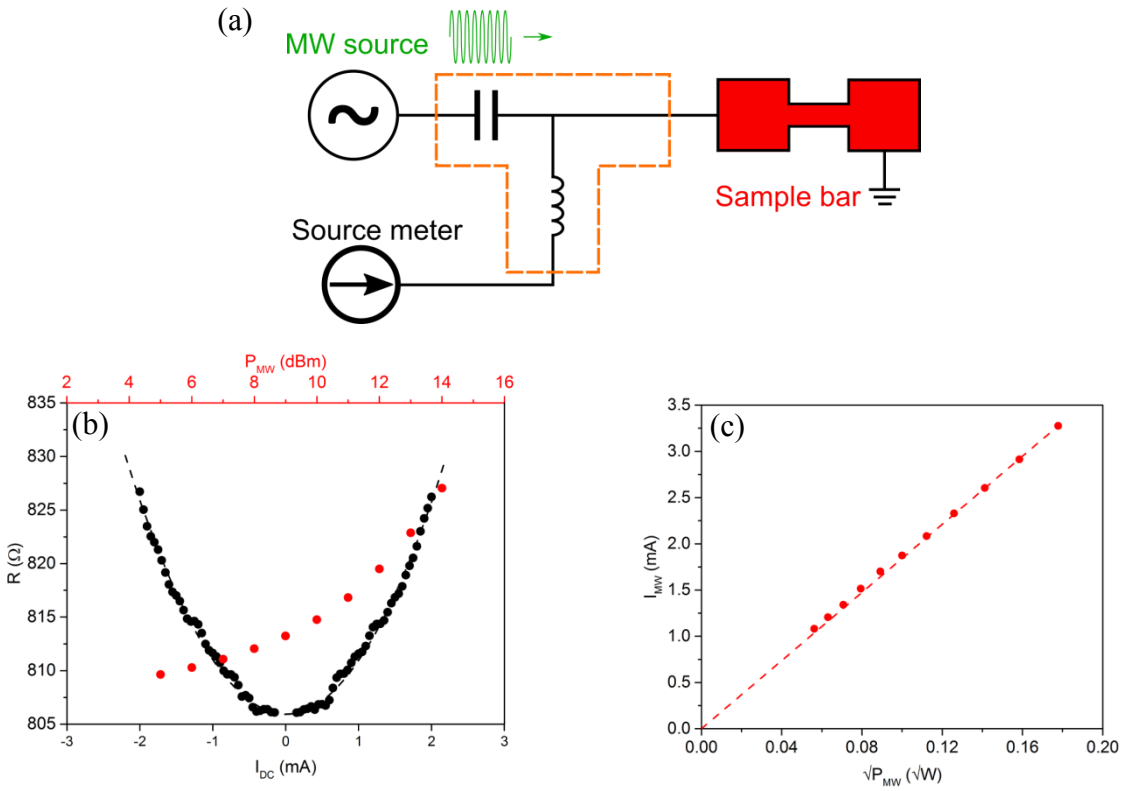


**Figure 3.7** (a) Schematic diagram of the microwave current calibration setup. (b) Comparison of the bar resistance when a DC current (black) and a microwave current (red) are applied. (c) Joule heating calibration shows a linear relationship between the square root of the applied microwave power and the microwave current. (b) and (c) are examples taken from a 5-um wide YIG(14.8)/Pt(4.2) bar.

dependence of the bar resistance. The procedure consists in comparing the Joule heating created by a DC current and the incident microwave signal by measuring the sample resistance as shown in Figure 3.7 (a). First, the microwave source is turned off, and the K2400 source meter sweeps the DC current from negative to positive values while the resistance is being measured (Figure 3.7 (b), in black). Then, we gradually increase the input microwave power and measure the resistance changes (Figure 3.7 (b), in red). The modulation function of the microwave source is turned off here. Since the powers produced by a DC current $I_{DC}$ and a microwave current $I_{MW}e^{j\omega t}$ are $I_{DC}^2R$ and $I_{MW}^2R/2$ respectively, the value of $I_{MW}$ can be determined by multiplying the DC current corresponding to the same

resistance by a factor of $\sqrt{2}$. Figure 3.7 (c) shows the final calibration where $I_{MW}$ is plotted against the square root of the microwave power, showing a linear dependence.

# Chapter 4 Current-induced resonance in $Y_3Fe_5O_{12}$/heavy metal bilayers

Within the family of magnetic materials, YIG always holds a special place in ferromagnetic materials, owing to its ultra-low damping, high Curie temperature and chemical stability [178–180]. As an insulating material, YIG allows pure spin currents flow inside without associated charge transport. This minimizes Joule heating and electromigration effects, because there is no charge current flowing in YIG. Meanwhile, this also offers an unprecedented geometric flexibility. Since the information in YIG is transmitted in a form of collective motion of magnetic momentum (i.e. spin wave), this allows us to build new devices based on the concept of wave, i.e. Mach-Zehnder interferometers [181,182], resonators [183,184], microwave oscillators [91] and so on.

A heavy metal (HM) layer, such as Pt, Ta or W, can be grown on YIG as a spin current source, as heavy metals can convert a charge current into a transverse pure spin current (i.e, a flow of spin angular momentum) via the spin Hall effect (SHE). The angular momentum transferred into YIG can exert spin-transfer torque (STT) on the magnetization, enabling the implementation of spin torque devices. Recently, several groups have made some progress on this issue, including damping control by passing a DC current in the Pt capping layer [185], by which spin Hall auto-oscillation are realized [91,92]. Replacing the DC current with a microwave current, the electrical signal in Pt can also be transmitted via spin waves in YIG [180].

To further explore the applications, a critical point is understanding of the torques in YIG induced by the charge current flowing in the adjacent heavy metal[13]. For this purpose, we use

[13] Part of this chapter is published on: Z. Fang et al., *Appl. Phys. Lett.* **110**, 092403 (2017).

current-induced ferromagnetic resonance (CI-FMR) to study a series of YIG/HM samples with different YIG thickness. We start with a theoretical analysis of the lineshape symmetry of the resonance signals and their dependence on the characteristics of the samples. Then we show the results of spin Hall magnetoresistance (SMR) and FMR measurements for each sample. Finally, we estimate the effective field induced by the current in the HM based on a YIG-thickness dependence study of the FMR.

## 4.1 Lineshape symmetry analysis

Figure 4.1 shows a schematic diagram of the CI-FMR measurement in YIG/heavy metal system. The leftmost microwave source generates an oscillating charge current into the Pt (or Ta) layer, which is converted into perpendicular pure spin-current oscillating at the same frequency via SHE. This oscillating spin current flows into the ferromagnetic layer and exert an oscillating STT to YIG. Moreover, according to Ampere's law, the charge current in Pt also generate an Oersted field, inserting a torque to YIG as well. Both mechanisms can drive magnetization precession once FMR condition is satisfied.

As discussed in section 3.3.2, the lineshape and the symmetry of the resonance signal depend on both the driving torque (or effective field) and the generation of the DC voltage (i.e. spin rectification or spin pumping). Here, the current-induced torque in YIG/Pt consists a

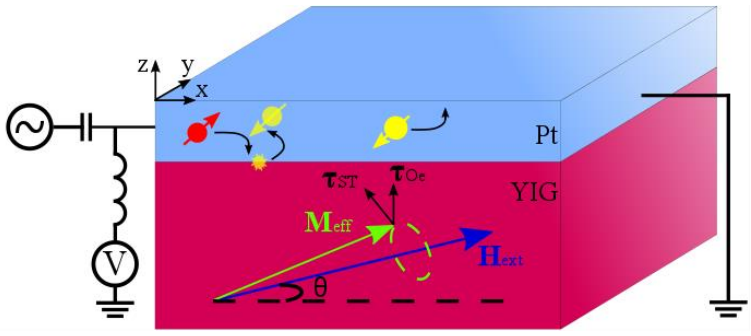


**Figure 4.1** Schematic diagram for CI-FMR measurement setup for YIG/HM. Magnetic dynamics are driven by the torques induced by both STT and Oersted field.

field-like torque $\boldsymbol{\tau}_{Oe} = \mathbf{M} \times \mathbf{h}_{Oe}$ induced by the Oersted field $\mathbf{h}_{Oe}$ // $\mathbf{y}$, where $\mathbf{y}$ is the unit vector along the y axis, and an antidamping-like STT $\boldsymbol{\tau}_{ST} = \mathbf{M} \times \mathbf{h}_{ST}$ induced by an effective field $\mathbf{h}_{ST}$ // $\mathbf{y} \times \mathbf{M}$. If $\mathbf{M}$ is in the x-y plane, both torques reach their maximum when $\mathbf{M}$ is along the x-axis, and become zero when $\mathbf{M}$ is in y-axis. Although the STT could introduce a field-like component which is indistinguishable from Oersted field from the symmetry point of view [139], in our work, we confirm that the driving field is dominated by the Oersted contribution by repeating the measurement with Pt and Ta [186].

**Table 4.1** Summary of resonance DC signal components from spin rectification (SR) and spin pumping (SP), with their Lorentzian lineshape, and dependence on $\theta$, $\vartheta_{SH}$, $t_{YIG}$ and $\alpha_{eff}$. $C_i$ are the positive coefficients independent from the parameters listed above.

| Driving | Detecting | lineshape | Dependence on $\theta$, $\vartheta_{SH}$, $t_{YIG}$, and $\alpha_{eff}$ |
|---|---|---|---|
| $\mathbf{h}_{ST}$ | SR | Symmetric | $-C_{ST\text{-}SR}\left[\vartheta_{SH}^3/(\alpha_{eff}t_{YIG})\right]\sin 2\theta\cos\theta$ |
| | SP | Symmetric | $C_{ST\text{-}SP}\left[\vartheta_{SH}^3/(\alpha_{eff}t_{YIG})^2\right]\sin 2\theta\cos\theta$ |
| $\mathbf{h}_{Oe}$ | SR | Anti-symmetric | $-C_{Oe\text{-}SR}\left(\vartheta_{SH}^2/\alpha_{eff}\right)\sin 2\theta\cos\theta$ |
| | SP | Symmetric | $C_{Oe\text{-}SP}\left(\vartheta_{SH}/\alpha_{eff}^2\right)\sin 2\theta\cos\theta$ |

From Eq. (3.5)-(3.7), we know that the DC voltage induced by spin rectification consists of two components: a symmetric Lorentzian component $V_{sym\text{-}SR}$ is induced by an antidamping-like field $\mathbf{h}_{ST}$ in z-axis and an antisymmetric Lorentzian $V_{asy\text{-}SR}$ is induced by $\mathbf{h}_{Oe}$ in y-axis. In contrast, the voltage induced by spin pumping, irrespective of the driving mechanisms, can be described by a symmetric Lorentzian component $V_{sym\text{-}SP}$ alone. The reason is that, unlike the spin rectification mechanism, it is independent from the phase between the microwave current and the precessing magnetization. This is because the DC component in spin pumping voltage only depends on the magnetization precessional area at resonance [187], and it does not result from the product of two variables as spin rectification

(from the product of two cosine terms from microwave current and AMR). We summarize[14] the lineshape and dependence of these DC signals in Table 4.1. Here, $\vartheta_{SH}$ is the spin Hall angle of Pt (or Ta); $t_{YIG}$ is the thickness of YIG layer; $\theta$ is the angle between the in-plane external field and the sample bar. The effective damping factor $\alpha_{eff}$ is a function of $t_{YIG}$ and includes the spin pumping term $\alpha_{SP}$ [106]:

$$\alpha_{eff}\left(t_{YIG}\right)=\alpha_0+\alpha_{SP}=\alpha_0+\frac{g\mu_B}{4\pi M_s t_{YIG}}g_{eff}^{\uparrow\downarrow} \tag{4.1}$$

$M_s$ and $\alpha_0$ are the saturation magnetization and the intrinsic Gilbert damping coefficient of YIG without HM cap respectively; $g$ is the g-factor; $\mu_B$ is the Bohr magneton; $g_{eff}^{\uparrow\downarrow}$ is the interface effective spin mixing conductance taking into account the backflow. Assuming that $\alpha_0$ does not change with $t_{YIG}$, $g_{eff}^{\uparrow\downarrow}$ can be determined by measuring $\alpha_{eff}$ for samples of different YIG thickness. Therefore, though the four components in Table 4.1 share the same angle dependence, we can investigate the current-induced effective field by varying the thickness of YIG.

## 4.2 Spin Hall magnetoresistance measurements

We first present the results from SMR measurement, since it is an essential quantity for the calculation of current-induced effective field in FMR measurement (Eq. (3.6)-(3.7)). Besides, it also helps us calibrate the angle $\theta$ and, more importantly, identify the mechanisms behind the anisotropy in resistance. In addition to SMR, magnetic proximity effect (MPE) can induce the AMR which has the same in-plane symmetry as SMR. Several atomic layers of Pt near the interface could become ferromagnetic due to MPE [188] and they may also show the FMR phenomenon once the resonance condition is satisfied. This may contaminate our FMR signal due to the magnetization precession in YIG.

[14] The deduction of Table 4.1 is shown in Appendix B.

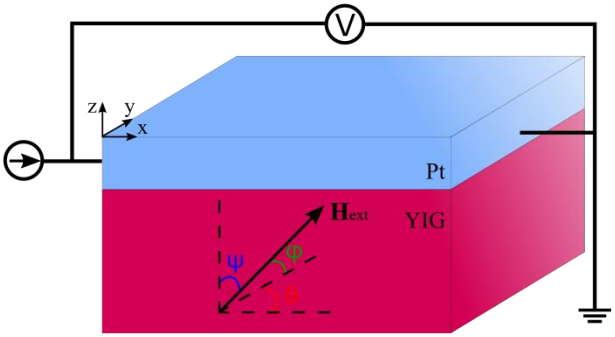


**Figure 4.2** Experimental setup for magnetoresistance measurement.

The SMR measurement is carried out with an external magnetic field $\mathbf{H}_{ext}$ ~ 0.8 T, which is large enough to keeping saturate the magnetization. $\mathbf{H}_{ext}$ is rotatable either in x-y, y-z and x-z plane as defined in Figure 4.2. The source meter K2400 is used to apply DC current into the sample bar and to measure the bar voltage simultaneously. Referring to section 2.2.1 and 2.2.3, the anisotropy in resistance from SMR and MPE-induced anisotropic magnetoresistance (AMR) can be identified by their angle dependence when $\mathbf{H}_{ext}$ goes out of the film plane [52]: the former depends on the angle between the SHE-induced spin polarization in y-axis at the interface and the magnetization in YIG, so the resistance should be a constant when $\mathbf{H}_{ext}$ rotates in x-z plane; the later instead depends on the angle between the charge current and the magnetization in YIG, so the resistance should stay unchanged if $\mathbf{H}_{ext}$ rotates in y-z plane. Figure 4.3 shows the measurement from each sample, where the number in bracket is the layer thickness in nanometre. Figure 4.3 (a) gives an example of SMR measurement from a YIG(14.8)/Pt bar, which shows anisotropy in resistance when $\mathbf{H}_{ext}$ is applied in x-y plane or y-z plane, while no clear anisotropy is measured in x-z plane. This means that the MPE-induced AMR is negligible in our YIG/Pt samples at room temperature. The in-plane SMR measurement of other bars are presented in Figure 4.3 (b) – (f). In addition, no clear SMR was observed in the two thinnest samples, i.e. YIG(8.2)/Pt and YIG(8.4)/Ta, as shown in Figure 4.4.

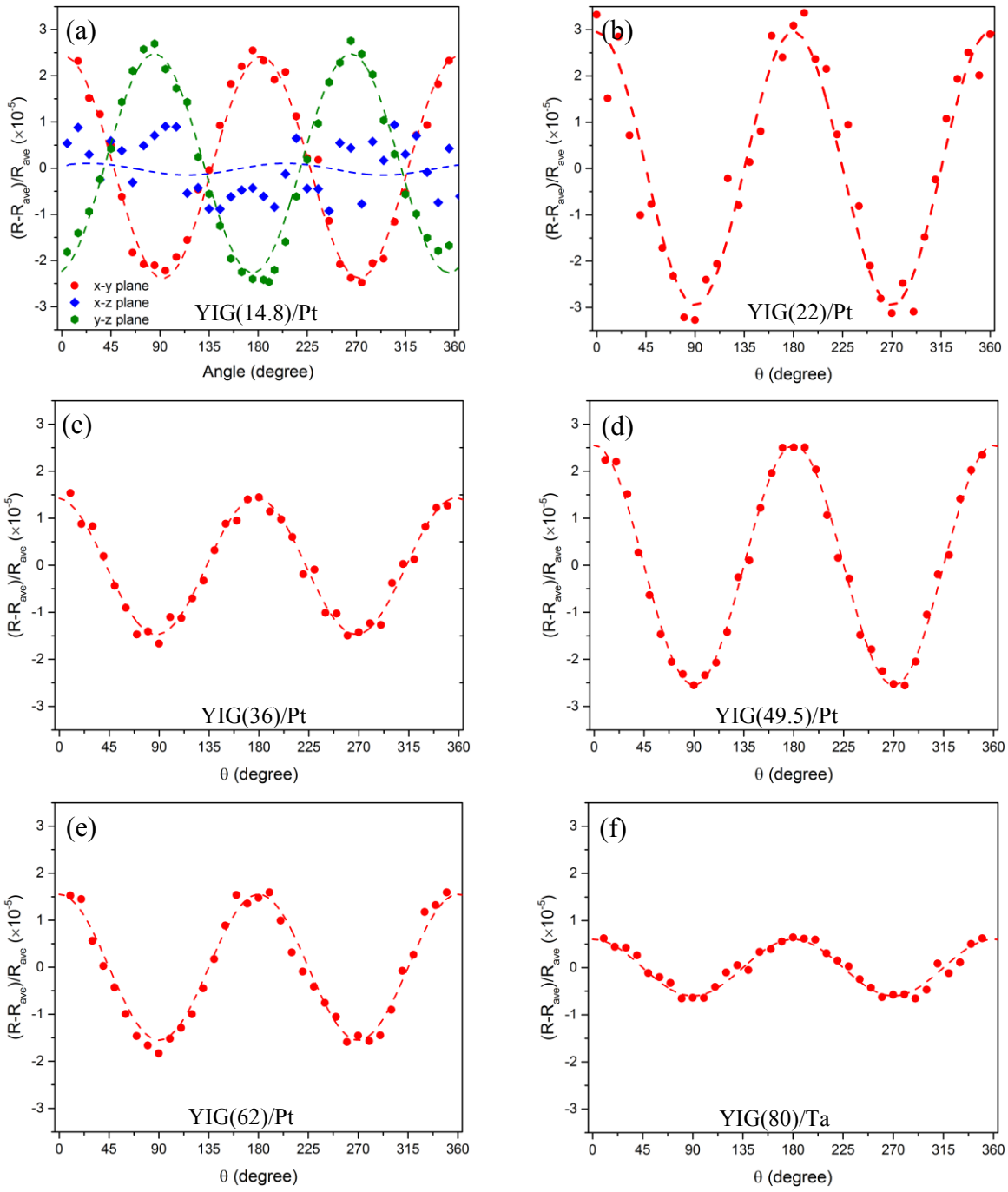


**Figure 4.3** (a) Angle-dependent magnetoresistance measurement in three principal planes on a YIG(14.8)/Pt(4.2) sample, where $R_{ave}$ is the resistance in average. The dashed lines are the fitting results. (b-f) The in-plane magnetoresistance measurement of other five bars with different YIG thickness. The thickness of Pt and Ta is 4.2 nm and 5.0 nm respectively.

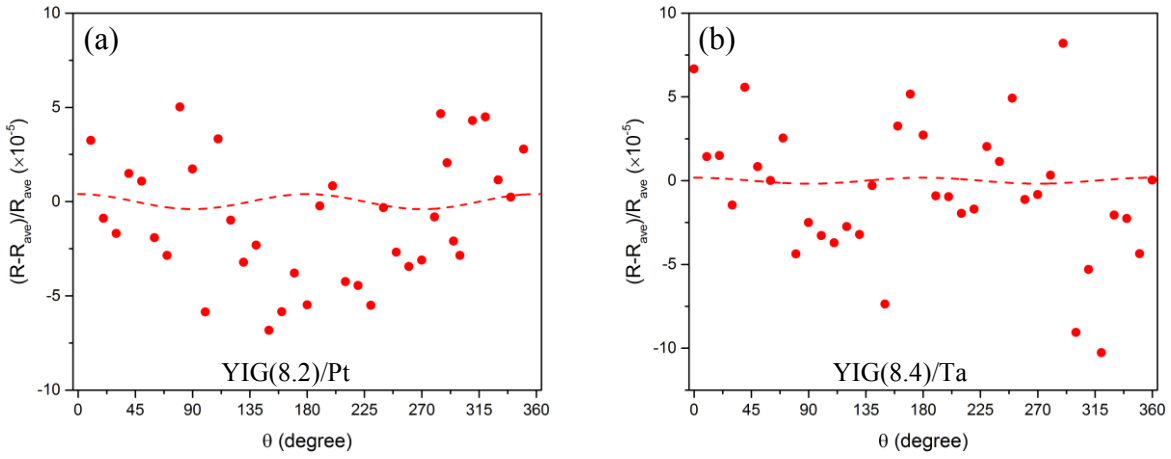


**Figure 4.4** In-plane magnetoresistance measurement of the two thinnest sample: (a) YIG(8.2)/Pt and (b) YIG(8.4)/Ta.

Similar results have been reported in YIG/Pt at room temperature by other groups [50,52,189,190], while the mechanism behind still remains controversial and not fully understood. Although the magnetoresistance in YIG/Pt can be well explained by a simultaneous action of SHE and inversed spin Hall effect (ISHE) (i.e. SMR), there are other theory on magnetoresistance which results in the similar behaviour. For example, Lu et al. proposed a new "hybrid magnetoresistance" in Pt in contact with a ferromagnetic materials originating from MPE [189]. This new magnetoresistance has the behaviour of $\rho_y < \rho_z \approx \rho_x$ which is the same as that of SMR. Miao et al. then argued that both the SMR and this new magnetoresistance from MPE contribute to the magnetoresistance of YIG/Pt, and they can be separated by tuning the YIG surface or inserting an Au layer in the middle [191]. Besides, Grigoryan et al. theoretically predicted an intrinsic magnetoresistance in YIG/Pt induced by the Rashba spin-orbit coupling [192]. When the external field is not collinear with the spin polarization introduced by the Rashba effect, the Hanle effect[15] will lead a spin precession and a dephasing of spin accumulation, resulting changes in resistivity [193,194]. This leaves a question that the SMR observed in [52] is a bulk metal or interface effect. Recently, this type of magnetoresistance has been observed in metallic heterostructures [195,196] and it has

[15] In Spintronics, Hanle effect is the phenomenon that an applied transverse magnetic field can result in a precession of the spin accumulation around this field [224]. This is important because it provides a method to manipulate the spins in FMs without rotating its magnetization.

the same symmetry as SMR. Therefore, the origins of magnetoresistance in YIG/Pt are rich and still remain controversial. However, since it is out of the scope of this thesis, we stop our discussion here and move on to investigate the FMR experiment results in next section.

## 4.3 Characterisation by ferromagnetic resonance

We first present our results from a 5×50 $\mu m^2$ bar on the YIG(14.8)/Pt(4.2) sample as an example of our frequency-dependent FMR measurement. Figure 4.5 shows the magnetic-field dependence of DC voltage measured along the bar at different microwave frequency. The in-plane external field $\mathbf{H}_{ext}$ is applied to the bar at $\theta = 45°$ as defined in Figure 4.1 and magnetic-field-independent background voltage due to spin Seebeck effect (SSE) is removed. The resonance signal is well described by a symmetric and an antisymmetric Lorentzian component. The details about the lineshape will be discussed later.

Figure 4.6 plots the frequency dependence of resonance field (left) and linewidth (right), which are well fitted by the in-plane Kittel formula Eq. (2.28) and the linear linewidth function Eq. (2.29). From the fitting results, we can get the effective values of gyromagnetic ratio $\gamma_{eff}$, effective magnetizsation $M_{eff}$ and effective Gilbert damping factor $\alpha_{eff}$. The measurement is repeated on all the YIG samples, and the results are summarized in Table 4.2, together with the measured SMR coefficient in the previous section. As shown in Figure 4.7, CI-FMR phenomenon is not observed in the sample YIG(8.2)/Pt(4.2) and YIG(8.4)/Ta(5) either. We believe this can be attributed to the increasing of interface roughness of YIG/HM when YIG thickness decreases to several nanometres. This could reduce the spin mixing conductance at interface, and in turn results in the absence of SMR and CI-FMR[16].

[16] Although, from Figure 4.8 (b), we get a spin mixing conductance with amplitude at moderate level, the measurement did not include these two thinnest samples, so it is possible that the spin mixing conductance of these samples are smaller than thicker samples due to increasing surface roughness.

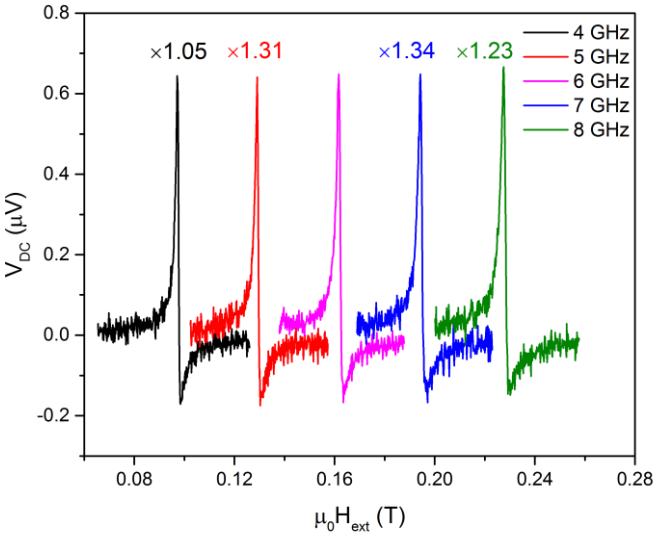


**Figure 4.5** Spectra of current-induced FMR measurement of YIG(14.8)/Pt(4.2) sample at 4-8 GHz, $\theta = 45°$.

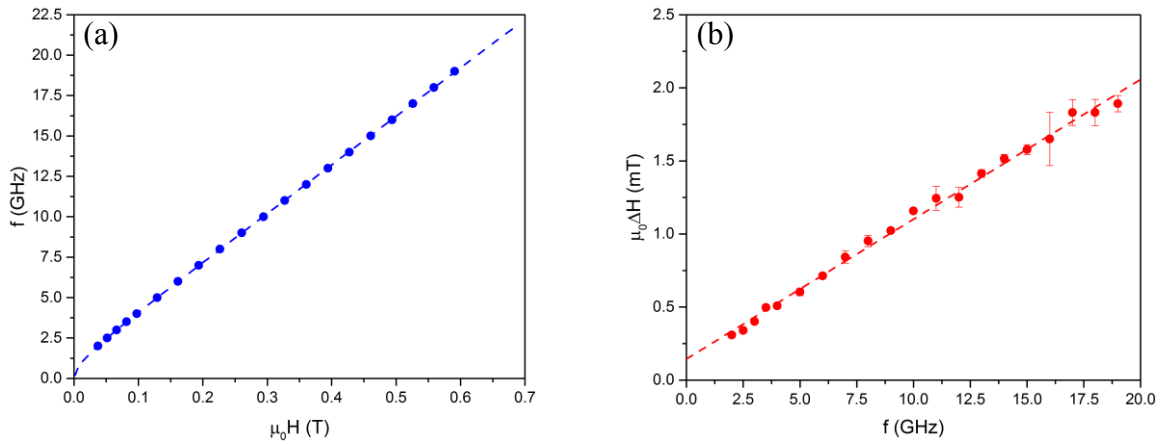


**Figure 4.6** Frequency dependent measurement of the same sample bar as Figure 4.3. (a) Resonance frequency $f$ as a function of the resonance field, fitted with the in-plane Kittel's formula in dashed line. (b) Frequency dependence of the FMR linewidth $\Delta H$. The dashed line represents a linear fit.

**Table 4.2** Summary of sample characteristics. The heavy metal cap layer is Pt unless being specified.

| $t_{YIG}$ (nm) | SMR ($10^{-5}$) | $\gamma_{eff}/2\pi$ (GHz/T) | $M_{eff}$ (kA/m) | $\alpha_{eff}$ ($10^{-3}$) | $K_{2\perp}$ (kJ/m$^3$) |
|---|---|---|---|---|---|
| 14.8 | 4.8 ± 0.6 | 30.0 ± 0.1 | 69.0 ± 3.3 | 1.41 ± 0.02 | 12.6 ± 1.3 |
| 22 | 5.9 ± 1.0 | 29.9 ± 0.1 | 80.8 ± 3.8 | 1.15 ± 0.03 | 11.2 ± 1.1 |
| 36 | 2.9 ± 0.3 | 29.8 ± 0.1 | 82.4 ± 3.0 | 1.00 ± 0.02 | 11.1 ± 1.0 |
| 49.5 | 5.1 ± 0.1 | 29.8 ± 0.1 | 81.8 ± 2.9 | 0.97 ± 0.02 | 11.1 ± 1.0 |
| 62 | 3.1 ± 0.5 | 29.9 ± 0.1 | 76.9 ± 4.4 | 0.93 ± 0.04 | 11.6 ± 1.2 |
| 80 (Ta) | 1.2 ± 0.5 | 28.1 ± 0.9 | 89.5 ± 6.7 | 1.36 ± 0.31 | 10.2 ± 0.9 |

We also measure the magnetic moment of our YIG samples using a vibrating sample magnetometer (VSM)[17] as Figure 4.8(a). The sample chip used for VSM measurement has the area[18] of 4×3 ~ 4×3.5 mm$^2$, and they are taken from the same wafer as the samples used for FMR measurement for each thickness. We can see that there is a 5.1 ± 0.1 nm-thick non-magnetic dead layer in our YIG films. This could be the reason for the absence of SMR nor FMR in YIG(8.2)/Pt(4.2) and YIG(8.4)/Ta(5) samples. Therefore, we define the thickness of active YIG layer as $t_{YIG\text{-}active} = t_{YIG} - 5.1$ in nm, and this value should be used in our calculation. After calibrating the YIG thickness, we can now determine the value of $M_s$ to be 180 ± 20 kA/m from Figure 4.8(a), and the interface anisotropy energy density $K_{2\perp}$ can now be calculated (Table 4.2). In addition, Figure 4.8(b) plots the value of $\alpha_{eff}$ with respect to the value of $t_{YIG\text{-}active}$, which is well fitted by EQ. (4.1). We find the values of $\alpha_0$ and $g_{eff}^{\uparrow\downarrow}$ to be (8.1 ± 0.1) × $10^{-4}$ and (7.1 ± 0.2) × $10^{17}$ m$^{-2}$ respectively, in good agreement with the literature [49].

[17] The VSM measurement was done by M. Ali from University of Leeds.

[18] There is one angle area on the sample chips covered by the tape in the sputtering process in order to fix the samples onto the holder. Therefore, this area is not covered by YIG/HM, leaving a small uncertainty when evaluating the sample area.

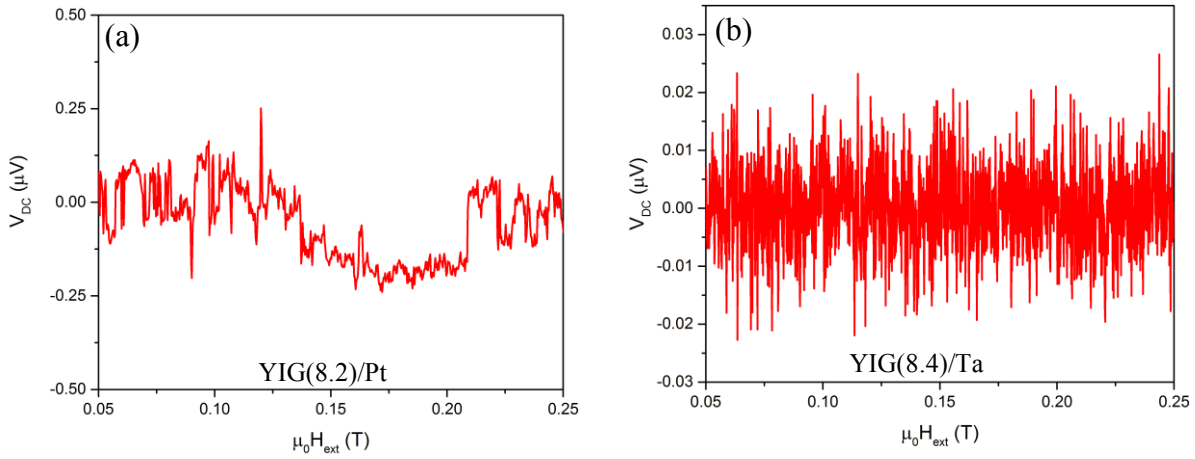


**Figure 4.7** Spectra of current-induced FMR measurement of (a) YIG(8.2)/Pt and (b) YIG(8.4)/Ta at 6 GHz, $\theta = 45°$.

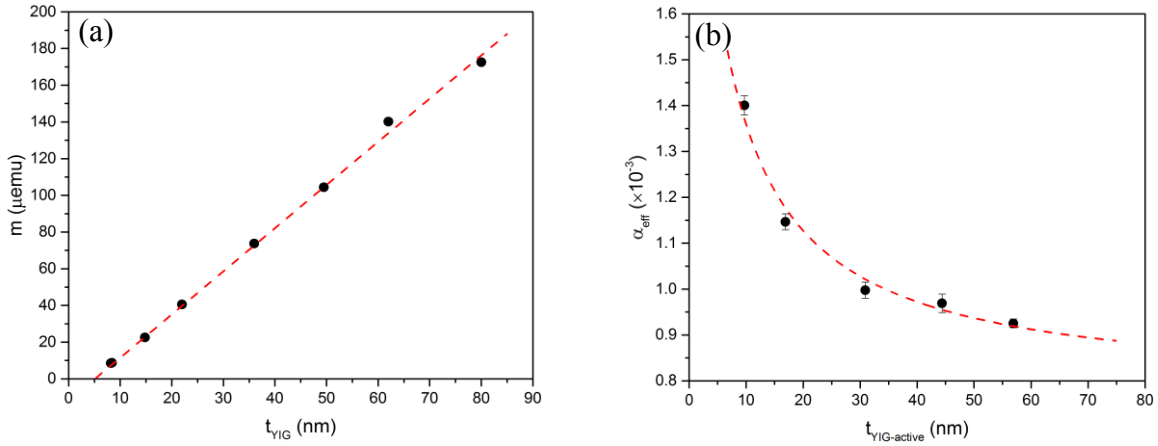


**Figure 4.8** Plot of (a) the magnetic moment m as a function of YIG thickness $t_{YIG}$ and (b) the effective damping $\alpha_{eff}$ as a function of active YIG thickness $t_{YIG\text{-}active}$. Red dashed line represents the fitting result using a linear function and Eq. (4.1) respectively.

The angle-dependent measurement is then carried out for each sample at 8 GHz, and the results are first presented in contour-map form as Figure 4.9. The green and the orange colours approximately represent the positive and negative output voltage at the corresponding angle and field (see the colour bar next to the map), after the constant system noise is subtracted. A resonance is clearly visible at the magnetic field of 0.22 ~ 0.23 T, which can be identified via the big colour contrast between the region of resonance and the ones at higher

and lower field at the same angle. From the figure, we can qualitatively obtain the following information: (1) the in-plane anisotropy is extremely small (< 2.5 mT) for all the samples; (2) the background DC signals shows a –sin(θ) dependence for YIG/Pt while the sign is reversed for YIG/Ta. This results from a combination of the longitudinal SSE and ISHE [54]; (3) the angle dependence of the resonance signal is dominated by a $\sin(2\theta)\cos\theta$ term.

For a quantitative analysis, we decompose the resonance lineshape into $V_{sym}$ and $V_{asy}$ by a Lorentzian fitting using Eq. (3.5), and the results for each sample are presented in Figure 4.10. To be consistent with Table 4.1, we note the spin-rectification induced DC voltage at FMR driven by STT and Oersted field as $V_{ST\text{-}SR}$ and $V_{Oe\text{-}SR}$ respectively, while the spin-pumping induced DC voltage at FMR driven by STT and Oersted field are noted as $V_{ST\text{-}SP}$ and $V_{Oe\text{-}SP}$ respectively. For all the YIG/Pt samples, $V_{sym}$ and $V_{asy}$ have opposite signs. From Table 4.1, this indicates that the spin pumping signal (either $V_{ST\text{-}SP}$ or $V_{Oe\text{-}SP}$) dominates over $V_{ST\text{-}SR}$. The $V_{asy}$ can be fitted well with a $\sin2\theta\cos\theta$ function alone, indicating that the in-plane effective field is mainly along the y-axis (Eq. (3.7)). In contrast, $V_{sym}$ is fitted by the sum of a $\sin2\theta\cos\theta$ term and a $\sin\theta$ term, noted as $V_{sym\text{-}sin2\theta cos\theta}$ and $V_{sym\text{-}sin\theta}$ respectively. The angle dependence of non-resonance background voltage in sample YIG(62.0)/Pt is also inserted in Figure 4.10(e) as an example, which is attributed to the longitudinal SSE [197,198]. The non-resonance voltage shows a $\sin\theta$ dependence, but with opposite sign with respect to the term $V_{sym\text{-}sin\theta}$. We repeat this angle-dependence measurement in each sample with different microwave power. One example from YIG(14.8)/Pt is shown in Figure 4.11, from which we find that all three components in resonance signal are linear in power. This indicates that the small-angle precession approximation is satisfied. The linearity is also held for all the other samples in our CI-FMR measurement.

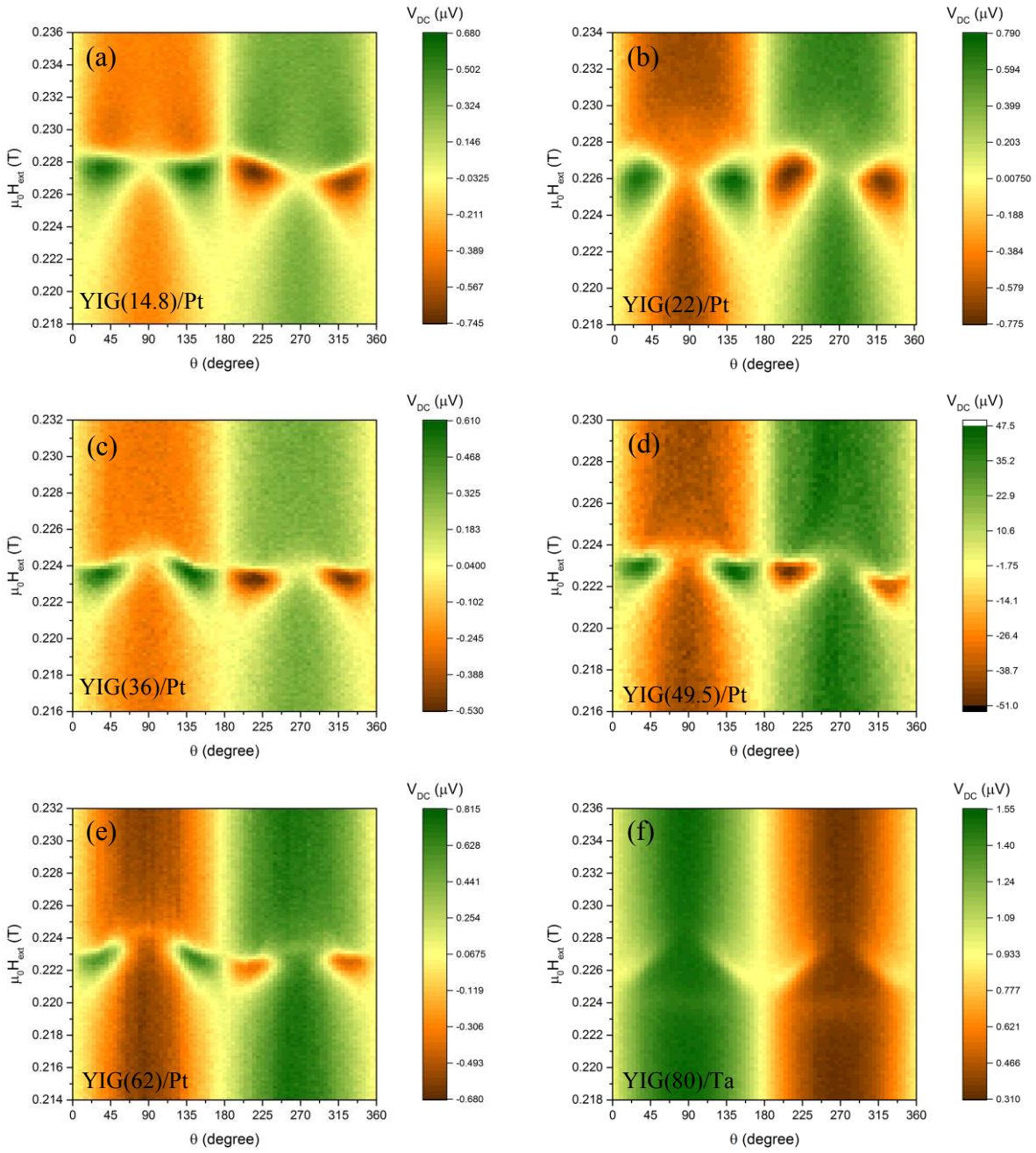


**Figure 4.9** The DC voltage along the bar measured from in-plane rotational scans of the external field, taken from different samples as labelled in figures, all measured at 8 GHz. The thickness of Pt and Ta is 4.2 nm and 5.0 nm respectively. The colour scale represents the magnitude of the DC voltage.

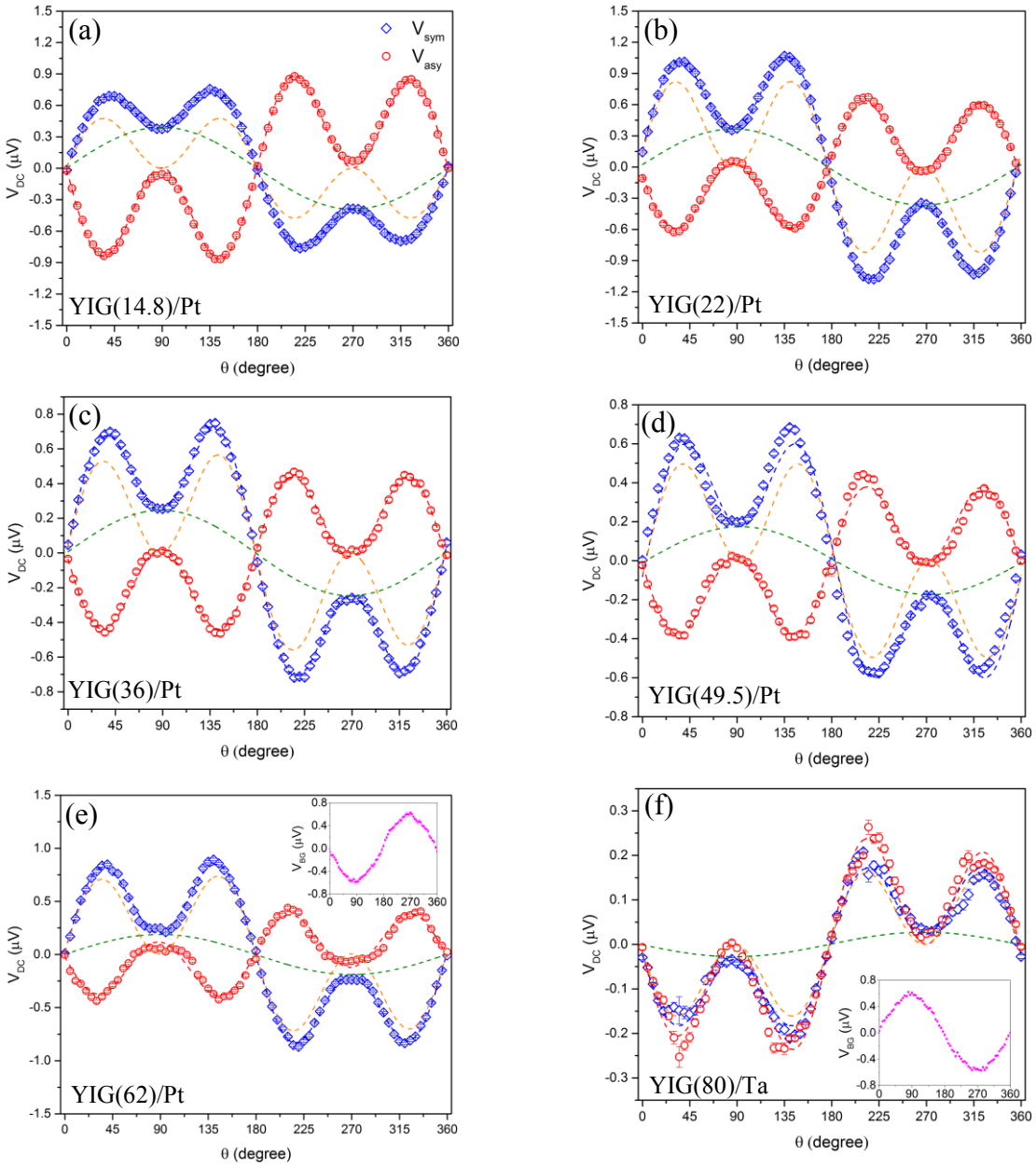


**Figure 4.10** The angle dependence of the amplitude of $V_{sym}$ and $V_{asy}$ components in FMR lineshape, taken from different samples as labelled in figures. The dashed lines represent the fitting. The angle dependence of $V_{asy}$ is fitted by $\sin2\theta\cos\theta$ (red), while the fitting of $V_{sym}$ (blue) requires a combination of a $\sin2\theta\cos\theta$ term (orange) and a $\sin\theta$ term (green). The insets in (e) and (f) are the background signals fitted with a $\sin\theta$ term.

As a control experiment, we replace the Pt with Ta and repeated the angle-dependent measurement in YIG(80)/Ta(5.0) as Figure 4.10(f). The symmetric components, including both $V_{\text{sym-sin2}\theta\cos\theta}$ and $V_{\text{sym-sin}\theta}$, change their sign compared with the YIG/Pt case, while the sign of $V_{\text{asy}}$ stays the same. In addition, the sign of the background voltage is also reversed. These can be understood from the opposite sign of spin Hall angle of Ta compared with Pt. Referring to Table 4.1, once $\vartheta_{\text{SH}}$ is reversed from positive (0.07~0.08 for Pt) to negative (-0.12~-0.15 for Ta) [47,48,51], only $V_{\text{Oe-SR}}$ with an antisymmetric lineshape keeps the same sign, while the sign of all the terms will be reversed, in agreement with what we observe. At this stage, we can initially conclude that $V_{\text{sym}}$ mainly attributes to the spin pumping, while $V_{\text{asy}}$ is from the rectification driven by Oersted field. Furthermore, this result also provides us strong evidence that the Oersted field dominates over the field-like STT in driving magnetization dynamics in our samples [186], because the sign of $V_{\text{asy}}$ does not depend on the sign of the spin Hall angle. In next section, we focus on their dependence on YIG thickness, from which we can understand more about their origins.

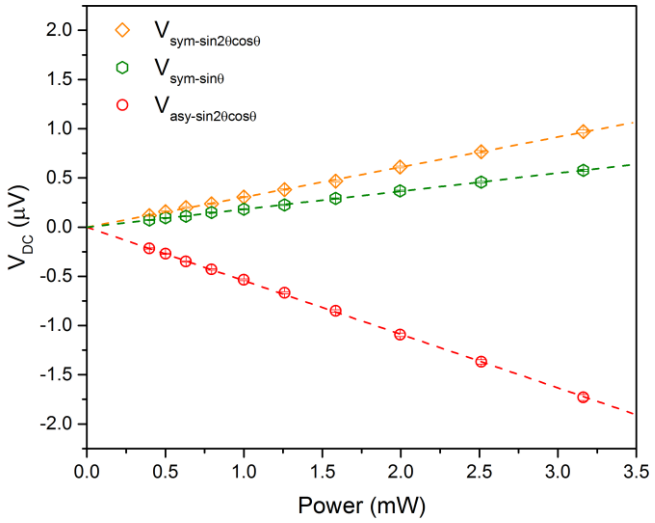


**Figure 4.11** Power dependence of each resonance component at 8 GHz from the YIG(14.8)/Pt sample, obtained by repeating angle-dependence measurement in Figure 4.10(a) with different power.

## 4.4 YIG thickness dependence of resonance signals

We start by analysing the antisymmetric Lorentzian component $V_{asy}$. As already mentioned, this component of the DC voltage is attributed to rectification induced by the field-like torque only. The value of the effective field was obtained by fitting the angle dependence of $V_{asy}$ using Eq. (3.7). The amplitude of the microwave current $I_0$ was deduced from heating calibration measurements [11,15]. Figure 4.12 plots the calculated effective field along the y-axis for each sample, normalized to a unit current density of $j_c = 10^{10}$ A/m$^2$. This can be compared with the value of the Oersted field calculated from Ampere's law as $\mu_0 h_{Oe} = \mu_0 j_c t_{Pt}/2 \approx 26$ μT (red dash in Figure 4.12), where $t_{Pt}$ is the thickness of Pt. The good agreement between the two values further demonstrates that the field-like torque can be mainly attributed to the Oersted field.

The analysis of the symmetric component $V_{sym\text{-}sin2\theta cos\theta}$ is richer, since it contains three contributions as shown in Table 4.1. Moreover, the uncertainty in the evaluation of the spin Hall angle and the spin diffusion length in Pt [51,199] is propagated to the determination of the effective field that generates the antidamping-like torque. Despite this, we are still able to

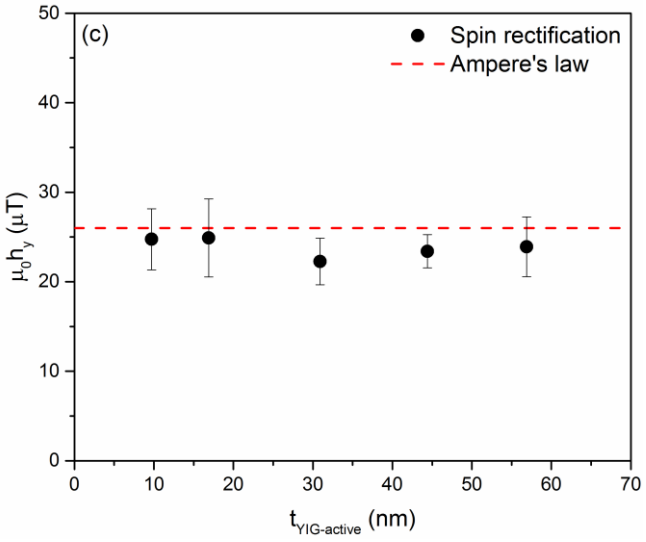


**Figure 4.12** Oersted field $\mu_0 h_y$ calculated from Ampere's law (red dashed line) and $V_{asy}$ using Eq. (3.7) (black dot) for each sample, normalized to $j_c = 10^{10}$ A/m$^2$.

identify the main driving mechanisms by comparing $V_{\text{sym-sin2}\theta\cos\theta}$ to $V_{\text{asy}}$. Figure 4.13 plots the ratio $V_{\text{sym-sin2}\theta\cos\theta}/V_{\text{asy}}$ in each sample against their effective damping parameter $\alpha_{\text{eff}}$, exhibiting a good linear relationship. Referring to Table 4.1, only $|V_{\text{Oe-SP}}/V_{\text{Oe-SR}}| \propto 1/\alpha_{\text{eff}}$, while the ratios between other terms have more complicated relationship with $\alpha_{\text{eff}}$, as $\alpha_{\text{eff}}$ also depends on $t_{\text{YIG}}$ (Eq. (4.1)). From this we conclude that $V_{\text{sym-sin2}\theta\cos\theta}$ can be mainly attributed to the spin pumping driven by the Oersted field.

Finally, we discuss the additional sin$\theta$ component $V_{\text{sym-sin}\theta}$ in the symmetric lineshape. This $V_{\text{sym-sin}\theta}$ is not negligible in magnitude compared with either $V_{\text{sym-sin2}\theta\cos\theta}$ or $V_{\text{BG}}$ as shown in Figure 4.10. However, as shown in Figure 4.13, differently from the case for $V_{\text{sym-sin2}\theta\cos\theta}/V_{\text{asy}}$, the ratio $V_{\text{sym-sin}\theta}/V_{\text{asy}}$ is less dependent on $\alpha_{\text{eff}}$ (or $t_{\text{YIG}}$). This sin$\theta$ component is also reported in some previous work on YIG/Pt [151]. We note that when measuring other material systems in our setup, e.g. Co/Pt [93] or Py/Pt [141], this sin$\theta$ component is absent, indicating its origin in the YIG/HM samples.

The $V_{\text{sym-sin}\theta}$ component indicates that the current-induced torque can drive the FMR even when the external field is perpendicular to the bar (i.e. $\theta = 90°$), where the torque induced by

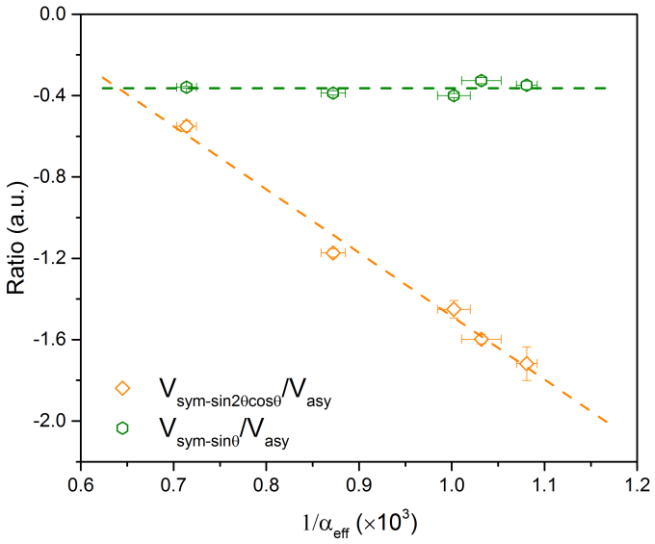


**Figure 4.13** Plot of the ratio $V_{\text{sym-sin2}\theta\cos\theta}/V_{\text{asy}}$ (orange) and $V_{\text{sym-sin}\theta}/V_{\text{asy}}$ (green) as a function of $1/\alpha_{\text{eff}}$, measured at 8 GHz. The dashed line represents the linear fitting.

either the Oersted field or STT is zero. Since the detection based on ISHE has an angle dependence of sin$\theta$, the torque induced by this unknown effective field should be independence from the in-plane angle $\theta$. Although we have not fully understood this point, we can exclude the possibility of an out-of-plane field induced by the non-uniformity of Oersted field by doing an out-of-plane angle-dependent measurement.

As shown in Figure 4.14(a), CI-FMR measurement is carried out with the external field applied in y-z plane with an arbitrary angle to y-axis. One example result is shown in Figure 4.14(b) and (c), measured from the sample YIG(14.8)/Pt at 8 GHz. In Figure 4.14(c), $V_{sym}$ and $V_{asy}$ components show the angle dependence of (sin2$\varphi$sin$\varphi$ + cos$\varphi$) and –sin2$\varphi$sin$\varphi$. In contrast, as deduced in Appendix B, if the resonance field is driven by a field-like torque from a field pointing to z-axis, $V_{sym}$ and $V_{asy}$ should have the angle dependence of $\cos^3\varphi$ and

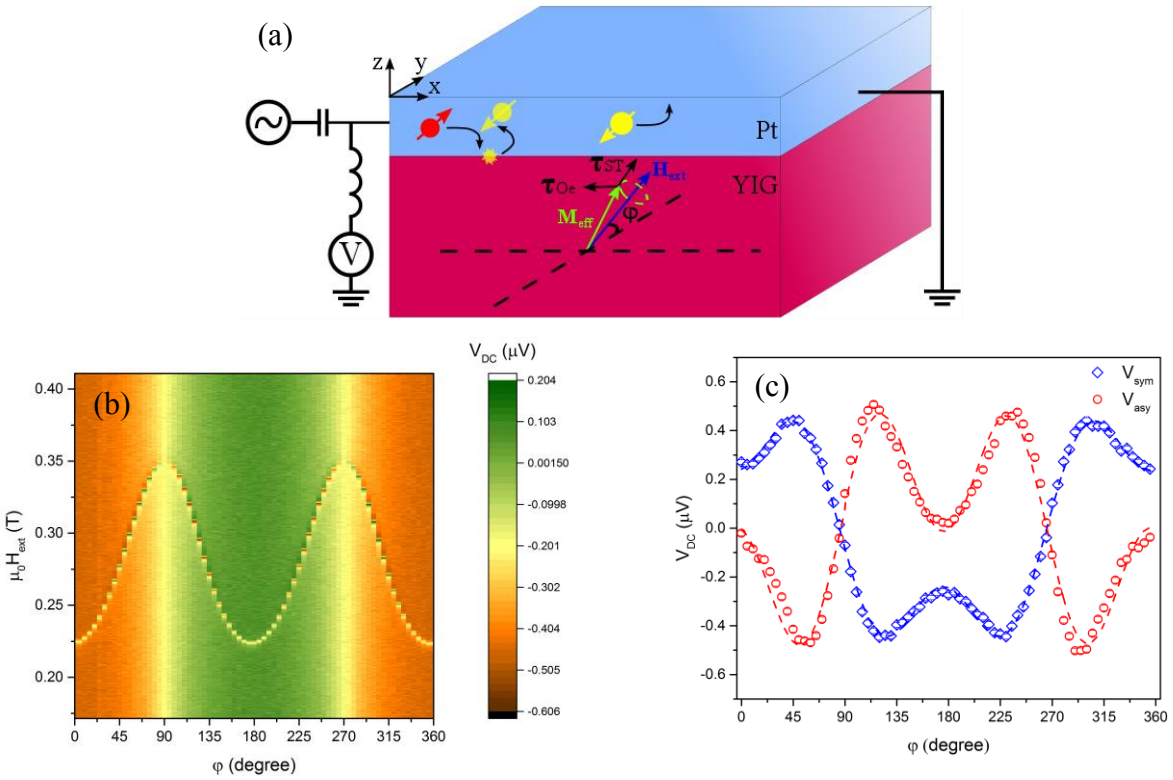


**Figure 4.14** (a) Experimental setup for an out-of-plane CI-FMR measurement. (b) The DC voltage mapping and (c) angle dependence of the amplitude of $V_{sym}$ and $V_{asy}$ components in FMR lineshape swept in y-z plane. The dashed line represents the trigonometric fitting.

$\sin2\varphi\cos\varphi$ respectively. However, neither of these two terms appears in Figure 4.14(c). Instead, the $\sin2\varphi\sin\varphi$ term in both $V_{sym}$ and $V_{asy}$ agrees with the symmetry of resonance signal driven by the in-plane Oersted field (see Appendix B). As a result, although we are still uncertain about the reason of the resonance at $\theta = 90°$, we can exclude the possibility of the out-of-plane field induced by the non-uniformity in Oersted field.

## 4.5 Discussion and future steps

We start with a brief summary of this chapter. We have used CI-FMR to investigate the charge-current-induced torque on YIG magnetization in a series of YIG/HM samples with different YIG thickness. In all of our samples, the Oersted field dominates over STT in driving magnetization dynamics, proven by the calculation of effective field and the relative amplitude of each component in the resonance signal. In addition, we also find that magnetization precession can also be driven even when the magnetization is parallel to both the spin polarization and the Oersted field, and the mechanism behind it is expected to be explored in future.

The main concern here is the absence of STT in our YIG/HM samples. From our lineshape shape analysis (section 4.1), rectification voltage $V_{sym\text{-}sin2\theta cos\theta}$ and $V_{asy\text{-}sin2\theta cos\theta}$ resulting from STT and Oersted field respectively should have the same sign for YIG/Pt, which are not observed in all of our samples. This result agrees with other papers focusing on the same topic [150,151,200]. However, Schreier et al. reported that the sign of $V_{sym\text{-}sin2\theta cos\theta}$ will be reversed when the thickness of YIG reduced to 4 nm which proved the existence of STT in YIG/Pt [146]. Spin-torque driven auto-oscillation has also been observed in a 20-nm YIG sample covered by Pt [91]. Therefore, we could not exclude the possibility of existence of STT in YIG/HM. To further analyse the reason behind, we make a summary of the YIG properties used in recent related work as Table 4.3. From the aspect of fabrication method, it shows that STT can be observed in YIG/Pt grown using the same method as ours (magnetron RF sputtering). However, the samples in [150] and [151] shows larger spin mixing conductance than ours which is $7.1 \times 10^{17}$ $m^{-2}$. The problem of the dead layer was not

observed as well. Therefore, one reason for the absence of STT may be the defect of our YIG/HM fabrication, which is expected to be improved in future. Another thing to notice is that the thickness used in [146], which is the only paper showing the same sign between $V_{sym}$ and $V_{asy}$, is only 4 nm. This provides a clue that it is necessary to have the YIG samples with thickness of several nanometres in order to observe $V_{sym}$ and $V_{asy}$ in the same sign, which is also supported by the recent theory [147]. This is also the work that should be investiagted in future.

**Table 4.3** Summary of the sample thickness, spin mixing conductance and fabrication methods of the related work for reference.

| Reference | Sample (nm) | $g_{eff}^{\uparrow\downarrow}$ ($m^{-2}$) | Method[19] |
|---|---|---|---|
| Schreier et al. [146] | YIG(4)/Pt(3) | $5.2 \times 10^{18}$ | LMBE |
| Hamadeh et al. [92] | YIG(20)/Pt(7) | $1.9 \times 10^{18}$ | PLD |
| Collet et al. [91] | YIG(20)/Pt(8) | $3.6 \times 10^{18}$ | PLD |
| Wang et al. [200] | YIG(20)/Pt(5) | Not reported | PLD |
| Sklenar et al. [150] | YIG(40)/Pt(6) | $1.9 \times 10^{18}$ | MRFS |
| Jungfleisch et al. [151] | YIG(40)/Pt(5) | $4.3 \times 10^{18}$ | MRFS |

Another question left is the sin$\theta$ component observed in $V_{sym}$ in all the samples. Similar results have also been observed in other works [150,151,200]. Sklenar et al. have attributed this component to the enhancement of SSE at FMR condition [150]. However, this still could not explain why resonance can be driven at $\theta = 90^{o}$, at which both STT and Oersted field provides zero torques to the magnetization. Moreover, if we assume that FMR can be driven at $\theta = 90^{o}$, the SSE effect should be enhanced because of the rise in temperature at FMR condition. However, from Figure 4.10 (e) and (f), we can clearly see that $V_{sym\text{-}sin\theta}$ has the opposite sign against the voltage from SSE at off-resonance. Instead, we might attribute the

[19] Abbreviations: PLD – pulsed laser deposition; LMBE – laser molecular beam epitaxy; MRFS – Magnetron radio-frequency sputtering

origin of $V_{\text{sym-sin}\theta}$ to the resonance of other spin wave modes, which could also generate the spin pumping signal. Different from FMR mode, the resonance at high modes could be generated, for example, via the parametric excitation. However, further investigation should be done in future.

In addition to the two topics discussed above, there are also some works that can be done further for better understanding of CITs in YIG/Pt systems. Firstly, thickness dependence measurement with several-nanometre thick YIG is desirable for further identification of the origin of CITs. Secondly, although the damping control via CIT has been reported [91,92] in YIG prepared by PLD. It is important to check whether the same phenomenon can be observed in the YIG grown by sputtering, since the fabrication methods and the YIG quality are one of the cores in YIG/HM system. Finally, it is also valuable to measure the variation of CITs against the temperature, which can help us to further understand the behaviour of CITs in YIG/HM.

# Chapter 5 Current-induced resonance in NiMnSb

Current-induced spin-orbit torques (SOTs) provide ways to electrically excite magnetization dynamics in some materials with bulk inversion asymmetry in their band structure, e.g. (Ga,Mn)As and NiMnSb [11,14]. Unlike the case of YIG/heavy metal (HM), where the spin current in YIG is generated by the neighbouring HM layer, the charge current is first polarized inside the (Ga,Mn)As itself via the spin-orbit coupling (SOC) and then interacts with the magnetization via the exchange interaction. In (Ga,Mn)As, the SOTs result from the broken inversion symmetry within the unit cell, and the symmetry of the SOTs is determined by the interface strain, where shear and tetragonal strains can lead to the effective spin-orbit field (SOF) in Rashba and Dresselhaus symmetry [11,14,201]. Remarkable SOT was first observed in strained, single-domain (Ga,Mn)As in 2009 [14], where Chernyshov et al. demonstrated that the current-induced SOT is sufficient to reversibly switching the magnetization of a microscale (Ga,Mn)As island. In their work, they applied a non-saturating magnetic field to a (Ga,Mn)As Hall bar and monitored the magnetization switching via the planar Hall effect [13,14,201]. The field was rotated in the sample plane with a DC current flowing through the Hall bar. The current-induced SOF assisted the magnetic domains switching between low-energy orientations, and was calculated from the shifts in the magnetization switching angle. Another approach is to use SOF dynamically to excite FMR. From a lineshape analysis of the rectified voltage, as described in Chapter 4, the magnitude and directions of the SOF was determined precisely [11,12].

Recently, the same method has been applied to probe the SOF in a different magnetic alloy, NiMnSb. Differently from (Ga,Mn)As, this half-Heusler alloy has a Curie temperature well above room temperature (about 730 K in bulk) [170]. Moreover, NiMnSb has a low Gilbert damping coefficient (in the order of $10^{-3}$) [170], which makes it an intriguing candidate for spintronic applications. Early spintronic studies of NiMnSb mainly focused on

the conventional giant magnetoresistance in spin valves [202–204] and its tunable magnetic anisotropy [172,205]. The anisotropy of NiMnSb is found to be sensitive to its lattice constant, which can be controlled by either varying the Mn concentration [172] or inducing external strains via a piezostack [205]. A variation in the composition of NiMnSb can result in both a change in the strength of the cubic anisotropy by more than one order of magnitude and a 90° rotation in the direction of the uniaxial anisotropy [172]. Moreover, the values of saturation magnetization, exchange stiffness and Gilbert damping factor are also reported to depend on the composition of the NiMnSb film: the stoichiometric composition gives the maximum values for the first two terms and a minimum value for the Gilbert damping factor [206].

Despite the extensive studies on the rich magnetic properties of NiMnSb for more than a decade, the electric manipulation of NiMnSb was only reported in the last two years. In 2015, Dürrenfeld et al. investigated the spin-transfer torque (STT) in Pt/NiMnSb bilayers using current-induced ferromagnetic resonance (CI-FMR) [207]. An antidamping-like STT was deduced from both the lineshape of the voltage generated by spin rectification and a change in linewidth under a DC current bias. However, the current required to fully compensate the damping was beyond the breakdown limit of the device, inhibiting the onset of the coherent auto-oscillation in NiMnSb [91,100]. Very recently, the relativistic SOT has been reported in single-layer NiMnSb bars patterned along the [110] and [-110] crystalline orientation using CI-FMR. Here, the field-like torque was found to be dominated by the Dresselhaus symmetry due to its non-centrosymmetric crystalline structure [15]. The field-like SOT was not observed along the [100] and [010] direction due to the absence of anisotropic magnetoresistance (AMR). The antidamping-like SOT was observed to be negligibly small.

In this chapter, we characterise the current-induced SOT in a NiMnSb sample by using CI-FMR. The first section introduces the AMR and the planar Hall effect (PHE) in NiMnSb. Different from the sample used in [15], which was slightly Ni-rich, our NiMnSb sample is stoichiometric. We observe that this difference has a significant impact on the magnitude of the SOT. In particular, we observe that the antidamping SOT is comparable in size to the field-like SOT and we are able to characterise the SOT in all the crystalline directions. After

charactering the properties of our NiMnSb samples using CI-FMR in the second section, we systematically estimate the field-like SOT and antidamping-like SOT in the third and fourth section respectively. In the final section, the perpendicular standing spin-wave (PSSW) resonance driven by SOT is observed, from which the exchange stiffness coefficient can be determined.

## 5.1 Characterisation of anisotropic magnetoresistance

This section presents the in-plane angle dependence of the longitudinal and the transverse magnetoresistance, where the transverse magnetoresistance is also known as the planar Hall effect. A phenomenological model previously derived for GaMnAs [26] is applicable to describe the AMR in NiMnSb because they share the same crystal symmetry. In this model, AMR in ferromagnetic materials with zinc-blende structure consists of a non-crystalline component and a crystalline component arising from the crystal symmetries. The expressions are [15,25]:

$$\frac{\Delta\rho_L}{\rho_{av}} \equiv \frac{\rho_L - \rho_{av}}{\rho_{av}} = C_I \cos\left(2\psi - 2\varphi\right) + C_{IC} \cos\left(2\psi + 2\varphi\right) + C_C \cos 4\psi + C_U \sin 2\psi \tag{5.1}$$

$$\frac{\rho_T}{\rho_{av}} = C_I \sin\left(2\psi - 2\varphi\right) - C_{IC} \sin\left(2\psi + 2\varphi\right) \tag{5.2}$$

where $\rho_{L/T}$ is the longitudinal/transversal resistivity and $\rho_{av}$ is the average longitudinal resistivity; $\psi$ and $\varphi$ are respectively the angles of magnetization and charge current with respect to the [100] direction. The first term with coefficient $C_I$ in both equations is the non-crystalline AMR term which depends solely on ($\psi$ − $\varphi$), i.e. the angle between the magnetization and the current. It is the AMR term we commonly discuss in ferromagnetic materials. The second term with coefficient $C_{IC}$ is the mixed crystalline-non-crystalline AMR contribution, while the third and the fourth terms with coefficient $C_C$ and $C_U$ in Eq. (5.1) are the cubic crystalline and the uniaxial crystalline AMR term respectively, originating from the

growth strain [15,25]. Additional higher-order terms with negligible amplitude are omitted here [25].

To simplify the analysis, we define $\theta = \psi - \varphi$ as the angle between the magnetization and the current. The expressions above can then be re-written as:

$$\begin{aligned}\frac{\Delta\rho_{L,(100)/(010)}}{\rho_{av}} &= C_C\cos 4\theta + (C_I + C_{IC})\cos 2\theta \pm C_U \sin 2\theta \\ \frac{\Delta\rho_{L,(-110)/(110)}}{\rho_{av}} &= -C_C\cos 4\theta + (C_I - C_{IC})\cos 2\theta \mp C_U \sin 2\theta\end{aligned} \tag{5.3}$$

$$\begin{aligned}\frac{\rho_{T,(100)/(010)}}{\rho_{av}} &= (C_I - C_{IC})\sin 2\theta \\ \frac{\rho_{T,(-110)/(110)}}{\rho_{av}} &= (C_I + C_{IC})\sin 2\theta\end{aligned} \tag{5.4}$$

Figure 5.1(a) plots the angle dependence of the longitudinal resistivity in NiMnSb Hall bars for four distinct crystalline directions. By fitting the data using Eq. (5.3), the four AMR coefficients can be obtained as (in the unit of $10^{-4}$): $C_I = -2.20 \pm 0.08$, $C_{IC} = 3.21 \pm 0.08$, $C_C = 0.06 \pm 0.03$ and $C_U = -0.01 \pm 0.01$. Clearly, the first two terms dominate, leading to a $\cos 2\theta$ AMR dependence in the [100] and [010] directions and a $-\cos 2\theta$ AMR dependence in the [±110] directions. Our results numerically agree with [15] within a reasonable range. However, the important difference is that the $C_I$ and $C_{IC}$ terms in our samples are not completely compensated as in [15], leading to an observable longitudinal AMR in the [100] and [010] directions.

We also measure the transversal resistivity as a function of $\theta$ as shown in Figure 5.1(b). We fit the data using Eq. (5.4) to get the AMR coefficients as (in the unit of $10^{-4}$): $C_I = -0.062 \pm 0.015$ and $C_{IC} = 0.080 \pm 0.015$. Similar to the results above, the two coefficients show opposite sign and the magnitude of $C_{IC}$ is larger than $C_I$. However, the absolute values of $C_{IC}$ and $C_I$ are more than one-order of magnitude smaller than those obtained from the

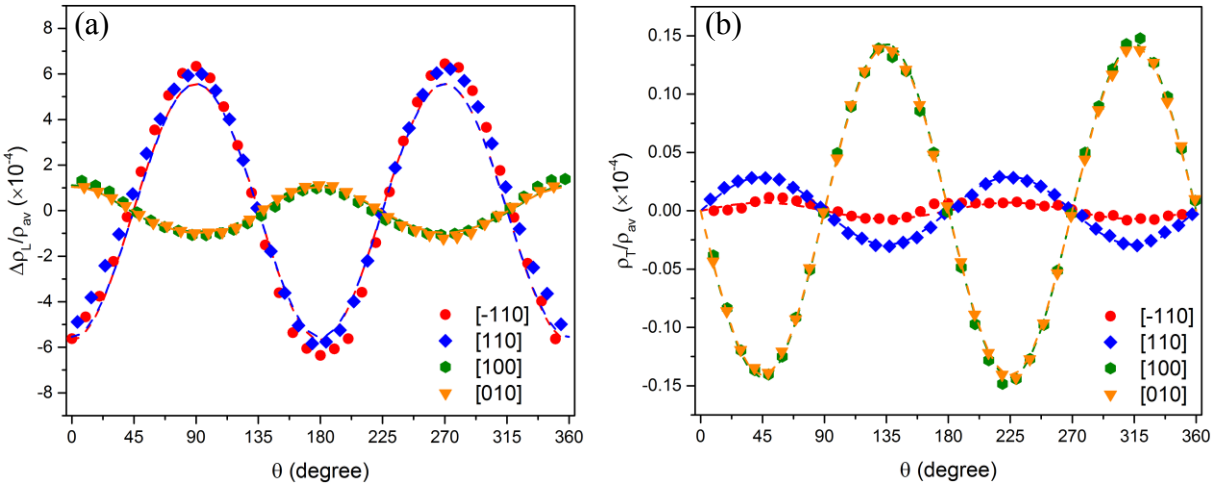


**Figure 5.1** Measurement of (a) longitudinal and (b) transversal AMR in NiMnSb Hall bars patterned in four distinct directions.

longitudinal resistivity measurement. We attribute this to the improper design of our Hall bars, where the contact point (5 μm in width) used to probe the transverse voltage is too wide compared to the width of the Hall bar (5 μm). This results in a current spreading near the probing area, leading to a reduction in transverse voltage. Nevertheless, the results from two measurements still agree with each other at a qualitative level.

## 5.2 Spin-orbit driven resonance in NiMnSb

We first present the results from the frequency-dependent CI-FMR measurement of a 4×40 $\mu m^2$ NiMnSb bar in the [110] crystalline direction. Figure 5.2 shows the DC voltage measured along the bar as a function of external field at different frequencies. The external field $H_{ext}$ is applied in the sample plane with an angle of $\theta$ = 30° to the bar as defined in Figure 3.5. The magnetic-field-independent background voltage is removed. The resonance signal is well described by a symmetric and an antisymmetric Lorentzians. The variation in signal level with frequency is attributed to the frequency-dependent attenuation of the circuit.

We repeat the measurement from 8 GHz to 25 GHz in order to get the dependence of the resonance field and the resonance linewidth on the microwave frequency as presented below

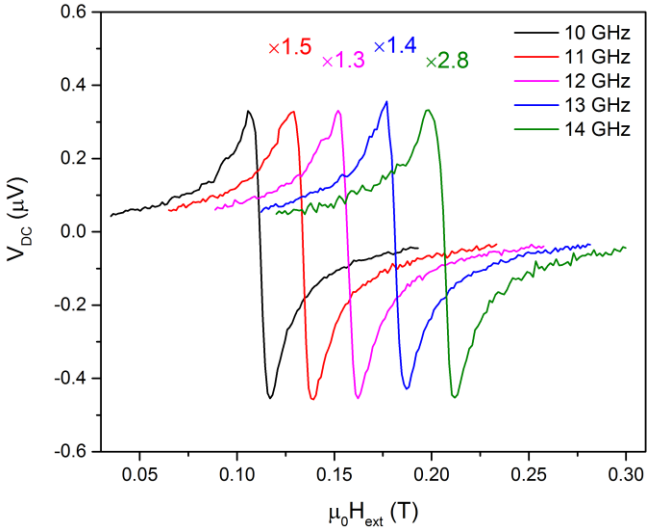


**Figure 5.2** Spectra of current-induced FMR measurement for a 4μm-wide NiMnSb bar in the [110] crystalline direction at 10-14 GHz, $\theta = 30°$.

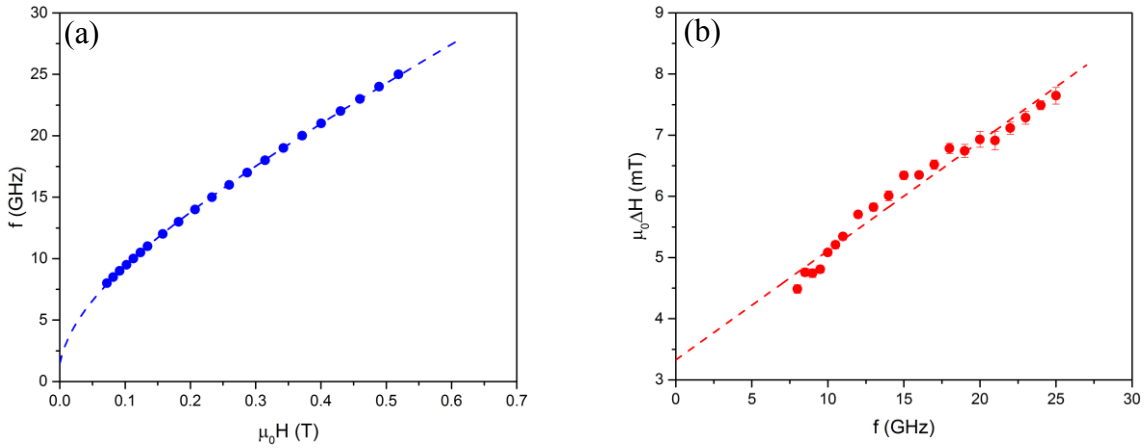


**Figure 5.3** Frequency dependence study for the same sample as in Figure 5.2. (a) Resonance frequency $f$ as a function of resonance field, fitted with the in-plane Kittel's formula (in dashed line). (b) Frequency dependence of the FMR linewidth $\Delta H$. The dashed line represents a linear fit.

in Figure 5.3(a) and (b) respectively. Figure 5.3(a) can be fitted well with the modified Kittel's formula (Eq. (2.25)), by assuming the value of gyromagnetic ratio $\gamma/2\pi$ to be 28 GHz/T. The Gilbert damping factor $\alpha$ can be obtained from the linear fitting of Figure 5.3(b)

using Eq. (2.29). We repeat the measurement of the bars in other three crystalline directions. The damping factors and the longitudinal AMR coefficient are summarized in Table 5.1.

**Table 5.1** Summary of average resistance, AMR coefficient and Gilbert damping factor for 4×40 $\mu m^2$ NiMnSb bars in four different crystalline directions.

| Direction | $R_{av}$ (Ω) | AMR ($10^{-3}$) | $\alpha$ ($10^{-3}$) |
|---|---|---|---|
| [110] | 97.4 ± 0.1 | −1.30 ± 0.02 | 5.0 ± 0.2 |
| [−110] | 104.2 ± 0.1 | −1.16 ± 0.01 | 4.3 ± 0.2 |
| [100] | 105.4 ± 0.1 | 0.20 ± 0.01 | 12.2 ± 0.4 |
| [010] | 98.0 ± 0.1 | 0.21 ± 0.01 | 17.2 ± 0.8 |

To probe the effective fields induced by the SOC, we carry angle-dependent measurements. In Figure 5.4, we show the DC voltage as a function of the external field's amplitude and angle $\theta$. We calibrate the microwave current density $J_c$ to be 1.3, 5.7, 4.7, 5.1 in units of $10^{10}$ A/m for the bars in (a) – (d) respectively using the method described in section 3.3.4. A resonance is clearly observed around $\mu_0 H_{ext}$ = 0.2 T. The reasonance field varies differently with $\theta$ for each bar due to the difference in anisotropy along four directions. We also note that there is a difference between the angle dependence of the non-resonance background voltage in each bar, which is discussed in more details in Chapter 6.

Figure 5.5 shows the fits of the angle dependence of the resonance field obtained by using Eq. (2.25). From the fits, the values of the anisotropy field are extracted and summarized in Table 5.2. As the NiMnSb film is patterned into bar structure, the in-plane compressive strain in NiMnSb is partially relaxed in the direction perpendicular to the long axis of the bar, regardless the crystalline directions of the bars [208,209]. According to [205], this will introduce an additional anisotropy term in NiMnSb along the relaxation direction. Similar phenomena was also observed and investigated intensively in (Ga,Mn)As [25,208–210]. Since the strain-induced anisotropy field and the demagnetization field are now parallel to each other, we show the sum of these two as $\mu_0 H_{sd}$; $\mu_0 H_{2//}$ and $\mu_0 H_{4//}$ are the uniaxial and

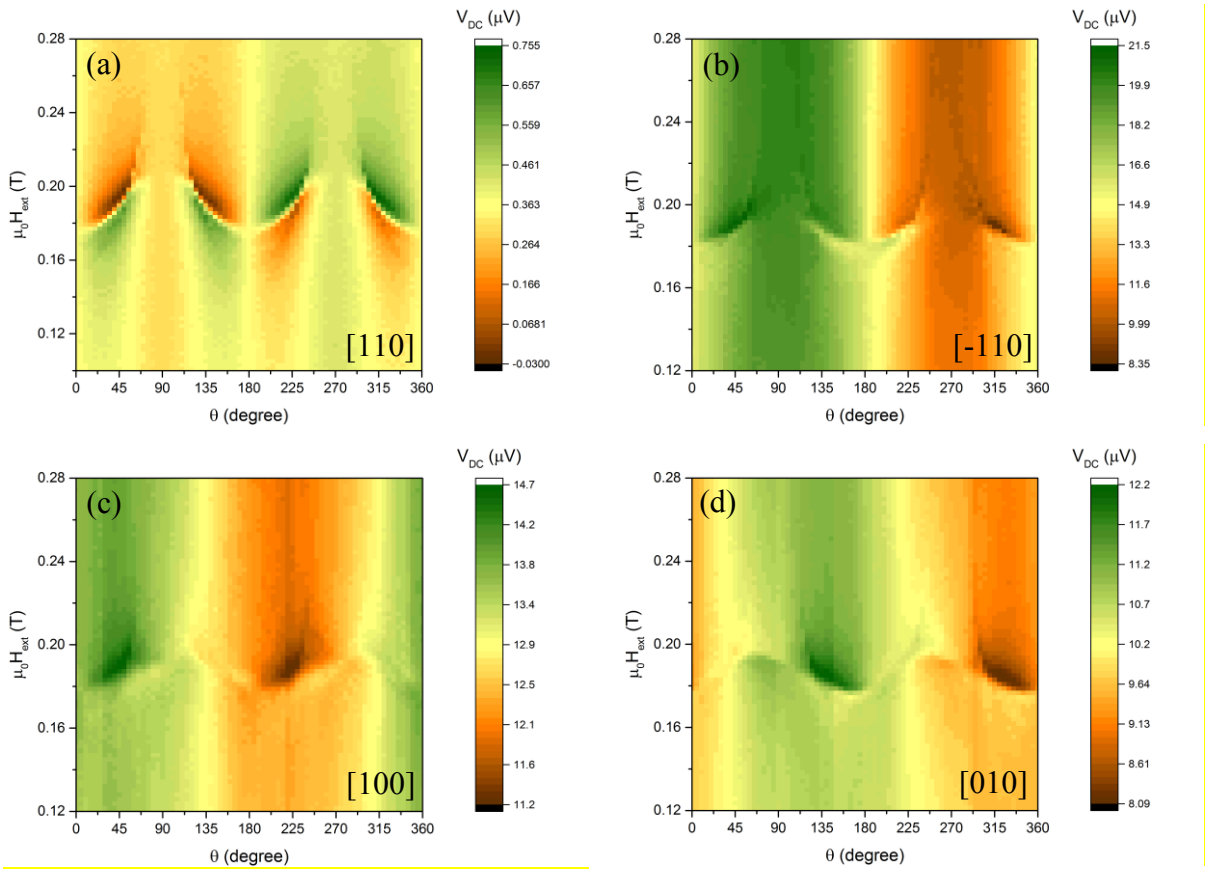


**Figure 5.4** The DC voltage along the bars in four different crystalline directions as a function of the amplitude and the angle $\theta$ of the external magnetic field, measured at 13GHz.

cubic crystalline anisotropy fields respectively; $\mu_0 M_{eff}$ is the effective magnetization including the out-of-plane anisotropy. We need to note that $\mu_0 H_{sd}$ is collinear with $\mu_0 H_{2//}$ along the [±110] directions, so their values cannot be extracted separately from the angle dependence of resonance field in this case. Differently from the results in [15] where the [110] and the [-110] directions mainly show a uniaxial and a cubic terms in the in-plane crystalline anisotropy, in our samples the anisotropy is mainly described by a uniaxial term, while the cubic term is relatively small. This difference, again, is attributed to the change in stoichiometry, where the magnetic anisotropy of NiMnSb strongly depends on the Mn concentration [172].

**Table 5.2** Summary of anisotropy fields (in mT) in the 4-μm NiMnSb bars in four crystalline directions.

| **Direction** | $\mu_0 H_{sd}$ | $\mu_0 H_{2//}$ | $\mu_0 H_{4//}$ | $\mu_0 M_{eff}$ |
|---|---|---|---|---|
| [110] | −20.3 ± 0.1 | | 3.5 ± 0.1 | 631.3 ± 0.3 |
| [−110] | −16.0 ± 0.1 | | 4.0 ± 0.1 | 642.1 ± 0.4 |
| [100] | −4.7 ± 0.9 | −7.4 ± 0.2 | 2.6 ± 0.1 | 602.4 ± 0.2 |
| [010] | −5.8 ± 0.7 | −7.6 ± 0.4 | 2.0 ± 0.1 | 602.9 ± 0.7 |

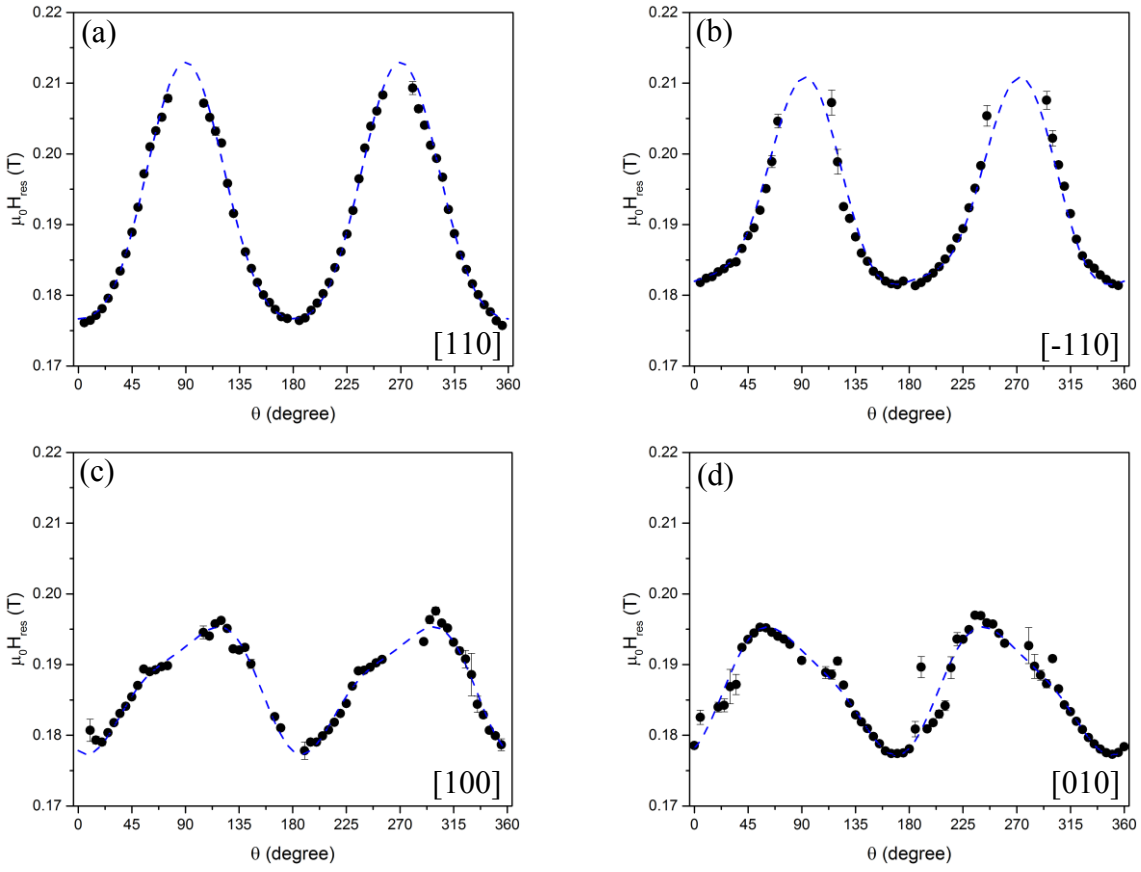


**Figure 5.5** The angle dependence of the resonance field for bars patterned in four crystalline directions measured at 13GHz and fitting (dashed line).

In order to determine the SOF, we fit the angle dependence of the resonance in the rectified voltage (Figure 5.6) using Eq. (3.5)-(3.7), distinguishing symmetric and antisymmetric contributions. The figure is plotted as a ratio of $V_{sym}/A_{sym}$ ($V_{asy}/A_{asy}$) rather than $V_{sym}$ ($V_{asy}$). This is because the coefficients $A_{sym}$ and $A_{asy}$ also depend on the direction of the magnetization, and its dependence is not negligible if the sample is anisotropic. The values of the SOF components extracted for each bar are summarized in Table 5.3, normalized to a unit current density of $J_c = 10^{11}$ A/m$^2$. It is important to remark that for our analysis we have made the assumption of a small-precession-angle approximation, which implies that the values of $V_{sym}$ and $V_{asy}$ are linear in the microwave power (Figure 5.7 for example). We need to point out that we have modified Eq. (3.6) by fitting the term $V_{sym}/A_{sym}$ with the antidamping-like

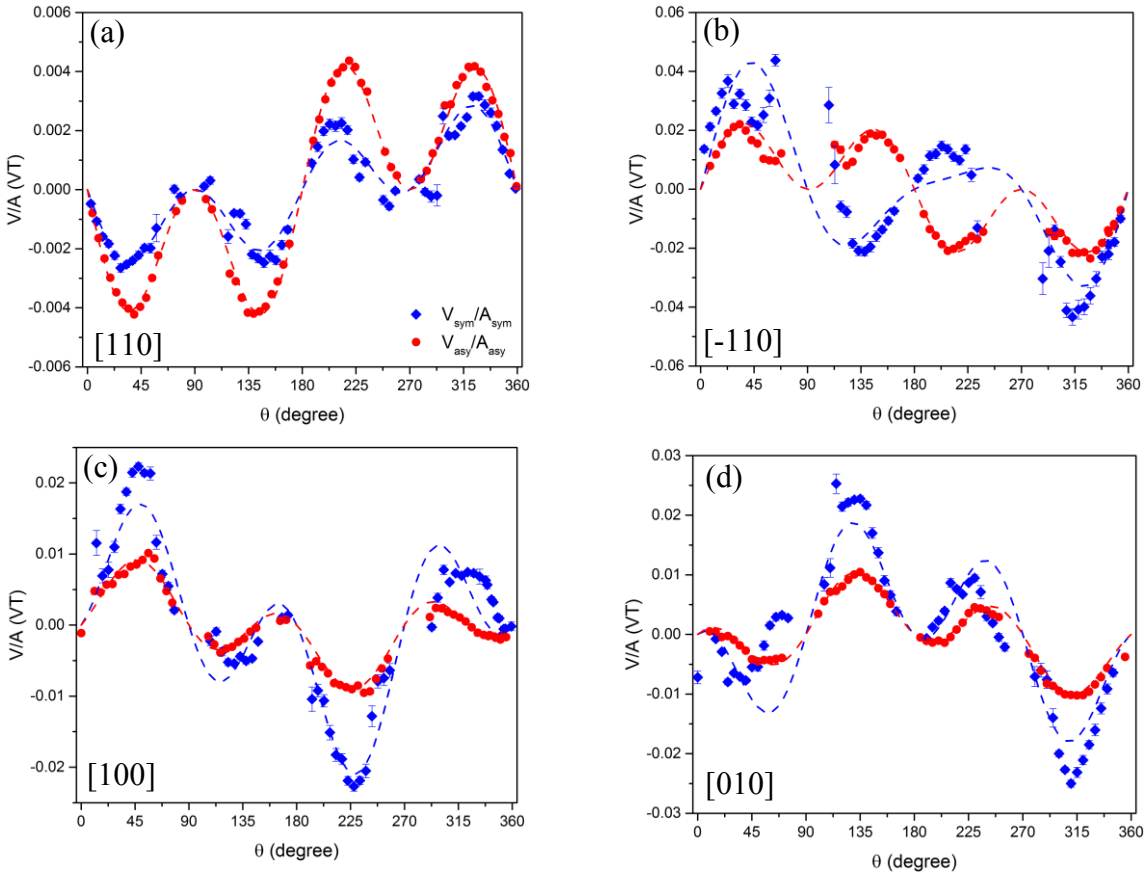


**Figure 5.6** Angle dependence of the symmetric (blue) and antisymmetric (red) components of the resonance in the rectified voltage for four bars patterned in four crystalline directions.

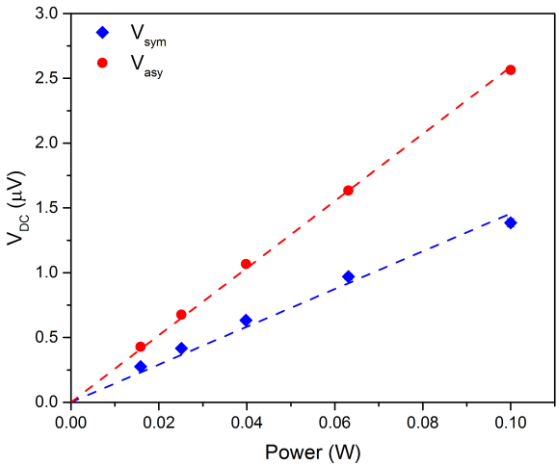


**Figure 5.7** An example of power dependence of $V_{sym}$ and $V_{asy}$ for a bar along the [100] direction, measured at $f = 13$ GHz and $\theta = 45°$, linearly fitted by the dashed line.

SOF $h_z$ as a sum of three different components: $h_z = h_{z0} + h_{zsin}\sin\theta + h_{zcos}\cos\theta$. This is because the out-of-plane component of the SOF should strongly depend on the orientation of the magnetization [12].

**Table 5.3** Summary of spin-orbit effective fields (in μT, normalized to $J_c = 10^{11}$ A/m$^2$) in the 4μm NiMnSb bars along four crystalline directions.

| Direction | $\mu_0 h_x$ | $\mu_0 h_y$ | $\mu_0 h_{z0}$ | $\mu_0 h_{zsin}$ | $\mu_0 h_{zcos}$ |
|---|---|---|---|---|---|
| [110] | −0.1 ± 3.8 | 414.4 ± 3.6 | 31.0 ± 8.4 | −28.9 ± 12.7 | 222.3 ± 11.8 |
| [−110] | 2.4 ± 3.2 | −78.1 ± 2.7 | −63.8 ± 7.1 | −22.2 ± 5.8 | −51.5 ± 9.7 |
| [100] | −225.6 ± 6.5 | 155.7 ± 7.3 | −60.9 ± 19.4 | 542.5 ± 32.0 | 269.7 ± 38.1 |
| [010] | 226.3 ± 7.9 | 127.0 ± 7.1 | −10.0 ± 9.9 | −507.7 ± 40.4 | 130.7 ± 46.1 |

### 5.2.1 Field-like spin-orbit torque

The in-plane components ($h_x$ and $h_y$) of the effective field can be most clearly represented by a polar diagram (Figure 5.8), where the arrows represent both direction and relative

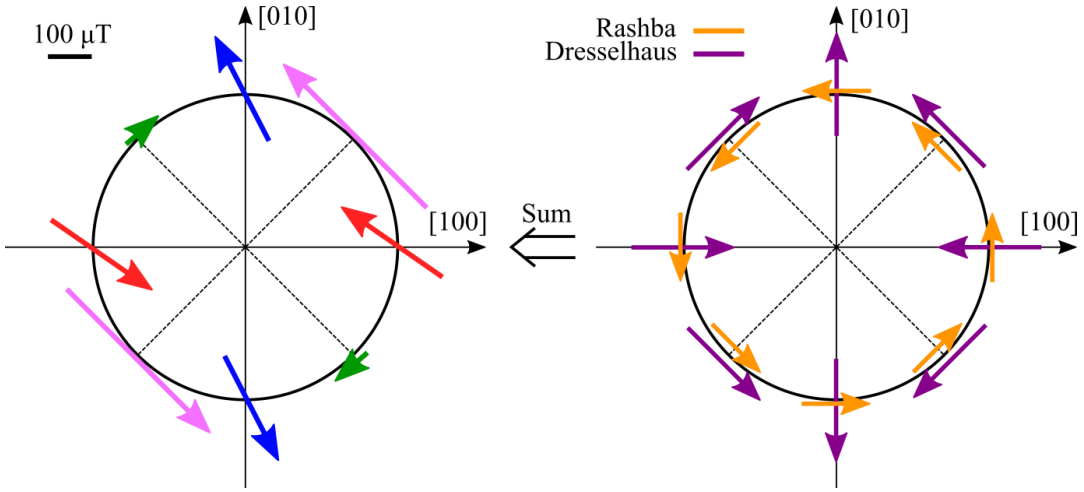


**Figure 5.8** Polar plot of the magnitude and direction of the in-plane current-induced effective field (left) and decomposition in Rashba and Dresselhaus contributions (right) for a current density of $J_c = 10^{11}$ A/m$^2$.

amplitude of the in-plane SO field for the different crystal directions. The polar plot on the right represents a decomposition of a Rashba $\mu_0\mathbf{h}_R$ = (155 ± 24) μT and a Dresselhaus $\mu_0\mathbf{h}_D$ = (236 ± 19) μT contributions (these values are for a current density of $J_c = 10^{11}$ A/m$^2$). The Dresselhaus term originates from the zinc-blend crystalline structure of NiMnSb, while the Rashba term comes from the shear strain together with possible partial strain relaxation, similar to the case of (Ga,Mn)As [11,15,211], though its origin is not completely understood. Compared with ref. [15], where the Dresselhaus field ($\mu_0 h_D$ = 445 ± 54 μT) is dominant over the Rashba field ($\mu_0 h_R$ = 105 ± 54 μT), these two terms are comparable in our sample. We again attribute this difference to the variation in Mn concentration.

### 5.2.2 Antidamping-like spin-orbit torque

Similar to the case of (Ga,Mn)As [12], we also expect an intrinsic antidamping-like SOT originating from the berry curvature in NiMnSb, but at room temperature. As introduced in section 2.4.2, this antidamping-like torque results from a scattering-independent process which can be visualized by solving the Bloch equations for the spins during the acceleration of the carriers between scattering events [12]. Unlike the effective field from field-like SOT

which is independent of the magnetization, the field from antidamping-like SOT purely originates from the band structure of the materials, and the torque it induces has the form of **M**×(**M**×**P**(**E**)), where **P**(**E**) is an in-plane vector proportional to the electric field **E** and its symmetry depends on the SOC (i.e. Rashba or Dresselhaus effect). From the expression of the torque, we see that the effective SOF **M**×**P**(**E**) is an out-of-plane vector and depends on both the electric field **E** and the magnetization **M**. In Table 5.4, we summarize its symmetry for different crystalline directions.

**Table 5.4** Symmetry of the effective field generating antidamping-like torques and originating from the Rashba and Dresselhaus SOC for an applied electric field **E** in different crystalline directions [12]. $\theta$ is the angle between **E** and **M**, as defined in Figure 3.5.

| SOC | [110] | [-110] | [100] | [010] |
|---|---|---|---|---|
| **Rashba** | $\cos\theta$ | $\cos\theta$ | $\cos\theta$ | $\cos\theta$ |
| **Dresselhaus** | $\cos\theta$ | $-\cos\theta$ | $\sin\theta$ | $-\sin\theta$ |

We now come back to the measured results of the out-of-plane effective SOF from which the antidamping-like torque originates (i.e., $h_{z0}$, $h_{z\sin}$ and $h_{z\cos}$ terms in Table 5.3). As expected, the angle dependence is dominated by a $\cos\theta$ term for both the [110] and the [-110] directions, but with opposite signs. This indicates that the Dresselhaus term is larger than the Rashba in our NiMnSb samples, agreeing with our measurement of the in-plane SOF (Figure 5.8). As for the [100] and the [010] directions, the antidamping-like effective SOF is a combination of a $\sin\theta$ term from the Dresselhaus contribution of the SOC and a $\cos\theta$ term from the Rashba contribution. These results well agree with the symmetry summarized in Table 5.4. The constant term $h_{z0}$ independent on the angle $\theta$, on the other hand, is attributed to a random error from the measurement and the fitting [12].

As an independent measurement of the antidamping-like SOT, we quantified the change in FMR linewidth as a function of an applied DC current. Similar to the case of STT [47,92,212], the antidamping-like component of the torque is expected to increase or

decrease the damping factor and hence the linewidth, depending on its direction with respect to the magnetization. Magnetic field modulation (section 3.3.3) is employed in this set of measurement in order to eliminate the huge background voltage resulting from a bolometric effect where amplitude modulation is employed [126]. Figure 5.9 (a-d) presents the measured FMR spectra at 13 GHz in [±100] bars with the magnetic field applied along $\theta$ = 30° and 210°. Unlike previous measurement where only the uniform mode is present, we observed multiple peaks in (a-d), which are corresponding to the additional spin wave modes. Therefore, we fit the spectra with multiple Lorentzian functions, while only the linewidth for the uniform mode (the one at the highest field) is what we concern.

From the fitting, we can obtained the linewidth of uniform mode as a function the DC bias current for the bars along the [110] and the [-110] directions as Figure 5.9 (e) and (f) respectively. The term $\Delta(\mu_0\Delta H) = \mu_0(\Delta H_{\text{biased}} - \Delta H_{\text{zero-bias}})$ is the change in linewidth under DC bias with respect to the linewidth without bias. In both bars, the linewidth changes linearly with the bias current, and the slope is revered when the external field is turned by 180°. Moreover, when comparing the results for along the [110] and the [-110] directions, we can find that the slope is opposite for the same angle $\theta$ and larger in the [110] direction compared to the [-110] direction. All of these findings agree with the results in Table 5.3, where the out-of-plane effective field is dominated by a $h_{\text{zcos}}$ term in both directions, and it has a larger magnitude and the opposite sign in the [110] direction compared with that in the [-110] direction. Following the method in [213], we can assume that the antidamping torque has a format of:

$$\tau_{AD} = \frac{\gamma a_J}{M_s}\mathbf{M}\times(\boldsymbol{\sigma}\times\mathbf{M}) \tag{5.5}$$

where σ is a unit vector of spin polarization induced by SOC; $a_{\text{j}}$ is the amplitude of the effective antidamping field at the current density of $j$. It has a similar format of the Landua-Lifshitz equation (2.18), where $\lambda = \gamma\alpha/(1+\alpha^2) \approx \gamma\alpha$. Therefore, the critical condition where the antidamping-like effective field can fully compensate the damping will be $a_{\text{j}} = \alpha H_{\text{res}}$. Since the linewidth of [110] and [-110] bar without bias are measured to be 6.2 ± 0.2 mT and

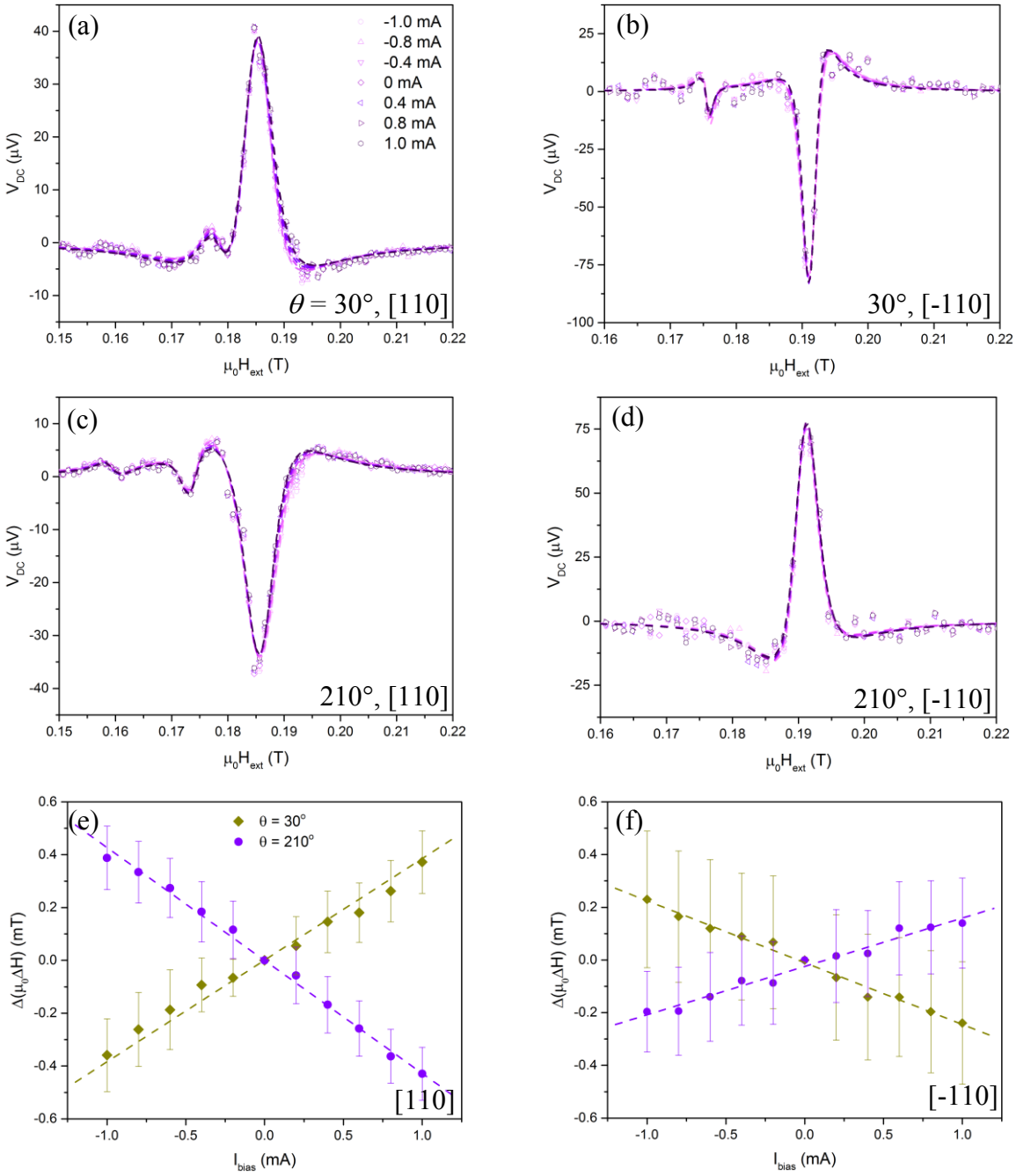


**Figure 5.9** (a-d) Spectra of current-induced FMR measurement along [±110] with different DC bias current at 13 GHz. Magnetic field is applied along $\theta = 30°$ and 210° from the bar direction. Dashed lines represent the fitting with multiple Lorentzian functions. (e-f) Change of FMR linewidth as a function of DC bias current for bars along [±110] directions at 30° (green) and 210° (purple)

5.8 ± 0.3 mT respectively, so from as Figure 5.9 (e) and (f), we can determine the critical current that fully compensates the damping to be 16.7 ± 6.7 mA and 23.2 ± 20.8 mA, which corresponds to a current density of 1.18 ± 0.47 and 1.63 ± 1.46 in a unit of $10^{11}$ A/m$^2$. We can then determine the amplitude of the effective antidamping-like field $a_j$ to be 779.7 ± 310.6 and −487.8 ± 436.9 μT at j = $10^{11}$ A/m$^2$ for [110] and [−110] bars respectively. Compared with the values of the cosine term in Table 5.3, the results agree with each other if taking the large error range into consideration. We may attribute this error to the signal quality in magnetic field modulation and the mathematical fitting, which is expected to be improved in future. Despite of this, differently from [15], where the antidamping-like torque is negligibly small, our measurement is the first of an antidamping-like SOT in a bulk material at room temperature.

## 5.3 Exchange spin wave resonance in NiMnSb

When the frequency of the microwave current goes above ~15 GHz, another resonance peak in addition to the uniform FMR mode can be observed when sweeping the external magnetic field. Figure 5.10 shows contour maps of the FMR measurement at 20GHz for bars along four crystalline directions. We notice that the two resonance modes share the same anisotropy and are well-separated by a ~0.3T gap from each other. The resonance at higher magnetic field is the uniform FMR mode, while the one at lower field can be attributed to the first PSSW mode [80,206,214], which has a wave vector pointing out of the film plane. Its wavelength, amplitude and phase strongly depend on the film thickness and the surface pinning conditions, but little on the crystalline directions of the bars.

To explore the characteristics of the PSSW mode, we carry out a frequency dependent measurement with the external magnetic field applied in the film plane, at an angle $\theta = 30°$ away from the bar direction. Figure 5.11 gives an example result for a [110] bar the diagrams for the bars in other directions are very similar). Similar to the uniform mode, the resonance

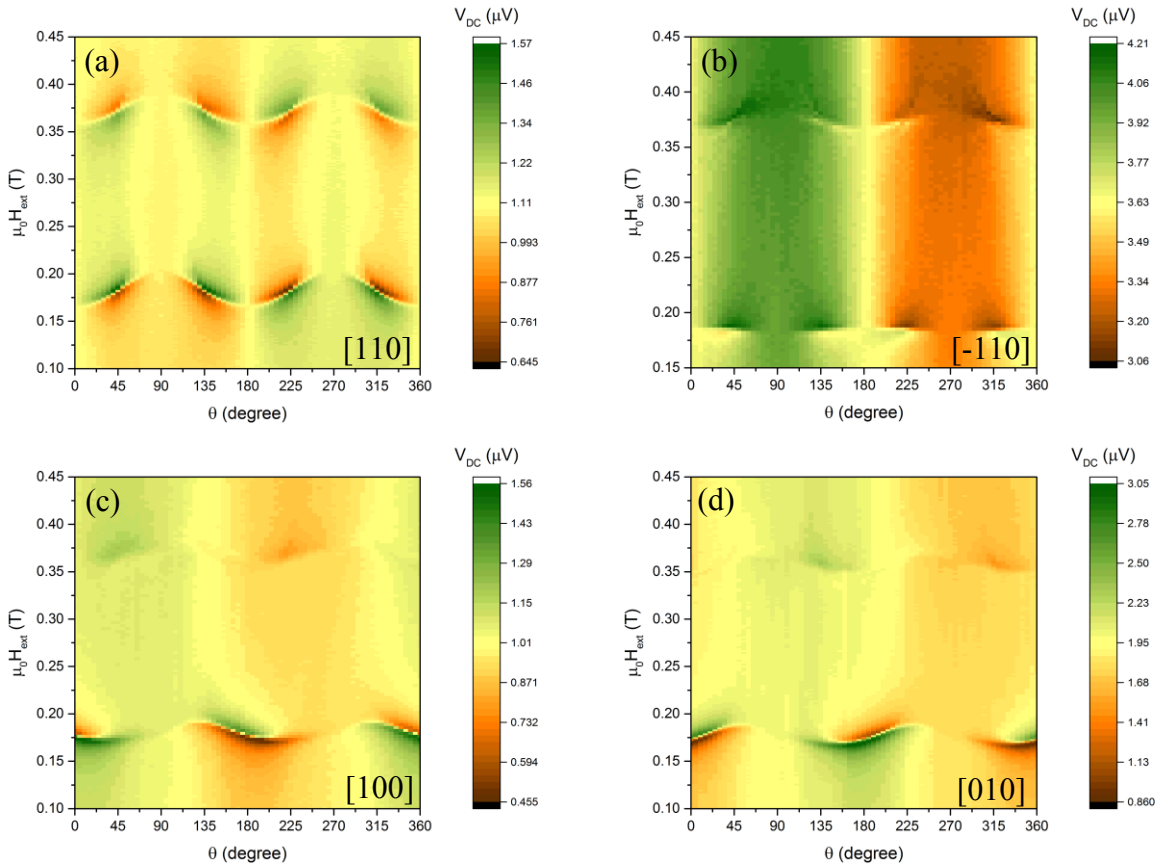


**Figure 5.10** 2D plot of the rectified voltage along the bars in four different crystalline directions as a function of the amplitude and the angle $\theta$ of the external magnetic field, measured at 20 GHz.

of PSSW can also be well described by using the modified Kittel's formula (Eq. (2.25)), but with the term $H_{\text{res}}$ being replaced by $H_{\text{res}} + H_{\text{ex}}$:

$$f = \frac{\mu_0 \gamma}{2\pi}\left(H_{res} + H_{ex} + H_1\right)\left(H_{res} + H_{ex} + H_2\right) \tag{5.6}$$

$H_1$ and $H_2$ are defined in Eq. (2.26) and (2.27), and the term $H_{\text{ex}}$ represents the exchange field:

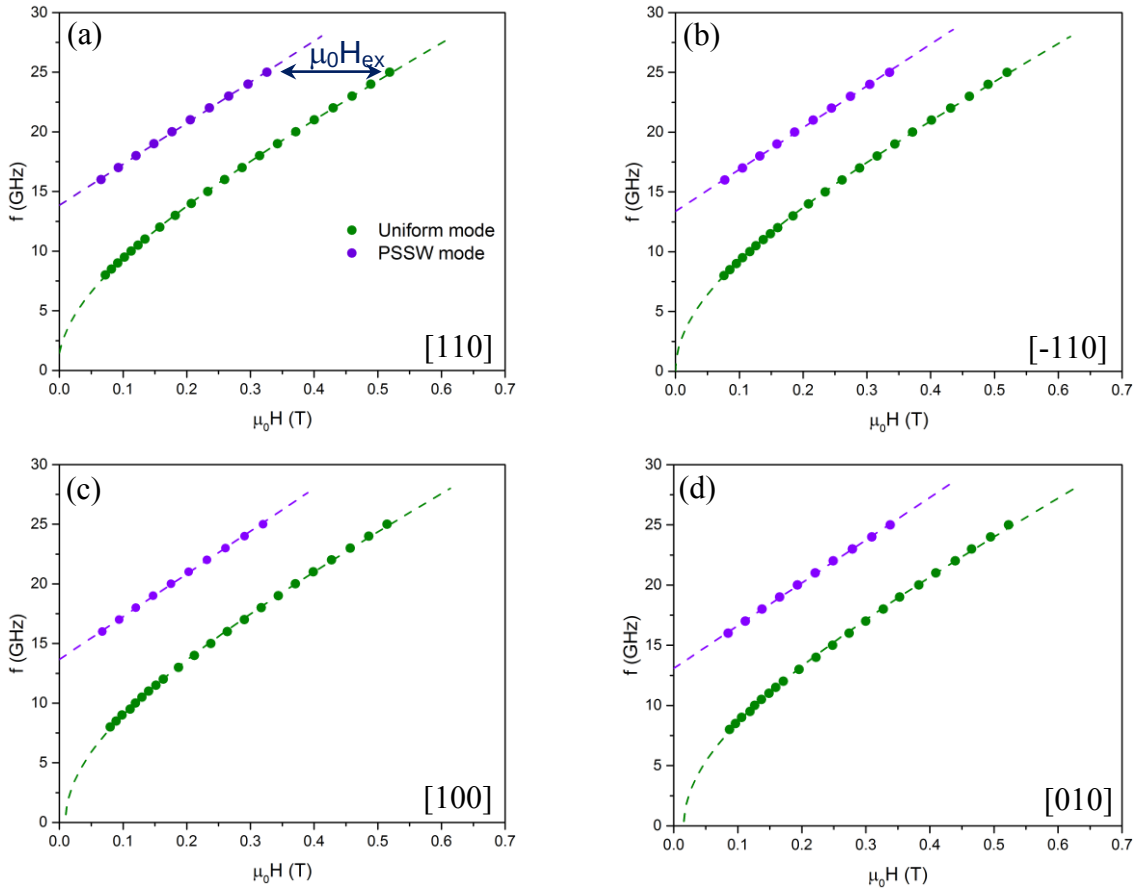


**Figure 5.11** Resonance frequency $f$ as a function of resonance field for the uniform mode (green) and the PSSW mode (purple) for bars along different crystal directions, fitted with the modified Kittel's formula (dashed line). The two modes are offset by the exchange field $H_{ex}$.

$$H_{ex} = \frac{2A}{\mu_0 M_s}\left(\frac{n\pi}{t}\right)^2 \tag{5.7}$$

where the parameters $A$, $n$ and $t$ represent the exchange stiffness, the order of the PSSW mode and the film thickness respectively. Therefore, $H_{ex}$ gives the offset in magnetic field between the uniform and the PSSW mode as (Figure 5.11). Given the value of $\mu_0 M_s = 0.90 \pm 0.01$ T, $t = 34 \pm 1$nm and $n = 1$, we can calculate the value of $A$ for each bar as: $A_{[-110]} = 7.9 \pm 0.1$ pJ/m, $A_{[110]} = 8.1 \pm 0.1$ pJ/m, $A_{[100]} = 8.1 \pm 0.1$ pJ/m, $A_{[010]} = 7.9 \pm 0.1$ pJ/m. As expected, $A$ varies little for different crystalline directions, and the value obtained here agrees well with a

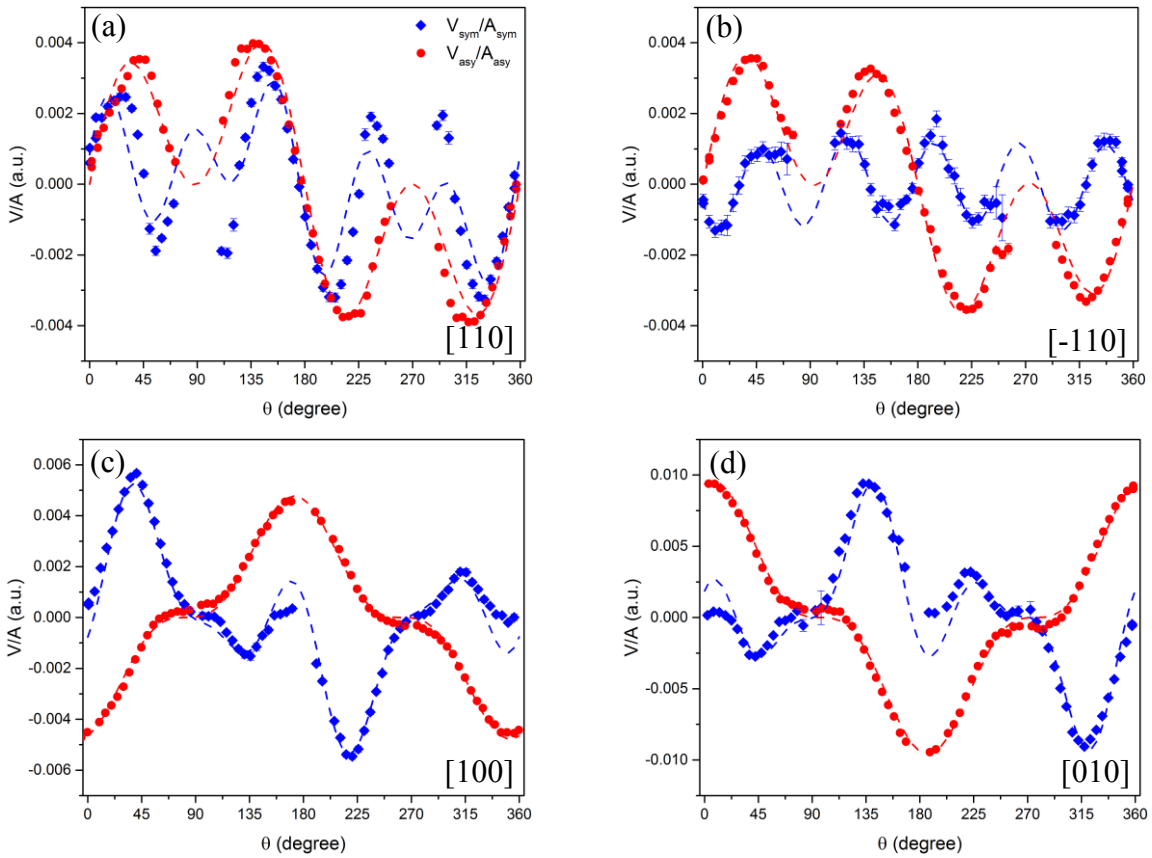


**Figure 5.12** The symmetric (blue) and antisymmetric (red) components in rectified voltage in the exchange PSSW resonance mode as function of angle $\theta$ from the bars in four crystalline directions, measured at 20 GHz.

previous report ($A$ = 8 pJ/m) for a NiMnSb thin film with the same as the one of our sample [206].

We further look into the PSSW mode by plotting the angle dependence of the rectified voltage at resonance in Figure 5.12. For the antisymmetric Lorentzian component $V_{asy}$, the angle dependence for both [±110] bars is dominated by a $+\sin 2\theta\cos\theta$ term for the PSSW mode, whereas it follows a $-\sin 2\theta\cos\theta$ angle dependence in the uniform mode for the [110] bar (Figure 5.6). When it comes to the [100] and [010] directions, the $V_{asy}$ component can be fitted well with a $\pm\cos^3\theta$ function for the PSSW mode, rather than the combination of $\sin 2\theta\cos\theta$ and $\sin 2\theta\sin\theta$ as for the uniform mode. The symmetric Lorentzian component has

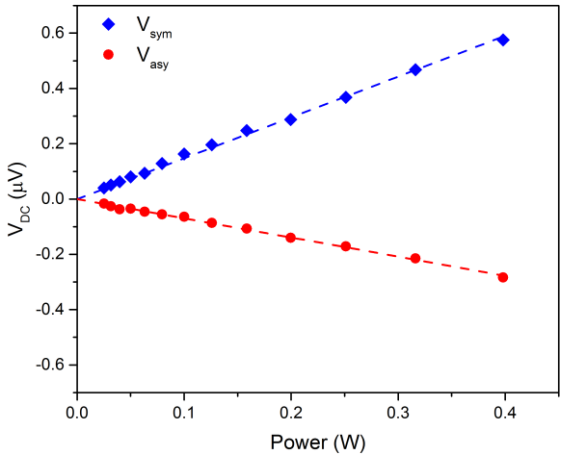


**Figure 5.13** Power dependence of $V_{sym}$ (blue) and $V_{asy}$ (red) for the PSSM mode for the bar along the [100] direction, measured at $f = 20$ GHz and $\theta = 45°$, fitted by a linear dashed line.

more complicated angle dependence for the PSSW. To precisely fit it, we need to introduce a $\sin 5\theta$ component for the bars along [±110] (or a $\cos 5\theta$ component for the [100] and the [010] bars). Figure 5.13 shows the power dependence of the DC voltage from the resonance in PSSW mode. Similar to the case of the uniform mode (Figure 5.7), both $V_{sym}$ and $V_{asy}$ are linear in microwave power. To interpret these results, we cannot follow the same analysis outlined in section 3.3.2, which assumes the uniform precession of the magnetization. A theory for analysing the amplitude and the polarity of the rectified signal of the spin waves would require averaging the spin dynamics throughout the out-of-plane direction. However, in this case other forms of rectification, by GMR for example, would also need to be included.

## 5.4 Discussion and future steps

We start with a brief summary of this chapter. We first measured the AMR in NiMnSb, and found that the AMR consists of crystalline and non-crystalline components of opposite sign. In the second part (section 5.2), a complete mapping of the spin-orbit effective field in our NiMnSb samples was done using CI-FMR. We found that the in-plane effective field consists of a Dresselhaus component of $h_D = 236 \pm 19$ μT and a Rashba component of $h_R = 155 \pm 24$ μT for a current density of $J_c = 10^{11}$ A/m$^2$. The out-of-plane effective field

originating from the Berry curvature is also found to have two contributions of Rashba and Dresselhaus symmetries. Its antidamping-like behaviour is further investigated by measuring the linewidth changes under a DC current bias. By comparing with the previous work in [15], we conclude that not only the AMR and the magnetic anisotropy but also the SOTs in NiMnSb can be tuned by varying the stoichiometry. Finally, we find that the SOTs can also drive a perpendicular standing spin-wave resonance mode, from which we can determine the exchange stiffness constant to be $A = 8.0 \pm 0.2$ pJ/m.

In addition to the works summarized above, there are still several things that can be done in future. The first one is to investigate the SOTs in more NiMnSb samples with different stoichiometry. Our work has shown that the SOTs is sensitive to stoichiometry, measurement on NiMnSb in other stoichiometry, ranging from Ni-rich to Mn-rich as shown in Figure 3.1, are desired to have a complete picture on stoichiometric control of SOTs in NiMnSb. Secondly, the temperature dependence of SOT in NiMnSb in different stoichiometry is also valuable to investigated. Although SOT can be detected at room-temperature, temperature dependence measurement can give us a deeper understanding on the mechanism behind. Thirdly, it is important to see whether magnetization switching can be done in NiMnSb, similar to the work Chernyshov et al. have done in (Ga,Mn)Sb [14]. As antidamping-like torques are observed and proven here, this also provides us opportunities to build auto-oscillators using bulk NiMnSb. Finally, in a broader picture, NiMnSb is a member of the big half-Heusler alloy family, other members, such as CoTiSb, IrMnSb and so on, could also exhibit SOTs at room temperature, which can offer more opportunities and flexibility in building SOT-based spintronic devices

# Chapter 6 Unidirectional spin-orbit magneto-resistance in NiMnSb

In the previous chapter, we have shown that a non-equilibrium spin polarization can be generated in some classes of non-centrosymmetric magnetic crystals, and the corresponding effective field can induce spin torques to the magnetization. This provides means to electrically manipulate ferromagnets without the assistance of either an external magnetic field or externally polarized currents. The initial experimental evidence of reversible control of magnetization via spin-orbit torques has been reported in (Ga,Mn)As at a temperature of $T$ = 50 K [14], while our measurement on NiMnSb can potentially extend applications to the room temperature. The remaining challenge, however, is to find the counterpart read scheme to identify the 180° magnetization reversal in these bulk systems. The anisotropic magnetoresistance (AMR) is not suitable for this purpose as it is symmetric with respect to 180° flips of the magnetization.

In this chapter, we report the observation of the unidirectional spin-orbit magnetoresistance (USOMR) in NiMnSb. In the conventional giant magnetoresistance (GMR) as shown in Figure 6.1 (a), the first ferromagnetic layer induces a non-equilibrium spin polarisation, and the scattering rate of carriers in the second ferromagnetic layer, thus the resistance of the junction, depends on the relative orientation of this spin with the local magnetization. In NiMnSb, the charge current develops a non-equilibrium component of the spin polarization due to the spin-orbit coupling (SOC) along the direction of the spin-orbit field (SOF) (Figure 5.8 in our work). This component depends on the crystalline direction of the bar and is not necessarily aligned with the magnetization, resulting in a low (high) resistivity if it is parallel (anti-parallel) to the magnetization as shown in Figure 6.1 (b).

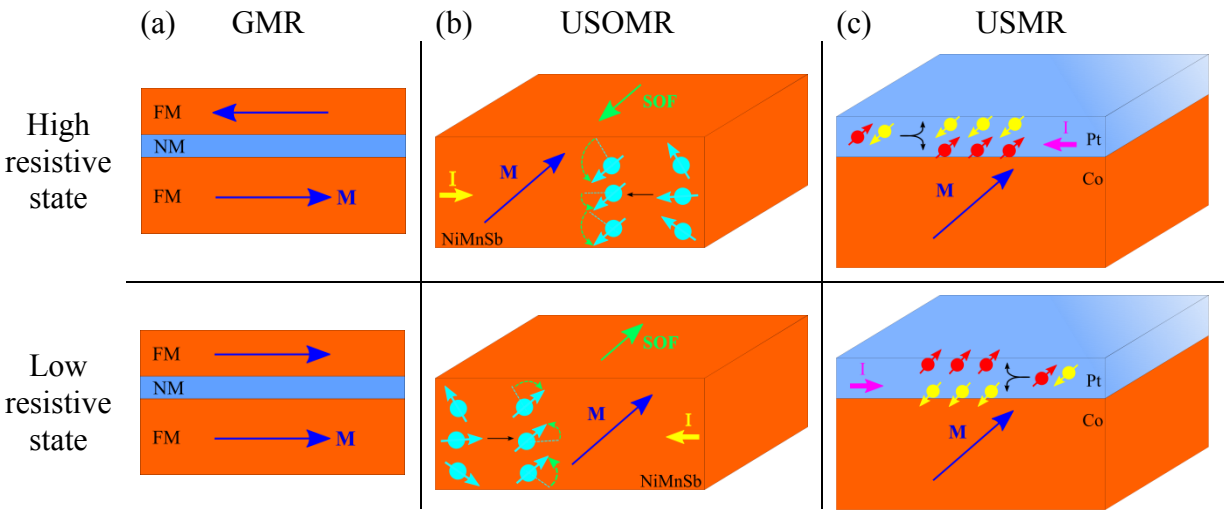


**Figure 6.1** Schematic diagram of high resistive and low resistive states in the samples with (a) GMR, (b) USOMR[20] and (c) USMR.

An analogous phenomenon, called unidirectional spin Hall magnetoresistance (USMR), has been reported in Co/Pt and Co/Ta bilayer systems as shown in Figure 6.1 (c) [215]. The heavy metal (HM) layer induces a spin accumulation at the interface via the SHE, and the USMR of the bilayer is found to reach the maximum (minimum) value when the interface spin accumulation is parallel (antiparallel) to the magnetization of the Co. Differently from conventional SMR [50,52,53] discussed in Chapter 4, the USMR is a non-linear effect and its amplitude depends on current density. The USMR is sensitive to the absolute direction of the Co magnetization and changes sign when Py is replaced by a metal of opposite spin Hall angle, such as Ta. Avci et. al. further investigated this topic by comparing W, Cu and Ti on Co [216], and found that W, which has the largest spin Hall angle of 0.33, gives the largest USMR of 0.004 % for a current density $j = 10^{11}$ A/m$^2$, while the USMR is absent in the last two cases due to the small spin Hall angle of Ti and Cu. Zhang et al. built a simple theoretical model for the USMR [217], where the nonlinear transport behaviour comes from the spin-dependent electron mobility in the ferromagnetic layer and the spin accumulation in ferromagnetic layer near the interface induced by the spin Hall effect (SHE) in the HM. This also explains the absence of the USMR in YIG/Pt system [216], since no charge current flows

[20] The electrons drawn here are only the small amount that are affected by the SOF. Most of the electrons (not drawn here) still have the magnetic momentum in parallel with the magnetization.

in the ferromagnetic insulator. Recently, the USMR has also been reported in a ferromagnet-(Ga,Mn)As/paramagnet-(Ga,Mn)As bilayer system [218], showing a much larger value (0.2% for $j = 10^{10}$ A/m$^2$) compared with ferromagnetic/HM bilayer. This is explained by the much larger resistivity of (Ga,Mn)As compared to the HM.

Compared with the USMR and conventional GMR, the USOMR in NiMnSb requires neither the adjacent HM layer nor the sandwich structure, as the spin polarization is induced directly inside NiMnSb via the SOC. Therefore, it is of great interests for the detection of magnetization switching. This chapter is separated into two sections. The first section shows the observation of the USOMR based on the current-induced ferromagnetic resonance (CI-FMR) measurement in microwave frequency range as shown in Figure 5.4. We explain the non-resonance background signal in these 2D plots as a combination of anomalous Nernst effect (ANE) and spin rectification from the USOMR. In the second section, we discuss some future work which can be done to characterise the SOMR.

## 6.1 Probing USOMR with a microwave current

We start this section by briefly introducing the ANE. ANE is a thermomagnetic phenomenon in ferromagnetic materials, where a temperature gradient can generate an electric field perpendicular to both the temperature gradient and the magnetisation [219]:

$$\mathbf{E}_{ANE} = \beta_{ANE}\left(\mu_0 \mathbf{M} \times \Delta \mathbf{T}\right) \tag{6.1}$$

The microwave current arises the temperature of NiMnSb due to the Joule heating. Since the thermal conductivity of the air and the (In,Ga)As buffer sandwiching the NiMnSb are different, this results in a temperature gradient along the out-of-plane direction. Due to ANE, an in-plane DC voltage perpendicular to the magnetisation is generated [220,221]. Considering our setup in Figure 3.5, the longitudinal $V_{\mathrm{ANE}}$ should have a $\sin\theta$ angular dependence with respect to the bar direction, which is independent from the crystalline orientation.

Referring to the CI-FMR measurements of the rectified voltage in NiMnSb presented in the previous chapter (Figure 5.4), it can be clearly observed that the non-resonance background can be fitted by $\sin(\theta + \varphi)$, where $\theta$ is the angle of the external field with respect to the bar and $\varphi$ depends on the crystalline direction in which the bar is patterned. In Figure 6.2, we plot the angle dependence of the background signal $V_{BG}$ shown in Figure 5.4 at high magnetic field far from resonance. Clearly, $V_{BG}$ along the [-110] and the [110] can be fitted by $\sin\theta$, but with opposite sign. The angle dependence of $V_{BG}$ along the [100] and the [010] contains an additional phase shift. This excludes that the background signal is entirely attributed to the ANE [169,222] and suggests an additional crystalline component.

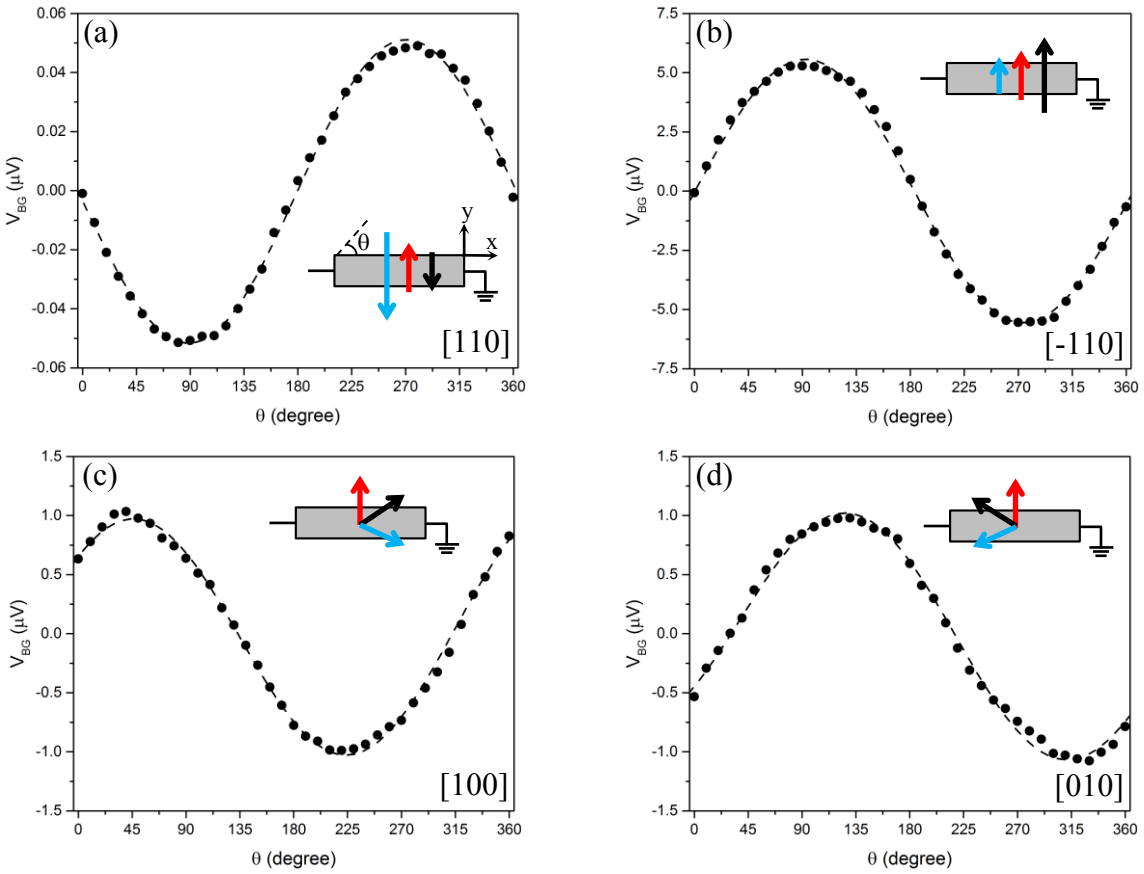


**Figure 6.2** (a) Angle dependence of non-resonance background voltage for bars along the (a) [110], (b) [-110], (c) [100] and (d) [010] direction. Insert: The grey rectangle represents an in-plane view of the sample bar. The arrows point to the maximum non-resonance voltage generated by the ANE (red), the USOMR rectification (blue) and the sum of two (black).

We try to fit our data by considering the contributions from the ANE and an additional term from the USOMR. When a current is passed the bar, the spin polarization of carriers gains a non-equilibrium component, whose direction only depends on the crystalline direction of the bar. Similar to conventional GMR, this additional spin polarization misaligned with the magnetization of the ferromagnet yields an extra term in the resistivity, which depends on the relative orientation between $\mathbf{h}_{SO}$ and the magnetization **M**.

We phenomenologically write the resistance of the NiMnSb bar as $R = R_0 - R_{AMR}\cos(2\theta) - \Delta R_{USOMR}\cos(\theta - \theta_{SO})$, where $R_0$ is a constant representing the average resistance of the bar; $R_{AMR}$ is the conventional AMR coefficient, while $\Delta R_{USOMR}$ is the current-induced change in resistance due to the USOMR; $\theta$ and $\theta_{SO}$ refer to the angle of **M** and $\mathbf{h}_{SO}$ with respect to the bar direction. The sample resistance has its minimal value when **M** // $\mathbf{h}_{SO}$, and comes to the maximum when **M** // $-\mathbf{h}_{SO}$. The amplitude $\Delta R_{USOMR}$ depends on the amount of non-equilibrium spins induced by the current flow in the FM and is linearly proportional to the current density ($\Delta R_{USOMR} \propto J_c$). As in our experiment, when a microwave current $I_c = I_0\cos(\omega t)$ flows into the bar, the sample resistance starts to oscillate at the frequency: $R = R_0 - \Delta R_{USOMR}\cos(\omega t)\cos(\theta - \theta_{SO})$. The product of this oscillating term with the oscillating current leads to a rectified component of the longitudinal voltage:

$$V = -\frac{1}{2} I_0 \Delta R_{USOMR} \cos\left(\theta - \theta_{SO}\right) \tag{6.2}$$

We carried out a power dependence of $V_{BG}$, and an example result measured for a bar along [100] is shown in Figure 6.3, while the bars in the other directions show similar results. The angle dependence of $V_{BG}$ in Figure 6.3 (a) is fitted with a sinusoidal function $A_{BG}\sin(\theta + \varphi)$. The amplitude of $V_{BG}$ is plotted in Figure 6.3 (b). The amplitude of $V_{BG}$ is linear in the microwave power, while the phase shift is independent on power. This result is expected because both the ANE and the USOMR contributions are proportional to $I_c^2$.

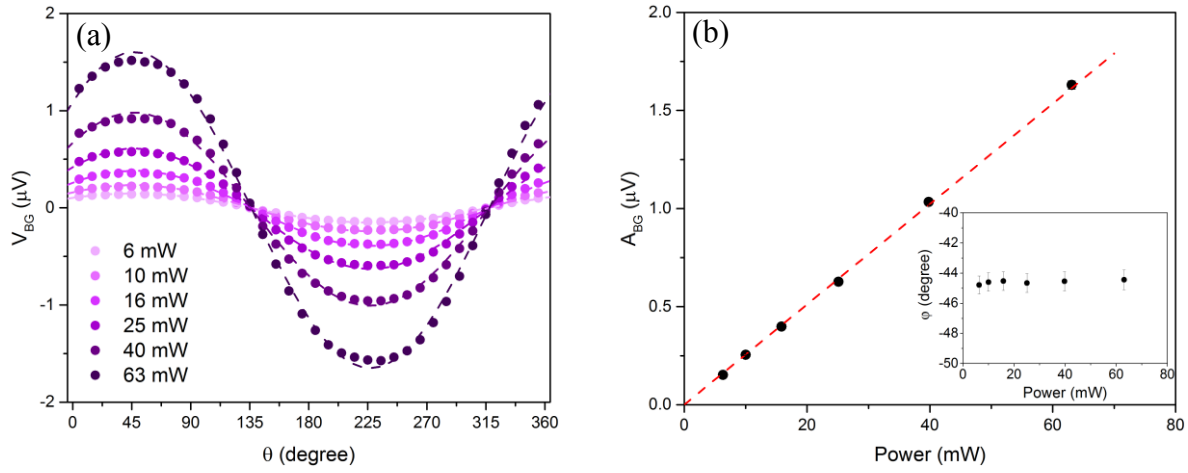


**Figure 6.3** (a) Angle dependence of the non-resonance background voltage in [100] direction at 13 GHz, with the input microwave power varying from 6.3 to 63.0 mW, fitted with a sinusoidal function (dashed line). (b) Amplitude of $V_{BG}$ showing a linear dependence with microwave power. The insert shows that the phase shift is independent on power.

In the inset of Figure 6.2, we show the unidirectional contribution to $V_{DC}$ induced by the USOMR (blue arrow), pointing in the opposite direction of $\mathbf{h}_{SO}$ (see Figure 5.8 for a complete map of $\mathbf{h}_{SO}$). The head of the arrow points in the direction where $V_{DC}$ is expected to be at its maximum for each bar direction. The ANE contribution is represented by a red arrow. The ANE induced by an out-of-plane temperature gradient. The black arrow is the sum of the two contributions respectively. The length of the arrows represents the estimated relative amplitude of each contribution. We find a good agreement between the direction of the black arrow and the angle dependence of $V_{BG}$ in each bar.

In the bars [100] and [010], the USOMR and the ANE contributions are misaligned and we are able to estimate each contribution from $\varphi$. Referring to Figure 6.2 (c) and (d), the x-component (i.e. along the bar) of the non-resonance DC voltage vector (black arrow) can be attributed to the USOMR rectification alone, while the y-component perpendicular to the bar is a combination of the contributions from the ANE and the USOMR. The direction of the total non-resonance voltage (black arrow) can be determined by fitting Figure 6.2. From Eq. (6.2), we also know that the USOMR contribution is aligned with $\mathbf{h}_{SO}$ (where $\cos(\theta - \theta_{SO}) =$

±1). The direction of $\mathbf{h}_{SO}$ is determined for the same bar and in the same set of measurements by analysing the rectified voltage at resonance as discussed in Chapter 5. This allows us to extrapolate the independent contributions for the ANE and the USOMR. Together with the linear dependence of non-resonance voltage on $J_c^2$, we extract $V_{USOMR}$ = 3.8 ± 0.3 μV and $V_{ANE}$ = 5.2 ± 0.4 μV for the bar along [100], and $V_{USOMR}$ = 2.5 ± 0.2 μV and $V_{ANE}$ = 4.4 ± 0.4 μV for the bar along [010], at a current density of $J_c = 10^{11}$ A/m$^2$. Since the vertical temperature gradient $\Delta T \propto J^2 R$, where $R$ is the bar resistance (see Table 5.1), we define a new coefficient as $S_{ANE} = V_{ANE}/R$ = 49 ± 1 and 45 ± 1 nV/Ω for the [100] and the [010] directions respectively. The values of $S_{ANE}$ varies within 10% for these two bars and it is reasonable to take $S_{ANE}$ = 47 ± 3 nV/Ω for the other two directions as well, since the ANE contribution is independent on the crystalline directions. This allows us to estimate the contributions from the SOMR for the other two directions: $V_{USOMR}$ = 12.3 ± 0.6 μV and $V_{ANE}$ = 4.9 ± 0.5 μV for the bar along [-110], and $V_{USOMR}$ = 7.6 ± 0.6 μV and $V_{ANE}$ = 4.6 ± 0.5 μV for the bar along [110], normalized to $J_c = 10^{11}$ A/m$^2$. Then, we can calculate the USOMR coefficient, defined as $\Delta R_{USOMR}/R$, at $J_c = 10^{11}$ A/m$^2$ using Eq. (6.2). The results are 11.5 ± 0.9, 17.3 ± 0.8, 5.3 ± 0.4 and 3.8 ± 0.3 in units of $10^{-6}$ for the bars along [110], [-110], [100] and [010] respectively. We find that the USOMR coefficients along the [110] and [-110] directions are respectively more than two times and three times stronger than the ones along [100] and [010]. A theoretical model that takes into account the detailed band structure and density of state for minority and majority carriers would be necessary to clarify this further.

The USOMR was not detected when carrying out current-induced ferromagnetic resonance (CI-FMR) measurement of (Ga,Mn)As [11]. The reason can be attributed to its large resistivity, which is ten times larger than that of NiMnSb. This makes ANE contribution dominant over the USOMR contribution in the non-resonance background signal.

## 6.2 Discussion and future steps

Given the in-plane geometry only, it is difficult to get a full interpretation of USOMR. However, its behaviour can be understood qualitatively by using the sophisticated two-current model, similar to GMR. We consider two separate channels for the electrons with majority and minority spins (i.e. spin ↑ and spin ↓) respectively (Figure 6.4). We use capital **S** to represent the equilibrium spin of the electrons (along **M**) and the small **s** to represent the non-equilibrium spin due to the SOC, which is linear in current density $J$. When SOF and **M** are in parallel, the amount of non-equilibrium spin in parallel (antiparallel) with M increases (decreases), and this is equivalent to decrease (increase) the resistance of majority (minority) channel, as shown in Figure 6.4 (a). The situation is the opposite when SOF and **M** are in antiparallel (Figure 6.4 (b)). Therefore, the overall effect of SOF can be modelled as an additional term $\pm r_{s\downarrow}$ (proportional to $J$) to both channel, but with opposite signs. This results in a lower (higher) overall resistive state for SOF and **M** in parallel (antiparallel). The amplitude of $r_s$ is function of current-induced spin polarization **s**($J$), which in turn is related to SOF by $\mathbf{h}_{SO} = J_{ex}\mathbf{s}(J)$, where $J_{ex}$ is s-d exchange constant. Therefore, for further analysis, it is necessary to know the value of $J_{ex}$, which, however, has not yet been determined for NiMnSb to our best knowledge.

There are several steps that we can do to further confirm USOMR and investigate its behaviour in detail. The first one is to measure it by a Hall bar structure. By probing the angle

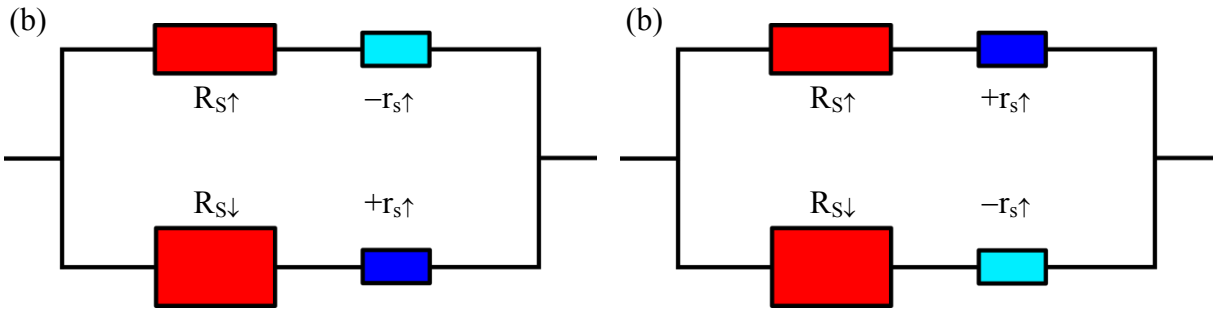


**Figure 6.4** Two-current model of USOMR when the magnetization and the SOF are in (a) parallel (lower resistance) and (b) antiparallel (higher resistance).

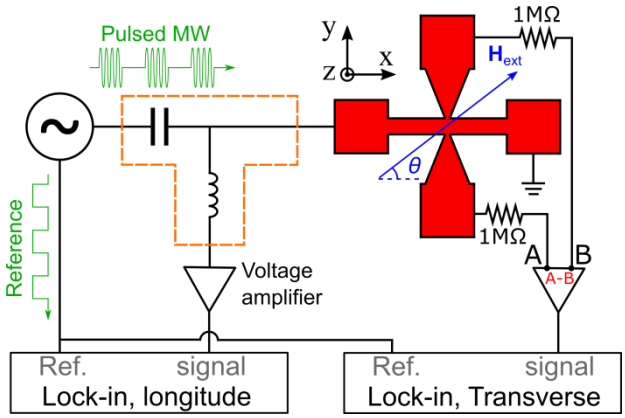


**Figure 6.5** Schematic diagram for the measurement of the USOMR using a Hall bar. We add two 1MΩ resistors to cut off the possible leakage of the longitudinal charge current to the transverse contacts.

dependence of both the longitudinal and transverse voltage when the microwave current is applied, we should be able to separate ANE and USOMR contributions experimentally. Unlike the longitudinal voltage, which is a sum of ANE and USOMR rectification, only the ANE can contribute to the transverse voltage. Hence, the transverse voltage is expected to have an angle dependence of $\sin\theta$ without any phase offset for all crystalline orientations. Therefore, the non-resonance voltage of thermal origin can be easily estimated, which helps us to determine the longitudinal voltage from USOMR rectification more precisely.

Secondly, since the USOMR is a non-resonance effect, we can measure it at low frequency by using the 2$^{nd}$ harmonic generation method, similar to [215]. The samples should be patterned into a Hall bar structure[21]. From a complete symmetry analysis obtained by rotating the magnetization not only in plane but also out of plane, we should be able to estimate precisely ANE and USOMR contributions.

Finally, it is valuable to carry out a temperature dependence measurement. Similar to the case of (Ga,Mn)As [211], we expect that at lower temperature, the current-induced spin-orbit

[21] Although we have patterned small amount of NiMnSb cross bars, the main purposes was to measure the AMR in NiMnSb. The cross bars were not re-usable because of the damage at pad when taking away the bonded wire, and there was no cross bars spared for the USOMR measurement in this thesis.

effective field is substantially enhanced which could make the contribution from USOMR dominate over that of ANE. Therefore, this allows us to observe the behaviour of USOMR more clearly, and understand how this effect varies with the sample temperature as well.

# Chapter 7 Conclusion

In this thesis, we have experimentally studied the spin dynamics of two ferromagnetic systems with strong spin-orbit coupling, namely YIG/heavy metal (HM) bilayers and NiMnSb, at room temperature. In both systems, current-induced torques (CITs) have been probed in details using the current-induced ferromagnetic resonance (CI-FMR) technique, and the mechanisms behind are well explained.

In Chapter 4, we explored the CITs in ferromagnetic insulator/HM bilayers by measuring a series of YIG samples with different thickness, capped by Pt or Ta with the spin Hall angles opposite to each other. The CITs contains three contributions, including the Oersted field, the field-like and the antidamping-like spin-transfer torques (STT), while the analysis is further complicated by the presence of spin pumping which contributes to signals of the same symmetry as those generated by the spin rectification signals. However, by carrying a thickness dependence study, we have unambiguously concluded that the Oersted field dominated over the STT in our YIG/HM bilayer systems in driving FMR.

In Chapter 5, we studied the CITs in an on-stoichiometric NiMnSb thin film with zinc-blende crystalline structure. Both field-like and antidamping-like CITs with comparable amplitudes are observed. For each of them, the CIT consists of a term of Dresselhaus symmetry and a relatively smaller term of Rashba symmetry. By comparing with the previous work on an off-stoichiometric NiMnSb thin film [15], not only the CITs, but also the anisotropic magnetoresistance and magnetic anisotropy change considerably. This provides a way to control the characteristics and the CITs in NiMnSb for different applications simply by varying the sample stoichiometry.

In Chapter 6, we reported the observation of the unidirectional spin-orbit magnetoresistance (USOMR) in NiMnSb at room temperature. Unlike the anisotropic

magnetoresistance, the USOMR scales linearly with the current, and it is unidirectional, i.e. it changes when reversing the sign of the magnetization. This provides an effective approach to detect magnetization switching in bulk NiMnSb, similar to the giant magnetoresistance. Together with the CITs explored in Chapter 5, this give us a chance to build a complete data reading and writing system in bulk NiMnSb operating at room temperature based on the spin-orbit coupling, with enormous potential for developing new spintronic devices for sensing and memory applications.

# References


[1] M. N. Baibich, J. M. Broto, A. Fert, F. N. Van Dau, F. Petroff, P. Etienne, G. Creuzet, A. Friederich, and J. Chazelas, Phys. Rev. Lett. **61**, 2472 (1988).

[2] G. Binasch, P. Grünberg, F. Saurenbach, and W. Zinn, Phys. Rev. B **39**, 4828 (1989).

[3] J. C. Slonczewski, J. Magn. Magn. Mater. **159**, L1 (1996).

[4] L. Berger, Phys. Rev. B **54**, 9353 (1996).

[5] M. Tsoi, A. Jansen, J. Bass, W.-C. Chiang, M. Seck, V. Tsoi, and P. Wyder, Phys. Rev. Lett. **80**, 4281 (1998).

[6] I. M. Miron, K. Garello, G. Gaudin, P.-J. Zermatten, M. V Costache, S. Auffret, S. Bandiera, B. Rodmacq, A. Schuhl, and P. Gambardella, Nature **476**, 189 (2011).

[7] I. M. Miron, T. Moore, H. Szambolics, L. D. Buda-Prejbeanu, S. Auffret, B. Rodmacq, S. Pizzini, J. Vogel, M. Bonfim, A. Schuhl, and G. Gaudin, Nat. Mater. **10**, 419 (2011).

[8] G. Yu, P. Upadhyaya, Y. Fan, J. G. Alzate, W. Jiang, K. L. Wong, S. Takei, S. A. Bender, L.-T. Chang, Y. Jiang, M. Lang, J. Tang, Y. Wang, Y. Tserkovnyak, P. K. Amiri, and K. L. Wang, Nat. Nanotechnol. **9**, 548 (2014).

[9] C. K. Safeer, E. Jué, A. Lopez, L. Buda-Prejbeanu, S. Auffret, S. Pizzini, O. Boulle, I. M. Miron, and G. Gaudin, Nat. Nanotechnol. **11**, 143 (2015).

[10] A. H. MacDonald, P. Schiffer, and N. Samarth, Nat. Mater. **4**, 195 (2005).

[11] D. Fang, H. Kurebayashi, J. Wunderlich, K. Výborný, L. P. Zârbo, R. P. Campion, A.

Casiraghi, B. L. Gallagher, T. Jungwirth, and A. J. Ferguson, Nat. Nanotechnol. **6**, 413 (2011).

[12] H. Kurebayashi, J. Sinova, D. Fang, A. C. Irvine, T. D. Skinner, J. Wunderlich, V. Novák, R. P. Campion, B. L. Gallagher, E. K. Vehstedt, L. P. Zârbo, K. Výborný, A. J. Ferguson, and T. Jungwirth, Nat. Nanotechnol. **9**, 211 (2014).

[13] M. Endo, F. Matsukura, and H. Ohno, Appl. Phys. Lett. **97**, 222501 (2010).

[14] A. Chernyshov, M. Overby, X. Liu, J. K. Furdyna, Y. Lyanda-Geller, and L. P. Rokhinson, Nat. Phys. **5**, 10 (2008).

[15] C. Ciccarelli, L. Anderson, V. Tshitoyan, A. J. Ferguson, F. Gerhard, C. Gould, L. W. Molenkamp, J. Gayles, J. Železný, L. Šmejkal, Z. Yuan, J. Sinova, F. Freimuth, and T. Jungwirth, Nat. Phys. **12**, 855 (2016).

[16] C. Kittel, *Introduction to Solid State Physics*, 7th ed. (John Wiley & Sons, New York, 1996).

[17] S. Blundell, *Magnetism in Condensed Matter*, 1st ed. (Oxford University Press, New York, 2001).

[18] R. Skomski, *Simple Models of Magnetism* (Oxford University Press, Oxford, 2010).

[19] P. Bruno, J. Phys. F Met. Phys. **18**, 1291 (1988).

[20] E. Hall, Am. J. Math. **2**, 287 (1879).

[21] J. Sinova, S. O. Valenzuela, J. Wunderlich, C. H. Back, and T. Jungwirth, Rev. Mod. Phys. **87**, 1213 (2015).

[22] U. Mizutani, *Introduction to the Electron Theory of Metals* (Cambridge University Press, 2001).

[23] L. Jogschies, D. Klaas, R. Kruppe, J. Rittinger, P. Taptimthong, A. Wienecke, L. Rissing, and M. C. Wurz, Sensors **15**, 28665 (2015).

[24] T. Jungwirth, J. Wunderlich, V. Novak, K. Olejnik, B. L. Gallagher, R. P. Campion, K.

W. Edmonds, A. W. Rushforth, A. J. Ferguson, and P. Nemec, Rev. Mod. Phys. **86**, 855 (2014).

[25] E. De Ranieri, A. W. Rushforth, K. Výborný, U. Rana, E. Ahmad, R. P. Campion, C. T. Foxon, B. L. Gallagher, A. C. Irvine, J. Wunderlich, and T. Jungwirth, New J. Phys. **10**, 65003 (2008).

[26] A. W. Rushforth, K. Výborný, C. S. King, K. W. Edmonds, R. P. Campion, C. T. Foxon, J. Wunderlich, A. C. Irvine, P. Vašek, V. Novák, K. Olejník, J. Sinova, T. Jungwirth, and B. L. Gallagher, Phys. Rev. Lett. **99**, 147207 (2007).

[27] N. F. Mott, Proc. R. Soc. London A Math. Phys. Eng. Sci. **156**, (1936).

[28] H. Jiao and G. E. W. Bauer, Phys. Rev. Lett. **110**, 217602 (2013).

[29] Z. Tang, Y. Kitamura, E. Shikoh, Y. Ando, T. Shinjo, and M. Shiraishi, Appl. Phys. Express **6**, 83001 (2013).

[30] C. Hahn, G. de Loubens, O. Klein, M. Viret, V. V. Naletov, and J. Ben Youssef, Phys. Rev. B **87**, 174417 (2013).

[31] K. Ando and E. Saitoh, Nat. Commun. **3**, 629 (2012).

[32] H. Tetlow and M. Gradhand, Phys. Rev. B **87**, 75206 (2013).

[33] Y. K. Kato, R. C. Myers, A. C. Gossard, and D. D. Awschalom, Science (80-. ). **306**, 1910 (2004).

[34] T. Jungwirth, J. Wunderlich, and K. Olejník, Nat. Mater. **11**, 382 (2012).

[35] S. Zhang, Phys. Rev. Lett. **85**, 393 (2000).

[36] K. Ando, S. Takahashi, J. Ieda, Y. Kajiwara, H. Nakayama, T. Yoshino, K. Harii, Y. Fujikawa, M. Matsuo, S. Maekawa, and E. Saitoh, J. Appl. Phys. **109**, 103913 (2011).

[37] J.-C. Rojas-Sánchez, N. Reyren, P. Laczkowski, W. Savero, J.-P. Attané, C. Deranlot, M. Jamet, J.-M. George, L. Vila, and H. Jaffrès, Phys. Rev. Lett. **112**, 106602 (2014).

[38] B. F. Miao, S. Y. Huang, D. Qu, and C. L. Chien, Phys. Rev. Lett. **111**, 66602 (2013).

[39] S. M. N. N. S.-C. Zhang, Science (80-. ). **31**, 1348 (2003).

[40] J. Sinova, D. Culcer, Q. Niu, N. Sinitsyn, T. Jungwirth, and A. MacDonald, Phys. Rev. Lett. **92**, 126603 (2004).

[41] J. Smit, Physica **24**, 39 (1958).

[42] L. Berger, Phys. Rev. B **2**, 4559 (1970).

[43] T. Kimura, Y. Otani, T. Sato, S. Takahashi, and S. Maekawa, Phys. Rev. Lett. **98**, 156601 (2007).

[44] O. Mosendz, J. E. Pearson, F. Y. Fradin, G. E. W. Bauer, S. D. Bader, and A. Hoffmann, Phys. Rev. Lett. **104**, 46601 (2010).

[45] H. L. Wang, C. H. Du, Y. Pu, R. Adur, P. C. Hammel, and F. Y. Yang, Phys. Rev. Lett. **112**, 197201 (2014).

[46] C. Du, H. Wang, P. C. Hammel, and F. Yang, J. Appl. Phys. **117**, 172603 (2015).

[47] L. Liu, T. Moriyama, D. C. Ralph, and R. A. Buhrman, Phys. Rev. Lett. **106**, 36601 (2011).

[48] L. Liu, C.-F. Pai, Y. Li, H. W. Tseng, D. C. Ralph, and R. A. Buhrman, Science **336**, 555 (2012).

[49] S. R. Marmion, M. Ali, M. McLaren, D. A. Williams, and B. J. Hickey, Phys. Rev. B **89**, 220404 (2014).

[50] M. Althammer, S. Meyer, H. Nakayama, M. Schreier, S. Altmannshofer, M. Weiler, H. Huebl, S. Geprägs, M. Opel, R. Gross, D. Meier, C. Klewe, T. Kuschel, J.-M. Schmalhorst, G. Reiss, L. Shen, A. Gupta, Y.-T. Chen, G. E. W. Bauer, E. Saitoh, and S. T. B. Goennenwein, Phys. Rev. B **87**, 224401 (2013).

[51] L. Liu, R. A. Buhrman, and D. C. Ralph, arXiv:1111.3702 (2011).

[52] H. Nakayama, M. Althammer, Y.-T. Chen, K. Uchida, Y. Kajiwara, D. Kikuchi, T. Ohtani, S. Geprägs, M. Opel, S. Takahashi, R. Gross, G. E. W. Bauer, S. T. B. Goennenwein, and E. Saitoh, Phys. Rev. Lett. **110**, 206601 (2013).

[53] N. Vlietstra, J. Shan, V. Castel, B. J. van Wees, and J. Ben Youssef, Phys. Rev. B **87**, 184421 (2013).

[54] N. Vlietstra, J. Shan, B. J. van Wees, M. Isasa, F. Casanova, and J. Ben Youssef, Phys. Rev. B **90**, 174436 (2014).

[55] M. Isasa, S. Velez, E. Sagasta, A. Bedoya-Pinto, N. Dix, F. Sanchez, L. E. Hueso, J. Fontcuberta, and F. Casanova, Phys. Rev. Appl. **6**, 34007 (2016).

[56] and Y. Z. W. Z. Ding, B. L. Chen, J. H. Liang, J. Zhu, J. X. Li, Phys. Rev. B **90**, 134424 (2014).

[57] M. Isasa, A. Bedoya-Pinto, S. Vélez, F. Golmar, F. Sánchez, L. E. Hueso, J. Fontcuberta, and F. Casanova, Appl. Phys. Lett. **105**, 142402 (2014).

[58] S. Cho, S. C. Baek, K.-D. Lee, Y. Jo, and B.-G. Park, Sci. Rep. **5**, 14668 (2015).

[59] C. He, A. Navabi, Q. Shao, G. Yu, D. Wu, W. Zhu, C. Zheng, X. Li, Q. L. He, S. A. Razavi, K. L. Wong, Z. Zhang, P. K. Amiri, and K. L. Wang, Appl. Phys. Lett. **109**, 202404 (2016).

[60] J. Kim, P. Sheng, S. Takahashi, S. Mitani, and M. Hayashi, Phys. Rev. Lett. **116**, 97201 (2016).

[61] X. Huang, Z. Dai, L. Huang, G. Lu, M. Liu, H. Piao, D.-H. Kim, S.-C. Yu, and L. Pan, J. Phys. Condens. Matter **28**, 476006 (2016).

[62] Y.-T. Chen, S. Takahashi, H. Nakayama, M. Althammer, S. Goennenwein, E. Saitoh, and G. Bauer, Phys. Rev. B **87**, 144411 (2013).

[63] L. Landau and E. Lifshitz, Phys. Zeitsch. Der Sow. **169**, 14 (1935).

[64] T. L. Gilbert, Phys. Rev. **100**, 1243 (1955).

[65] D. Ralph and M. Stiles, J. Magn. Magn. Mater. **320**, 1190 (2008).

[66] C. Bilzer, T. Devolder, P. Crozat, C. Chappert, S. Cardoso, and P. P. Freitas, J. Appl. Phys. **101**, 74505 (2007).

[67] I. Neudecker, G. Woltersdorf, B. Heinrich, T. Okuno, G. Gubbiotti, and C. H. Back, J. Magn. Magn. Mater. **307**, 148 (2006).

[68] S. S. Kalarickal, P. Krivosik, M. Wu, C. E. Patton, M. L. Schneider, P. Kabos, T. J. Silva, and J. P. Nibarger, J. Appl. Phys. **99**, 93909 (2006).

[69] A. A. Tulapurkar, Y. Suzuki, A. Fukushima, H. Kubota, H. Maehara, K. Tsunekawa, D. D. Djayaprawira, N. Watanabe, and S. Yuasa, Nature **438**, 339 (2005).

[70] X. Liu and J. K. Furdyna, J. Phys. Condens. Matter **18**, R245 (2006).

[71] X. Liu, Y. Sasaki, and J. K. Furdyna, Phys. Rev. B **67**, 205204 (2003).

[72] C. Kittel, Phys. Rev. **73**, (1948).

[73] C. Kittel, Phys. Rev. **110**, 1295 (1958).

[74] R. White and I. Solt, Phys. Rev. **104**, 56 (1956).

[75] M. Seavey and P. Tannenwald, Phys. Rev. Lett. **1**, 168 (1958).

[76] S. Manuilov, Ferromagnetic Resonance in Films with Growth Induced Anisotropy, Royal Institute of Technology, Sweden, 2011.

[77] L. R. Walker, J. Appl. Phys. **29**, 318 (1958).

[78] R. W. Damon and J. R. Eshbach, J. Phys. Chem. Solids **19**, 308 (1961).

[79] D. D. Stancil, *Theory of Magnetostatic Waves* (Springer, New York, 1993).

[80] B. Lenk, G. Eilers, J. Hamrle, and M. Münzenberg, Phys. Rev. B **82**, 134443 (2010).

[81] D. D. Stancil and A. Prabhakar, *Spin Waves: Theory and Applications* (Springer Science & Business Media, 2009).

[82] I. S. Maksymov and M. Kostylev, Phys. E Low-Dimensional Syst. Nanostructures **69**, 253 (2015).

[83] S. O. Demokritov, B. Hillebrands, and A. N. Slavin, Phys. Rep. **348**, 441 (2001).

[84] C. Burrowes, A. P. Mihai, D. Ravelosona, J.-V. Kim, C. Chappert, L. Vila, A. Marty, Y. Samson, F. Garcia-Sanchez, L. D. Buda-Prejbeanu, I. Tudosa, E. E. Fullerton, and J.-P. Attané, Nat. Phys. **6**, 17 (2010).

[85] S. DuttaGupta, S. Fukami, C. Zhang, H. Sato, M. Yamanouchi, F. Matsukura, and H. Ohno, Nat. Phys. **12**, 333 (2015).

[86] L. Liu, O. J. Lee, T. J. Gudmundsen, D. C. Ralph, and R. A. Buhrman, Phys. Rev. Lett. **109**, 96602 (2012).

[87] Y.-W. Oh, S. Chris Baek, Y. M. Kim, H. Y. Lee, K.-D. Lee, C.-G. Yang, E.-S. Park, K.-S. Lee, K.-W. Kim, G. Go, J.-R. Jeong, B.-C. Min, H.-W. Lee, K.-J. Lee, and B.-G. Park, Nat. Nanotechnol. **11**, 878 (2016).

[88] S. Fukami, C. Zhang, S. DuttaGupta, A. Kurenkov, and H. Ohno, Nat. Mater. **15**, 535 (2016).

[89] Y. Fan, P. Upadhyaya, X. Kou, M. Lang, S. Takei, Z. Wang, J. Tang, L. He, L.-T. Chang, M. Montazeri, G. Yu, W. Jiang, T. Nie, R. N. Schwartz, Y. Tserkovnyak, and K. L. Wang, Nat. Mater. **13**, 699 (2014).

[90] I. M. Miron, G. Gaudin, S. Auffret, B. Rodmacq, A. Schuhl, S. Pizzini, J. Vogel, and P. Gambardella, Nat. Mater. **9**, 230 (2010).

[91] M. Collet, X. de Milly, O. d'Allivy Kelly, V. V Naletov, R. Bernard, P. Bortolotti, J. Ben Youssef, V. E. Demidov, S. O. Demokritov, J. L. Prieto, M. Muñoz, V. Cros, A. Anane, G. de Loubens, and O. Klein, Nat. Commun. **7**, 10377 (2016).

[92] A. Hamadeh, O. d'Allivy Kelly, C. Hahn, H. Meley, R. Bernard, A. H. Molpeceres, V. V. Naletov, M. Viret, A. Anane, V. Cros, S. O. Demokritov, J. L. Prieto, M. Muñoz, G. de Loubens, and O. Klein, Phys. Rev. Lett. **113**, 197203 (2014).

[93] T. D. Skinner, M. Wang, A. T. Hindmarch, A. W. Rushforth, A. C. Irvine, D. Heiss, H. Kurebayashi, and A. J. Ferguson, Appl. Phys. Lett. **104**, 62401 (2014).

[94] S. Zhang and Z. Li, Phys. Rev. Lett. **93**, 127204 (2004).

[95] S. Zhang, P. M. Levy, and A. Fert, Phys. Rev. Lett. **88**, 236601 (2002).

[96] Z. Li, S. Zhang, Z. Diao, Y. Ding, X. Tang, D. M. Apalkov, Z. Yang, K. Kawabata, and Y. Huai, Phys. Rev. Lett. **100**, 246602 (2008).

[97] N. Vlietstra, J. Shan, V. Castel, J. Ben Youssef, G. E. W. Bauer, and B. J. van Wees, Appl. Phys. Lett. **103**, 32401 (2013).

[98] A. Brataas, Y. Tserkovnyak, G. E. W. Bauer, and P. J. Kelly, arXiv 1 (2011).

[99] J. . Slonczewski, J. Magn. Magn. Mater. **247**, 324 (2002).

[100] V. E. Demidov, S. Urazhdin, H. Ulrichs, V. Tiberkevich, A. Slavin, D. Baither, G. Schmitz, and S. O. Demokritov, Nat. Mater. **11**, 1028 (2012).

[101] S. Langenfeld, V. Tshitoyan, Z. Fang, A. Wells, T. A. Moore, and A. J. Ferguson, Appl. Phys. Lett. **108**, 192402 (2016).

[102] K. Xia, P. J. Kelly, G. E. W. Bauer, A. Brataas, and I. Turek, Phys. Rev. B **65**, 220401 (2002).

[103] A. Brataas, Y. V. Nazarov, and G. E. W. Bauer, Eur. Phys. J. B **22**, 99 (2001).

[104] Y. Tserkovnyak, A. Brataas, and G. Bauer, Phys. Rev. Lett. **88**, 117601 (2002).

[105] Y. Tserkovnyak, A. Brataas, G. E. W. Bauer, and B. I. Halperin, Rev. Mod. Phys. **77**, 1375 (2005).

[106] M. B. Jungfleisch, A. V. Chumak, A. Kehlberger, V. Lauer, D. H. Kim, M. C. Onbasli, C. A. Ross, M. Kläui, and B. Hillebrands, Phys. Rev. B **91**, 134407 (2015).

[107] S. Mizukami, Y. Ando, and T. Miyazaki, Japanese J. Appl. Physics, Part 1 Regul. Pap. Short Notes Rev. Pap. **40**, 580 (2001).

[108] R. Urban, G. Woltersdorf, and B. Heinrich, Phys. Rev. Lett. **87**, 217204 (2001).

[109] B. Heinrich, Y. Tserkovnyak, G. Woltersdorf, A. Brataas, R. Urban, and G. E. W. Bauer, Phys. Rev. Lett. **90**, 187601 (2003).

[110] S. M. Rezende, R. L. Rodríguez-Suárez, M. M. Soares, L. H. Vilela-Leão, D. Ley Domínguez, and A. Azevedo, Appl. Phys. Lett. **102**, 12402 (2013).

[111] A. Kapelrud and A. Brataas, Phys. Rev. Lett. **111**, 97602 (2013).

[112] A. Azevedo, L. H. Vilela-Leão, R. L. Rodríguez-Suárez, A. F. Lacerda Santos, and S. M. Rezende, Phys. Rev. B **83**, 144402 (2011).

[113] Y. Tserkovnyak, A. Brataas, and G. Bauer, Phys. Rev. B **66**, 224403 (2002).

[114] H. Kubota, A. Fukushima, K. Yakushiji, T. Nagahama, S. Yuasa, K. Ando, H. Maehara, Y. Nagamine, K. Tsunekawa, D. D. Djayaprawira, N. Watanabe, and Y. Suzuki, Nat. Phys. **4**, 37 (2008).

[115] J. C. Sankey, Y.-T. Cui, J. Z. Sun, J. C. Slonczewski, R. A. Buhrman, and D. C. Ralph, Nat. Phys. **4**, 67 (2007).

[116] J. Zhu, J. A. Katine, G. E. Rowlands, Y.-J. Chen, Z. Duan, J. G. Alzate, P. Upadhyaya, J. Langer, P. K. Amiri, K. L. Wang, and I. N. Krivorotov, Phys. Rev. Lett. **108**, 197203 (2012).

[117] X. Cheng, J. A. Katine, G. E. Rowlands, and I. N. Krivorotov, Appl. Phys. Lett. **103**, 82402 (2013).

[118] S. Miwa, S. Ishibashi, H. Tomita, T. Nozaki, E. Tamura, K. Ando, N. Mizuochi, T. Saruya, H. Kubota, K. Yakushiji, T. Taniguchi, H. Imamura, A. Fukushima, S. Yuasa, and Y. Suzuki, Nat. Mater. **13**, 50 (2014).

[119] B. Fang, M. Carpentieri, X. Hao, H. Jiang, J. A. Katine, I. N. Krivorotov, B. Ocker, J. Langer, K. L. Wang, B. Zhang, B. Azzerboni, P. K. Amiri, G. Finocchio, and Z. Zeng, Nat. Commun. **7**, 27 (2014).

[120] C. Wang, Y.-T. Cui, J. Z. Sun, J. A. Katine, R. A. Buhrman, and D. C. Ralph, J. Appl. Phys. **106**, 53905 (2009).

[121] S. Ishibashi, T. Seki, T. Nozaki, H. Kubota, S. Yakata, A. Fukushima, S. Yuasa, H. Maehara, K. Tsunekawa, D. D. Djayaprawira, and Y. Suzuki, Appl. Phys. Express **3**, 73001 (2010).

[122] W. Chen, G. De Loubens, J. M. L. Beaujour, J. Z. Sun, and A. D. Kent, Appl. Phys. Lett. **95**, 172513 (2009).

[123] J. C. Sankey, P. M. Braganca, A. G. F. Garcia, I. N. Krivorotov, R. A. Buhrman, and D. C. Ralph, Phys. Rev. Lett. **96**, 227601 (2006).

[124] T. Staudacher and M. Tsoi, J. Appl. Phys. **109**, 07C912 (2011).

[125] T. Staudacher and M. Tsoi, Thin Solid Films **519**, 8260 (2011).

[126] A. M. Gonçalves, I. Barsukov, Y.-J. Chen, L. Yang, J. A. Katine, and I. N. Krivorotov, Appl. Phys. Lett. **103**, 172406 (2013).

[127] M. B. Jungfleisch, W. Zhang, J. Sklenar, W. Jiang, J. E. Pearson, J. B. Ketterson, and A. Hoffmann, Phys. Rev. B **93**, 224419 (2016).

[128] C. F. Pai, L. Liu, Y. Li, H. W. Tseng, D. C. Ralph, and R. A. Buhrman, Appl. Phys. Lett. **101**, 122404 (2012).

[129] A. Ganguly, K. Kondou, H. Sukegawa, S. Mitani, S. Kasai, Y. Niimi, Y. Otani, and A. Barman, Appl. Phys. Lett. **104**, 72405 (2014).

[130] K. Kondou, H. Sukegawa, S. Mitani, K. Tsukagoshi, and S. Kasai, Appl. Phys. Express **5**, 73002 (2012).

[131] W. Zhang, W. Han, X. Jiang, S.-H. Yang, and S. S. P. Parkin, Nat. Phys. **11**, 496 (2015).

[132] C. F. Pai, Y. Ou, L. H. Vilela-Leao, D. C. Ralph, and R. A. Buhrman, Phys. Rev. B **92**, 64426 (2015).

[133] T. Nan, S. Emori, C. T. Boone, X. Wang, T. M. Oxholm, J. G. Jones, B. M. Howe, G. J. Brown, and N. X. Sun, Phys. Rev. B - Condens. Matter Mater. Phys. **91**, 214416 (2015).

[134] K. Sasage, K. Harii, K. Ando, K. Uchida, D. Kikuchi, and E. Saitoh, J. Magn. Magn. Mater. **322**, 1425 (2010).

[135] S. Kasai, K. Kondou, H. Sukegawa, S. Mitani, K. Tsukagoshi, and Y. Otani, Appl. Phys. Lett. **104**, 92408 (2014).

[136] X. Fan, W. Wang, Y. Wang, H. Zhou, J. Rao, X. Zhao, C. Gao, Y. S. Gui, C.-M. Hu, and D. Xue, Appl. Phys. Lett. **105**, 262404 (2014).

[137] A. R. Mellnik, J. S. Lee, A. Richardella, J. L. Grab, P. J. Mintun, M. H. Fischer, A. Vaezi, A. Manchon, E.-A. Kim, N. Samarth, and D. C. Ralph, Nature **511**, 449 (2014).

[138] Y. Wang, P. Deorani, K. Banerjee, N. Koirala, M. Brahlek, S. Oh, and H. Yang, Phys. Rev. Lett. **114**, 257202 (2015).

[139] T. D. Skinner, K. Olejník, L. K. Cunningham, H. Kurebayashi, R. P. Campion, B. L. Gallagher, T. Jungwirth, and A. J. Ferguson, Nat. Commun. **6**, 6730 (2015).

[140] T. Moriyama, S. Takei, M. Nagata, Y. Yoshimura, N. Matsuzaki, T. Terashima, Y. Tserkovnyak, and T. Ono, Appl. Phys. Lett. **106**, 162406 (2015).

[141] S. Langenfeld, Control of Magnetisation Dynamics in Permalloy Microstructures by Spin-Hall Effect, University of Cambridge, 2015.

[142] V. E. Demidov, S. Urazhdin, and S. O. Demokritov, Nat. Mater. **9**, 984 (2010).

[143] S. Kaka, M. R. Pufall, W. H. Rippard, T. J. Silva, S. E. Russek, and J. A. Katine, Nature **437**, 389 (2005).

[144] X. W. Yu, V. S. Pribiag, Y. Acremann, A. A. Tulapurkar, T. Tyliszczak, K. W. Chou, B. Bräuer, Z.-P. Li, O. J. Lee, P. G. Gowtham, D. C. Ralph, R. A. Buhrman, and J. Stöhr, Phys. Rev. Lett. **106**, 167202 (2011).

[145] A. A. Awad, P. Dürrenfeld, A. Houshang, M. Dvornik, E. Iacocca, R. K. Dumas, and J. Åkerman, Nat. Phys. **13**, 292 (2016).

[146] M. Schreier, T. Chiba, A. Niedermayr, J. Lotze, H. Huebl, S. Geprägs, S. Takahashi, G. E. W. Bauer, R. Gross, and S. T. B. Goennenwein, Phys. Rev. B **92**, 144411 (2015).

[147] T. Chiba, G. E. W. Bauer, and S. Takahashi, Phys. Rev. Appl. **2**, 34003 (2014).

[148] T. Chiba, M. Schreier, G. E. W. Bauer, and S. Takahashi, J. Appl. Phys. **117**, 17C715 (2015).

[149] T. Chiba, G. E. W. Bauer, and S. Takahashi, J. Magn. Magn. Mater. **400**, 163 (2016).

[150] J. Sklenar, W. Zhang, M. B. Jungfleisch, W. Jiang, H. Chang, J. E. Pearson, M. Wu, J. B. Ketterson, and A. Hoffmann, Phys. Rev. B **92**, 174406 (2015).

[151] M. B. Jungfleisch, W. Zhang, J. Sklenar, J. Ding, W. Jiang, H. Chang, F. Y. Fradin, J. E. Pearson, J. B. Ketterson, V. Novosad, M. Wu, and A. Hoffmann, Phys. Rev. Lett. **116**, 57601 (2016).

[152] P. Gambardella and I. M. Miron, Philos. Trans. R. Soc. A Math. Phys. Eng. Sci. **369**, 3175 (2011).

[153] A. Brataas and K. M. D. Hals, Nat. Nanotechnol. **9**, 86 (2014).

[154] Y. K. Kato and D. D. Awschalom, J. Phys. Soc. Japan **77**, 31006 (2008).

[155] E. I. Rashba, Sov. Phys. Solid State **2**, 1109 (1960).

[156] A. Manchon, H. C. Koo, J. Nitta, S. M. Frolov, and R. A. Duine, Nat. Mater. **14**, 871 (2015).

[157] Y. A. Bychkov and E. I. Rashba, J. Exp. Theor. Phys. Lett. Vol. 39, p.78 **39**, 78 (1984).

[158] F. T. Vas'ko and F. T., J. Exp. Theor. Phys. Lett. Vol. 30, p.541 **30**, 541 (1979).

[159] Y. Kato, R. C. Myers, A. C. Gossard, and D. D. Awschalom, Nature **427**, 50 (2004).

[160] G. C. La Rocca, N. Kim, and S. Rodriguez, Phys. Rev. B **38**, 7595 (1988).

[161] G. Dresselhaus, Phys. Rev. **100**, 580 (1955).

[162] M. I. Dyakonov and V. I. Perel, Sov. Phys. Solid State, Ussr **13**, 3023 (1972).

[163] M. Silver, W. Batty, A. Ghiti, and E. P. O'Reilly, Phys. Rev. B **46**, 6781 (1992).

[164] A. Y. Silov, P. A. Blajnov, J. H. Wolter, R. Hey, K. H. Ploog, and N. S. Averkiev, Appl. Phys. Lett. **85**, 5929 (2004).

[165] V. M. Edelstein and V. M., Solid State Commun. **73**, 233 (1990).

[166] L. Meier, G. Salis, I. Shorubalko, E. Gini, S. Schön, and K. Ensslin, Nat. Phys. **3**, 650 (2007).

[167] D. A. Pesin and A. H. MacDonald, Phys. Rev. B **86**, 14416 (2012).

[168] X. Wang and A. Manchon, Phys. Rev. Lett. **108**, 117201 (2012).

[169] L. Anderson, Room-Temperature Spin-Orbit Torques in a Ferromagnetic Crystal, University of Cambridge, 2015.

[170] A. Koveshnikov, G. Woltersdorf, J. Q. Liu, B. Kardasz, O. Mosendz, B. Heinrich, K. L. Kavanagh, P. Bach, A. S. Bader, C. Schumacher, C. Rüster, C. Gould, G. Schmidt, L. W. Molenkamp, and C. Kumpf, J. Appl. Phys. **97**, 73906 (2005).

[171] M. Ekholm, P. Larsson, B. Alling, U. Helmersson, and I. A. Abrikosov, J. Appl. Phys. **108**, 93712 (2010).

[172] F. Gerhard, C. Schumacher, C. Gould, and L. W. Molenkamp, J. Appl. Phys. **115**, 94505 (2014).

[173] T. D. Skinner, Electrical Control of Spin Dynamics in Spin-Orbit Coupled Ferromagnets, University of Cambridge, 2014.

[174] V. Castel, N. Vlietstra, B. J. van Wees, and J. Ben Youssef, Phys. Rev. B **86**, 134419 (2012).

[175] M. Haertinger, C. H. Back, J. Lotze, M. Weiler, S. Geprägs, H. Huebl, S. T. B. Goennenwein, and G. Woltersdorf, Phys. Rev. B **92**, 54437 (2015).

[176] K. Kaski, P. Kuivalainen, and T. Stubb, J. Appl. Phys. **49**, 1595 (1978).

[177] M. Weiler, J. M. Shaw, H. T. Nembach, and T. J. Silva, Phys. Rev. Lett. **113**, 157204 (2014).

[178] E. Schlömann, J. J. Green, and U. Milano, J. Appl. Phys. **31**, S386 (1960).

[179] A. A. Serga, A. V Chumak, and B. Hillebrands, J. Phys. D. Appl. Phys. **43**, 264002 (2010).

[180] Y. Kajiwara, K. Harii, S. Takahashi, J. Ohe, K. Uchida, M. Mizuguchi, H. Umezawa, H. Kawai, K. Ando, K. Takanashi, S. Maekawa, and E. Saitoh, Nature **464**, 262 (2010).

[181] T. Schneider, A. A. Serga, B. Leven, B. Hillebrands, R. L. Stamps, and M. P. Kostylev, Appl. Phys. Lett. **92**, 22505 (2008).

[182] M. P. Kostylev, A. A. Serga, T. Schneider, B. Leven, and B. Hillebrands, Appl. Phys. Lett. **87**, 153501 (2005).

[183] J. Krupka, B. Salski, P. Kopyt, and W. Gwarek, Sci. Rep. **6**, 34739 (2016).

[184] D. Zhang, W. Song, and G. Chai, J. Phys. D. Appl. Phys. **50**, 205003 (2017).

[185] V. Lauer, D. A. Bozhko, T. Brächer, P. Pirro, V. I. Vasyuchka, A. A. Serga, M. B. Jungfleisch, M. Agrawal, Y. V. Kobljanskyj, G. A. Melkov, C. Dubs, B. Hillebrands, and A. V. Chumak, Appl. Phys. Lett. **108**, 12402 (2016).

[186] M. A. Zimmler, B. Özyilmaz, W. Chen, A. D. Kent, J. Z. Sun, M. J. Rooks, and R. H. Koch, Phys. Rev. B **70**, 184438 (2004).

[187] T. Nonaka, K. Ando, T. Yoshino, and E. Saitoh, J. Phys. Conf. Ser. **266**, 12101 (2011).

[188] S. Y. Huang, X. Fan, D. Qu, Y. P. Chen, W. G. Wang, J. Wu, T. Y. Chen, J. Q. Xiao, and C. L. Chien, Phys. Rev. Lett. **109**, 107204 (2012).

[189] Y. M. Lu, J. W. Cai, S. Y. Huang, D. Qu, B. F. Miao, and C. L. Chien, Phys. Rev. B **87**, 220409 (2013).

[190] Y. Yang, B. Wu, K. Yao, S. Shannigrahi, B. Zong, and Y. Wu, J. Appl. Phys. **115**, (2014).

[191] B. F. Miao, S. Y. Huang, D. Qu, and C. L. Chien, Phys. Rev. Lett. **112**, 236601 (2014).

[192] V. L. Grigoryan, W. Guo, G. E. W. Bauer, and J. Xiao, Phys. Rev. B **90**, 161412 (2014).

[193] S. Vélez, V. N. Golovach, A. Bedoya-Pinto, M. Isasa, E. Sagasta, M. Abadia, C. Rogero, L. E. Hueso, F. S. Bergeret, and F. Casanova, Phys. Rev. Lett. **116**, 16603 (2016).

[194] M. Dyakonov, Phys. Rev. Lett. **99**, 126601 (2007).

[195] K. Meng, J. Xiao, Y. Wu, J. Miao, X. Xu, J. Zhao, and Y. Jiang, Sci. Rep. **6**, 20522 (2016).

[196] H. Nakayama, Y. Kanno, H. An, T. Tashiro, S. Haku, A. Nomura, and K. Ando, Phys. Rev. Lett. **117**, 116602 (2016).

[197] T. Kikkawa, K. Uchida, Y. Shiomi, Z. Qiu, D. Hou, D. Tian, H. Nakayama, X.-F. Jin, and E. Saitoh, Phys. Rev. Lett. **110**, 67207 (2013).

[198] D. Tian, Y. Li, D. Qu, X. Jin, and C. L. Chien, Appl. Phys. Lett. **106**, 212407 (2015).

[199] M. Isasa, E. Villamor, L. E. Hueso, M. Gradhand, and F. Casanova, Phys. Rev. B **91**, 24402 (2015).

[200] P. Wang, S. W. Jiang, Z. Z. Luan, L. F. Zhou, H. F. Ding, Y. Zhou, X. D. Tao, and D. Wu, Appl. Phys. Lett. **109**, 112406 (2016).

[201] Y. Li, Y. F. Cao, G. N. Wei, Y. Li, Y. Ji, K. Y. Wang, K. W. Edmonds, R. P. Campion, A. W. Rushforth, C. T. Foxon, and B. L. Gallagher, Appl. Phys. Lett. **103**, 22401 (2013).

[202] C. Hordequin, J. P. Nozières, and J. Pierre, J. Magn. Magn. Mat. **183**, 225 (1998).

[203] Z. Wen, T. Kubota, T. Yamamoto, and K. Takanashi, Sci. Rep. **5**, 18387 (2015).

[204] W. R. Branford, S. K. Clowes, M. H. Syed, Y. V. Bugoslavsky, S. Gardelis, J. Androulakis, J. Giapintzakis, C. E. A. Grigorescu, A. V. Berenov, S. B. Roy, and L. F. Cohen, Appl. Phys. Lett. **84**, 2358 (2004).

[205] B. Botters, F. Giesen, J. Podbielski, P. Bach, G. Schmidt, L. W. Molenkamp, and D. Grundler, Appl. Phys. Lett. **89**, 242505 (2006).

[206] P. Dürrenfeld, F. Gerhard, J. Chico, R. K. Dumas, M. Ranjbar, A. Bergman, L. Bergqvist, A. Delin, C. Gould, L. W. Molenkamp, and J. Åkerman, Phys. Rev. B **92**, 214424 (2015).

[207] P. Dürrenfeld, F. Gerhard, M. Ranjbar, C. Gould, L. W. Molenkamp, and J. Åkerman, J. Appl. Phys. **117**, 17E103 (2015).

[208] J. Wenisch, C. Gould, L. Ebel, J. Storz, K. Pappert, M. J. Schmidt, C. Kumpf, G. Schmidt, K. Brunner, and L. W. Molenkamp, Phys. Rev. Lett. **99**, 77201 (2007).

[209] S. Hümpfner, K. Pappert, J. Wenisch, K. Brunner, C. Gould, G. Schmidt, L. W. Molenkamp, M. Sawicki, and T. Dietl, Appl. Phys. Lett. **90**, 102102 (2007).

[210] J. Wunderlich, A. C. Irvine, J. Zemen, V. Holý, A. W. Rushforth, E. De Ranieri, U. Rana, K. Výborný, J. Sinova, C. T. Foxon, R. P. Campion, D. A. Williams, B. L. Gallagher, and T. Jungwirth, Phys. Rev. B **76**, 54424 (2007).

[211] B. Howells, K. W. Edmonds, R. P. Campion, and B. L. Gallagher, Appl. Phys. Lett. **105**, 12402 (2014).

[212] K. Ando, S. Takahashi, K. Harii, K. Sasage, J. Ieda, S. Maekawa, and E. Saitoh, Phys. Rev. Lett. **101**, 36601 (2008).

[213] S. Petit, C. Baraduc, C. Thirion, U. Ebels, Y. Liu, M. Li, P. Wang, and B. Dieny, Phys. Rev. Lett. **98**, 77203 (2007).

[214] A. M. Portis, Appl. Phys. Lett. **2**, 69 (1963).

[215] C. O. Avci, K. Garello, A. Ghosh, M. Gabureac, S. F. Alvarado, and P. Gambardella, Nat. Phys. **11**, 570 (2015).

[216] C. O. Avci, K. Garello, J. Mendil, A. Ghosh, N. Blasakis, M. Gabureac, M. Trassin, M. Fiebig, and P. Gambardella, Appl. Phys. Lett. **107**, 192405 (2015).

[217] S. S. L. Zhang and G. Vignale, Phys. Rev. B **94**, 140411 (2016).

[218] K. Olejnik, V. Novak, J. Wunderlich, and T. Jungwirth, Phys. Rev. B **91**, 180402 (2015).

[219] S. Onoda, N. Sugimoto, and N. Nagaosa, Phys. Rev. Lett. **97**, 126602 (2006).

[220] T. Miyasato, N. Abe, T. Fujii, A. Asamitsu, S. Onoda, Y. Onose, N. Nagaosa, and Y. Tokura, Phys. Rev. Lett. **99**, 86602 (2007).

[221] N. Nagaosa, J. Sinova, S. Onoda, A. H. MacDonald, and N. P. Ong, Rev. Mod. Phys. **82**, 1539 (2010).

[222] Vahe Tshitoyan, Antiferromagnets for Spintronics, University of Cambridge, 2016.

[223] B. Heinrich and J. F. Cochran, Adv. Phys. **42**, 523 (1993).

[224] M. Costache, High Frequency Spin Dynamics in Hybrid Metallic Devices, University of Groningen, 2007.

# Appendix A

# Angle dependence of the FMR lineshape

The angle dependence of ferromagnetic resonance (FMR) lineshape detected either by spin rectification or planar Hall effect (PHE) can be derived from Landau-Lifshitz-Gilbert (LLG) equation:

$$\frac{\partial \mathbf{M}}{\partial t} = -\mu_0 \gamma \mathbf{M} \times \left( \mathbf{H}_{tot} + \mathbf{h}_{eff} \right) + \frac{\alpha}{M_s} \mathbf{M} \times \frac{\partial \mathbf{M}}{\partial t} \tag{A-1}$$

where $\mathbf{M}$, and $\mathbf{H}_{\text{tot}}$ are the vectors representing the magnetization and total static magnetic field including both the external field and anisotropy fields; $\mathbf{h}_{\text{eff}} = (h_{\text{x}}, h_{\text{y}}, h_{\text{z}})e^{j\omega t}$ is the current-induced effective field at microwave frequency; $\gamma$, $\alpha$ and $M_{\text{s}}$ are gyromagnetic ratio, Gilbert damping coefficient and the saturation magnetization. We first define a new right-hand coordinate system (a-b-c) with respect to the $\mathbf{H}_{\text{tot}}$ as Figure A-1. With small-precession-angle approximation, we can assume that magnetization component along a-axis is $m_{\text{a}} \approx M_{\text{s}}$. we can now write:

$$\mathbf{M} = \begin{pmatrix} M_s \\ m_b e^{j\omega t} \\ m_c e^{j\omega t} \end{pmatrix}, \ \mathbf{h}_{eff} = \begin{pmatrix} h_a \\ h_b \\ h_c \end{pmatrix} = \begin{pmatrix} h_x \cos\theta + h_y \sin\theta \\ -h_x \sin\theta + h_y \cos\theta \\ h_z \end{pmatrix} e^{j\omega t} \tag{A-2}$$

Solving the LLG equation to the first order [223], we obtain:

$$\frac{i\omega}{\mu_0 \gamma} m_b + \left( i\Delta H + H_{ext} + H_1 \right) m_c = M_s h_z \tag{A-3}$$

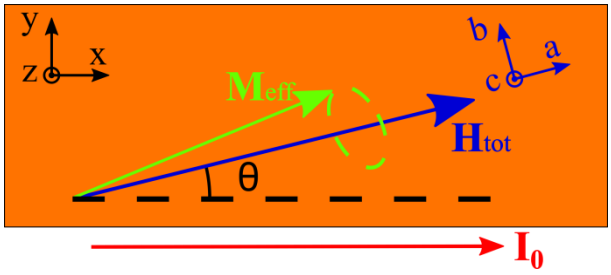


**Figure A-1** The two coordinate systems defined with respect to the charge current direction (x-y-z system) and the total static magnetic field (a-b-c system).

$$\left(i\Delta H + H_{ext} + H_2\right)m_b - \frac{i\omega}{\mu_0\gamma}m_c = M_s\left(-h_x\sin\theta + h_y\cos\theta\right) \tag{A-4}$$

where $\mu_0\Delta H = \alpha\omega/\gamma$ is the resonance linewidth; $H_1$ and $H_2$ are the terms including the anisotropy as follows [12]:

$$\begin{aligned} H_1 = M_s\left[-N_x\cos^2\left(\theta+\phi\right) - N_y\sin^2\left(\theta+\phi\right) + N_z\right] - H_{2\perp} \\ + H_{2//}\sin^2\left(\theta - \frac{\pi}{4}\right) + \frac{1}{4}H_{4//}\left(3+\cos 4\theta\right) \end{aligned} \tag{A-5}$$

$$H_2 = M_s\left(N_y - N_x\right)\cos 2\left(\theta+\phi\right) - H_{2//}\sin 2\theta + H_{4//}\cos 4\theta \tag{A-6}$$

Here, $H_{2\parallel}$ and $H_{4\parallel}$ are in-plane uniaxial and biaxial anisotropy fields respectively; $H_{2\perp}$ represents the out-of-plane anisotropy field; $\theta$ represents the angle between $\mathbf{H}_{tot}$ and the [100] crystalline direction; $N_i$ is the demagnetization factors in i-axis. We add a phase shift $\phi$ into the demagnetization term to extend our equation to the bars patterned in any crystalline directions.

From Eq. (A-3) and (A-4), we can finally obtain the expression for $m_b$ as:

$$m_b = \frac{\left[\left(H_{ext} + H_1 + i\Delta H\right)\left(-h_x\sin\theta + h_y\cos\theta\right) + \frac{i\omega}{\mu_0\gamma}h_z\right]M_s}{\left(H_{ext} + H_1 + i\Delta H\right)\left(H_{ext} + H_2 + i\Delta H\right) - \left(\frac{\omega}{\mu_0\gamma}\right)^2} \tag{A-7}$$

From section 3.3.1, we already know that the DC voltage from spin rectification can be determined as:

$$V_{SR} = -\frac{1}{2} I_0 \Delta R \theta_c \sin(2\theta) = -\frac{1}{2} I_0 \Delta R \frac{m_b}{M_s} \sin(2\theta) \tag{A-8}$$

To derive the lineshape near the resonance field $H_{res}$, we assume a small perturbation $\delta H << H_{res}$, and replace $H_{ext}$ with $H_{res} + \delta H$ in Eq. (A-7). Only keeping the real terms linear to $\delta H$ or $\Delta H$, we can get:

$$m_b = \frac{M_s}{2H_{res} + H_1 + H_2} \frac{(H_{res} + H_1)\delta H(-h_x \sin\theta + h_y \cos\theta) + \frac{\omega}{\mu_0 \gamma} \Delta H h_z}{\delta H^2 + \Delta H^2} \tag{A-9}$$

Replacing $\delta H$ with $H_{ext}$ - $H_{res}$, we finally obtain the expression for DC signal from spin rectification as:

$$V_{SR} = V_{sym-SR} \frac{\Delta H^2}{(H_{ext} - H_{res})^2 + \Delta H^2} + V_{asy-SR} \frac{(H_{ext} - H_{res})\Delta H}{(H_{ext} - H_{res})^2 + \Delta H^2} \tag{A-10}$$

where $V_{sym\text{-}SR}$ and $V_{asy\text{-}SR}$ are the Lorentzian components in symmetric and antisymmetric lineshape:

$$V_{sym-SR} = \frac{I_0 \Delta R}{2} \frac{\omega}{\mu_0 \gamma \Delta H (2H_{res} + H_1 + H_2)} h_z \sin 2\theta = \frac{I_0 \Delta R}{2} A_{sym} h_z \sin 2\theta \tag{A-11}$$

$$V_{asy-SR} = \frac{I_0 \Delta R}{2} \frac{(H_{res} + H_1)}{\Delta H (2H_{res} + H_1 + H_2)} (-h_x \sin\theta + h_y \cos\theta) \sin 2\theta = \frac{I_0 \Delta R}{2} A_{asy} (-h_x \sin\theta + h_y \cos\theta) \tag{A-12}$$

# Appendix B

# Analysis of the DC voltage in YIG/heavy metal system

The lineshape and the angle dependence has been discussed in some previous works [11,12,47,146,147], so we only focus on the dependence of each DC resonance signal on $\vartheta_{SH}$, $t_{YIG}$, and $\alpha_{eff}$ here. Following the analysis in [147], there are at least four components that contribute to the DC resonance signal, namely spin rectification and spin pumping at ferromagnetic resonance (FMR) condition driven by either spin transfer torque (STT) or Oersted field. We note these four components as $V_{ST\text{-}SR}$, $V_{ST\text{-}SP}$, $V_{Oe\text{-}SR}$ and $V_{Oe\text{-}SP}$ respectively. A simple method to analyse the dependence of each components is to separate the signal generation into FMR driving process and DC signal generation/detection process. That is, we can first analyse the mechanism by which FMR is driven and how the DC voltage is generated/detected separately, and then combine them together. The FMR driving mechanism can be described using the Landau-Lifshitz-Gilbert (LLG) equation:

$$\frac{d\mathbf{M}}{dt} = -\mu_0\gamma_{eff}\left(\mathbf{H}_{ext} + \mathbf{h}_{Oe} + \mathbf{h}_{ST}\right)\times\mathbf{M} + \frac{\alpha_{eff}}{M_s}\mathbf{M}\times\frac{d\mathbf{M}}{dt} \tag{B-1}$$

where $\mu_0$ is the vacuum permeability; $M_s$ is the saturation magnetization; $\gamma_{eff}$ and $\alpha_{eff}$ are the effective gyromagnetic ratio and the effective Gilbert damping factor respectively including the effect from spin pumping. The term $\mathbf{h}_{Oe}$ and $\mathbf{h}_{ST}$ are the effective magnetic field created by Oersted field and STT respectively, given by:

$$\mathbf{h}_{Oe} = \mathbf{y} \cdot J_c t_{NM} / 2 \tag{B-2}$$

$$\mathbf{h}_{ST} = \frac{\hbar \xi \theta_{SH} J_c}{2e\mu_0 M_s t_{YIG}} (\mathbf{M} \times \boldsymbol{\sigma}) \tag{B-3}$$

where **y** is the unit vector in y-axis, as defined in Figure 4.1 in main text; $t_{HM}$, $\vartheta_{SH}$ and $J_c$ are respectively the thickness and spin Hall angle of heavy metal (HM), and the charge current density in it; $t_{YIG}$ is the thickness of YIG; $\xi$ is the spin absorption efficiency [28]; $e$, $\mu_0$ and $\hbar$ are the constants representing elementary charge, vacuum permeability and reduced Planck constant respectively; **σ** is the unit vector of the spin polarization of the spin current created in HM via spin Hall effect. Therefore, for driving mechanisms, we know that the STT-induced effective field $\mathbf{h}_{ST}$ is proportional to $\vartheta_{SH}$ and inversely proportional to $t_{YIG}$, while the Oersted field is independent from both of them.

As for the aspect of the DC voltage-generation mechanism, the spin rectified signal is produced by the multiplication of microwave current and the dynamic change in resistance due to spin Hall magnetoresistance (SMR) effect as [12]:

$$V(t) = J_c w_{HM} t_{HM} \cos(2\pi ft) \cdot \left\{ R_0 - \Delta R \cos^2 \left[ \theta + \theta_c \cos(2\pi ft) \right] \right\} \tag{B-4}$$

where $w_{HM}$ is the width of HM layer; $R_0$ and $\Delta R$ are the bar resistance and the change in resistance due to SMR; $\theta_c$ is the magnetization precession angle; $f$ and $t$ are the microwave frequency and time. By extending the above equation using Taylor's series, we can know that the DC spin rectified voltage at resonance is [11]:

$$V_{SR} = \frac{J_c w_{HM} t_{HM} \cdot \Delta R \theta_c}{2} \sin 2\theta \tag{B-5}$$

Referring to [175], if assuming the inhomogeneous linewidth is very small, the maximum precession angle can be determined by:

$$\theta_{c-\max} = \frac{h_{eff}}{\Delta H} \approx \frac{\gamma_{eff} \mu_0 h_{eff}}{4\pi f \alpha_{eff}} \tag{B-6}$$

Here, $h_{\mathrm{eff}}$ is the effective field that drives the FMR, i.e. either STT-induced effective field or Oersted field. The effective Gilbert damping factor is calculated by introducing the additional term $\alpha_{\mathrm{SP}}$ due to the spin pumping effect:

$$\alpha_{eff}\left(t_{YIG}\right)=\alpha_0+\alpha_{SP}=\alpha_0+\frac{\gamma\hbar^2}{2e^2M_st_{YIG}}g_{eff}^{\uparrow\downarrow} \tag{B-7}$$

where $g_{\mathrm{eff}}^{\uparrow\downarrow}$ is the effective interface spin-mixing conductance.

The dependence for $\Delta R$ can be determined from the expression of SMR in [52]:

$$\Delta R\approx R_0\vartheta_{SH}^2\frac{\frac{2\lambda_{HM}^2}{\sigma_{HM}t_{HM}}g_{eff}^{\uparrow\downarrow}\tanh^2\frac{t_{HM}}{2\lambda_{HM}}}{1+\frac{2\lambda_{HM}}{\sigma_{HM}}g_{eff}^{\uparrow\downarrow}\coth\frac{t_{HM}}{\lambda_{HM}}} \tag{B-8}$$

where $\lambda_{\mathrm{SD}}$ is the spin diffusion length and conductivity of HM; Therefore, $\Delta R\propto\vartheta_{\mathrm{SH}}^2$ while it is independent from $t_{\mathrm{YIG}}$. Inputting Eq. (B-2), (B-3), (B-6), (B-7) and (B-8) into (B-5), we can qualitatively estimate the dependence of spin rectification as: $V_{\mathrm{ST\text{-}SR}}\propto\vartheta_{\mathrm{SH}}^3/(\alpha_{\mathrm{eff}}t_{\mathrm{YIG}})$ and $V_{\mathrm{Oe\text{-}SR}}\propto\vartheta_{\mathrm{SH}}^2/\alpha_{\mathrm{eff}}$.

As for spin pumping signal, the DC voltage created via ISHE is given by [106]:

$$V_{sym\text{-}SP}=R_0w_{HM}\frac{2e}{\hbar}\vartheta_{SH}\lambda_{HM}\eta\tanh\left(\frac{t_{HM}}{2\lambda_{HM}}\right)j_s^0\sin\theta \tag{B-9}$$

Here, $\eta$ is a correction factor for the ellipticity of the magnetization precession. The spin-current density $j_{\mathrm{s}}^0$ at the interface is given by [36]:

$$j_s^0=\frac{\hbar g_{eff}^{\uparrow\downarrow}\gamma^2\left(\mu_0h_{eff}\right)^2\left[\mu_0M_{eff}\gamma+\sqrt{\left(\mu_0M_{eff}\gamma\right)^2+16\left(\pi f\right)^2}\right]}{8\pi\alpha_{eff}^2\left[\left(\mu_0M_{eff}\gamma\right)^2+16\left(\pi f\right)^2\right]} \tag{B-10}$$

where $M_{\text{eff}}$ is the effective magnetization. Inputting Eq. (B-2), (B-3) and (B-10) into (B-9), it is known that $V_{\text{ST-SP}} \propto \vartheta_{\text{SH}}^3/(\alpha_{\text{eff}} t_{\text{YIG}})^2$ and $V_{\text{Oe-SP}} \propto \vartheta_{\text{SH}}/\alpha_{\text{eff}}^2$.

A summary about the deduction above can be found in Table 4.1 in the main text. It should be noted that several approximations have been made inside the analysis above, which may cause some error depending on the value of each term in reality. Therefore, it is only suitable for a simplified qualitative method which can quickly evaluate the experiment results in this paper. To analyse the results quantitatively, one is expected to input the values of each parameters and fit the results using mathematic software.

**Angle dependence of DC resonance voltage in the y-z plane**

We give a qualitatively analysis on the angle dependence of the spin rectified voltage when the external magnetic field is applied in y-z plane as defined in Figure 4.14. Compared with the in-plane case, the Eqs. (B-6) and (B-10) still hold while some modification should be made to Eq. (B-9) for out-of-plane case. From SMR measurement in Figure 4.3, the angle dependence of magnetoresistance in x-y plane and y-z plane shares the same symmetry (but opposite sign). Therefore, we should expect that:

$$V_{SR-yz} \propto \sin 2\varphi \cdot \theta_{c-\max} \propto \sin 2\varphi \cdot h_{eff} \tag{B-11}$$

For spin pumping signal, the polarization of the spin current in average is along the magnetization. Since the spin current is detected by ISHE, We need to replace the $\sin\theta$ term in Eq. (B-9) with a $\cos\varphi$ term, and the dependence of spun pumping voltage on the angle $\varphi$ becomes:

$$V_{SP-yz} \propto \cos\varphi \cdot \theta_{c-\max}^2 \propto \cos\varphi \cdot h_{eff}^2 \tag{B-12}$$

Here, the term $h_{\text{eff}}$ only includes the component in the current-induced effective field that can drive the FMR (i.e. the component perpendicular to the magnetization). Therefore, for an Oersted field in y-axis ($h_{\text{Oe-y}}$) and z-axis ($h_{\text{Oe-z}}$), the effective fields that drive FMR are $h_{\text{Oe-y}}\sin\varphi$ and $h_{\text{Oe-z}}\cos\varphi$ respectively. From Eqs. (B-11) and (B-12), the angle dependence of the DC signals in y-z plane can be qualitatively summarized as Table B-1.

**Table B-1** Angle dependence of resonance signal driven by $h_{Oe\text{-}y}$ and $h_{Oe\text{-}z}$

| **Driving field** | **Spin rectification** | **Spin pumping** |
|---|---|---|
| $h_{Oe\text{-}y}$ | $\sin 2\varphi \sin\varphi$ | $\sin 2\varphi \sin\varphi$ |
| $h_{Oe\text{-}z}$ | $\sin 2\varphi \cos\varphi$ | $\cos^3\varphi$ |